I N A U G U R A L – D I S S E R T A T I O N

zur

Erlangung der Doktorwürde

der

Naturwissenschaftlichen – Mathematischen
Gesamtfakultät

der

Ruprecht - Karls - Universität
Heidelberg

vorgelegt von

Master.-Phys. Jaena Park

aus Paju

Tag der mündlichen Prüfung: 04.11.2015

High-field Electron Spin Resonance study on Correlated Transition Metal Compounds and Metal-Organic Compounds

Gutachter: Prof. Dr. Rüdiger Klingeler
Prof. Dr. Bernd Pilawa

Kurzzusammenfassung

In der vorliegenden Arbeit werden Hochfrequenz- und X-Band-Elektronenspinresonanz-(ESR) Spektroskopie sowie Messungen der statischen Magnetisierung an korrelierten Elektronensystemen und metallorganischen Spinsystemen vorgestellt. Ergebnisse der ESR-Spektroskopie an $Na_3Ni_2SbO_6$ und $Li_3Ni_2SbO_6$ mit hexagonaler Schichtstruktur zeigen uniaxiale beziehungsweise orthorhombische antiferromagnetische Resonanzen im magnetisch geordneten Zustand, mit Spinanregungslücken von 358 GHz bzw. 200 GHz. Das zweilagige Kagomé-Gitter $Ca_{10}Cr_7O_{28}$, ein frustriertes Spinsystem, zeigt einen anisotropen g-Faktor ($g_b = 1.94$, $g_c = 2.01$) in den Hochfrequenz-ESR Daten. Die Analyse der X-band ESR Daten zeigt, dass die Temperaturabhängigkeit der Linienbreiten in den verschiedenen kristallographischen Richtungen ähnlich ist. Bei den metalloganischen Systemen wurden zwei Nickel-Dimere $[Ni_2L(dppba)]ClO_4$ und $[Ni_2L(dppba)AuPh]BPh_4$ (1) mit ähnlichen Liganden untersucht, wobei bei (1) ein zusätzliches Gold-Atom an das Phosphor-Atom eines Liganden gebunden ist. Beide Systeme zeigen eine ferromagnetische Kopplung der Ni-Ionen sowie eine uniaxiale Anisotropie von etwa -12 GHz. Der Au-Ligand bewirkt keine signifikante Änderung der magnetischen Eigenschaften. Resultate der Messungen am $[Ni(III)Ni(II)(L^{DA})](BPh_4)_2$ Komplex zeigen einen Gesamtspin von $S = 3/2$, der auf ferromagnetische Kopplung zwischen dem Ni^{2+}- ($S = 1$) und dem Low-Spin ($S = 1/2$) Ni^{3+}-Ion hinweist. Auch in diesem Fall tritt eine uniaxiale Anisotropie (-49 GHz) auf. ESR-Messungen an $(HNEt_3)_2Cu(II)[12\text{-}MC_{Cu(II)N(Shi)}\text{-}4]$ zeigen typische Pulverspektren, die sich durch einen $S = 1/2$ Spin-Hamiltonian und $g_x = 2{,}03$, $g_y = 2{,}04$ und $g_z = 2{,}23$ beschreiben lassen. $[Gd(III)_2L(OAc)_4]$ PF_6 besitzt eine magnetische Anisotropie, die auf Dipol-Wechselwirkungen der Gadolinium-Ionen zurückgeführt werden kann.

Abstract

High-frequency as well as X-band electron spin resonance (ESR) spectroscopy, and static magnetization measurements of correlated electron systems and metal-organic spins systems are presented. ESR data of the honeycomb-lattice spin systems $Na_3Ni_2SbO_6$ and $Li_3Ni_2SbO_6$ reveal uniaxial and orthorhombic antiferromagnetic resonances (AFMR), respectively, in the ordered state. In both materials, AFMR gaps of 358 GHz and 200 GHz, respectively, are found. The bilayer Kagomé lattice $Ca_{10}Cr_7O_{28}$, which is a frustrated spin system, demonstrates g anisotropy ($g_b = 1.94$, $g_c = 2.01$) depending on the crystallographic axes on high-frequency ESR data. X-band ESR data show a similar temperature dependence of the linewidths for the different axes. The two Ni dimer compounds $[Ni_2L(dppba)]ClO_4$ and $[Ni_2L(dppba)AuPh]BPh_4$ (1) have a similar ligand except an Au atom attached to the phosphorus atom of (1). In both materials, ferromagnetic coupling and uniaxial anisotropy of about -12 GHz is found. The Au ligand however does not significantly affect the magnetic properties. Results presented for the mixed valence complex $[Ni(III)Ni(II)(L^{DA})](BPh_4)_2$ demonstrate a total spin $S = 3/2$ which implies ferromagnetic coupling between the Ni^{2+} ion ($S = 1$) and the low spin Ni^{3+} ion ($S = 1/2$). Again, there is an uniaxial anisotropy which amounts to -49 GHz. ESR measurements of $(HNEt_3)_2Cu(II)[12\text{-}MC_{Cu(II)N(Shi)}\text{-}4]$ with Cu5-clusters organized in a metal-organic framework show typical powder spectra which are described by a $S = 1/2$ spin-Hamiltonian and $g_x = 2.03$, $g_y = 2.04$ and $g_z = 2.23$. $[Gd(III)_2L(OAc)_4]$ PF_6 has a magnetic anisotropy which can be ascribed to dipolar coupling between the Gd ions.

Contents

I. Introduction 1

II. Background and Experimental Setup 3

1. Theoretical Background 3

1.1. The Resonance Phenomenon . . . 3
1.1.1. Bloch Equation . . . 3
1.1.2. Magnetic Moment . . . 5
1.1.3. Selection Rule . . . 7
1.1.4. Line Position and g-factor . . . 8
1.1.5. Line Shape . . . 9
1.2. Effective Spin Hamiltonian . . . 10
1.3. Spin-Orbit Coupling and Dipolar Interaction . . . 11
1.4. Crystal Field Effect . . . 13
1.5. Exchange Interaction . . . 16
1.6. Magnetic Anisotropy . . . 17
1.7. Multiple and Giant Spin Hamiltonian . . . 20
1.8. Antiferromagnetic Resonance (AFMR) . . . 21
1.8.1. Susceptibility of a Uniaxial Antiferromagnet . . . 22
1.8.2. Uniaxial Antiferromagnetic Resonance Theory . . . 24
1.9. Simulation . . . 29

2. Experimental Technique 30

2.1. High Field - High Frequency ESR Setup . . . 30
2.2. Waveguide and Cryostat . . . 33

III. Frustrated Transition Metal Oxides 36

3. Introduction to Frustrated Spin Systems 36

4. Honeycomb-lattice Spin Systems $Na_3Ni_2SbO_6$ and $Li_3Ni_2SbO_6$ 38

4.1. Crystal Structure and Magnetic Properties . . . 39
4.2. HF-ESR: Experimental Results and Discussion . . . 40
4.3. Summary . . . 52

5. Spin-1 Kagomé Antiferromagnet $Ca_{10}Cr_7O_{28}$ 54
5.1. Kagomé Lattice 54
5.2. Crystal Structure 55
5.3. HF-ESR and X-band ESR: Experimental Results and Discussion . 55
5.4. Summary 63

IV. Metal-Organic Compounds 64

6. Introduction to Single Molecule Magnetism 64

7. Ni Dimer Complexes with Au Ligand 67
7.1. Crystal Structure 68
7.2. Magnetization and HF-ESR: Experimental Results 68
7.3. Discussion 73
7.4. Summary 75

8. Mixed Valence Dinuclear Complex Ni(II)Ni(III) 76
8.1. Crystal Structure 76
8.2. Magnetization and HF-ESR: Experimental Results 77
8.3. Discussion 82
8.4. Summary 84

9. Gd Dimer Complex 85
9.1. Crystal Structure and Magnetic Properties 85
9.2. HF-ESR: Experimental Results 86
9.3. Discussion 86
9.4. Summary 91

10. High-spin Cu_5 Complex 92
10.1. Crystal Structure and Magnetic Properties 92
10.2. HF-ESR: Experimental Results 94
10.3. Discussion 95
10.4. Summary 97

V. Summary and Outlook 98

Bibliography 101

Publication List 111

Part I.
Introduction

Magnetism has been studied since earlier than 600 b.c. The mineral magnetite, lodestone was first observed by the ancient Greeks [1]. It is called a magnet due to its ability to attract iron. Depending on the intrinsic interactions and electronic configurations, materials show different types of magnetism such as diamagnetism, ferromagnetism, and other types [2]. Accordingly, theoretical understanding of macroscopic magnetism has developed, e.g. ferromagnets have been explained by including exchange interaction and the idea of domains of macroscopic size. However, these days the scale of size of materials is becoming smaller, to nanoscale magnets, in order to, e.g. developing electronic devices using molecules. Also, nanosize magnets are a good model to study quantum phenomena [3].

From this point of view, single molecular magnets (SMMs) are an appropriate material to investigate. They possess a magnetic core surrounded by organic ligands. They are uniform in size with having an ability to approach the quantum properties in nanoscale magnets such as quantum tunneling of magnetization [4], a quantum level crossing [5], and so on [6]. Furthermore, magnetization relaxation time of SMMs is long at very low temperature because of their large spin ground state with a uniaxial anisotropy. It leads to long coherence time of SMMs which generates the chance to possibly apply them to quantum computing. Also, their molecular scale with properties of bulk materials appeals in the field of magnetic data storage [7,8]. If the range of applications is extended to molecular clusters, there are possibilities to embody in drug delivery [9] or magnetocaloric effects [10]. In order to fulfill those applications, there are still challenges, for example, increasing of the blocking temperatures of SMMs, and increasing the number of core spins or of the anisotropy [11].

While SMMs are isolated spin systems, many materials have a large number of electrons. Positions and motion of electrons are correlated by Coulomb interaction and by exchange interaction between them [12, 14]. In case of antiferromagnetically coupled systems, geometrical frustrations can be present. Due to the geometrical frustration, all the exchange interactions between spins cannot be satisfied simultaneously. This situation leads to an unclear ground state [13]. Thus, frustration may suppress long-range order and hence allows the study the effects of thermal and quantum fluctuations.

By using the electron spin resonance (ESR) technique, spin systems of SMMs and correlated materials can be studied. First ESR phenomena was observed by E. K. Zavoisky in 1945 [16]. So far, it is applied in the fields of physics, chemistry, medical, and so on [17]. ESR applied in this work uses a wide frequency range of 10 - 1000 GHz and magnetic fields up to 15 T. It is a powerful tool to study metal-organic materials with a finite number of paramagnetic core ions as well as magnetic ordering, lattice dynamics, and low energy excitation in correlated spin system [15]. In this thesis, four SMMs and three correlated materials are studied by means of ESR.

In chapter II, the theoretical background which will be used to analyze the ESR data will be described. Then, in chapter III, antiferromagnetic resonance phenomena in frustrated spin systems will be discussed, while chapter IV includes studies on metal-organic spin systems. In chapter V, the main results presented in this thesis will be summarized.

Part II.
Background and Experimental Setup

1. Theoretical Background

In this chapter, the theoretical background for ESR data analysis is discussed. The contents presented in this chapter are based on the books by S. Blundell [12], C. Kittel [18], A. Abragam and B. Bleaney [19], C. Poole [20], and G. T. Rado and H. Suhl [21].

1.1. The Resonance Phenomenon

1.1.1. Bloch Equation

Magnetization represents the macroscopic response of an ensemble of spins, which is the sum of their magnetic moments. The equation of motion of magnetization in magnetic fields can be expressed as follows,

$$\frac{d\mathbf{M}}{dt} = \gamma \mathbf{M} \times \mathbf{H}. \tag{1.1}$$

In thermal equilibrium, the components of $\mathbf{M}$ are $M_x = M_y = 0$ and $M_z = \text{const.}$ in the magnetic field $H = (0, 0, H_0)$. However, in the non-equilibrium, the state equation (Equation (1.1)) can be modified as (Bloch equation):

$$\frac{d}{dt}\vec{M} = \gamma(\vec{M} \times \vec{H}) - \frac{M_x + M_y}{T_2} + \frac{M_0 - M_z}{T_1}, \tag{1.2}$$

where T_2 and T_1 are the relaxation times. T_1 is called the longitudinal relaxation time since it changes with M_z. While T_2 is called the transverse relaxation time which is associated with the coherence of a spin state. When $M_z = M_0$, Equation (1.2) can be written as,

$$\frac{d}{dt}M_x = \gamma H_0 M_y - \frac{M_x}{T_2}, \tag{1.3}$$

$$\frac{d}{dt}M_y = -\gamma H_0 M_x - \frac{M_y}{T_2}, \tag{1.4}$$

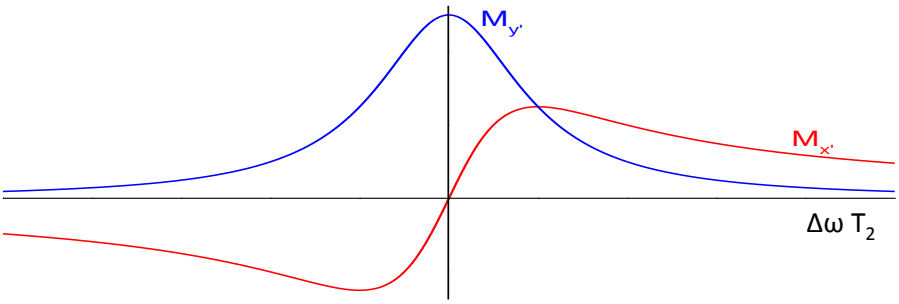

Figure 1.1: Absorption (M'_y) and dispersion (M'_x) from the Bloch equations.

$$\frac{d}{dt}M_z = 0, \tag{1.5}$$

where the solution is $M_x = A\cos\gamma H_0 t$ and $M_y = -A\sin\gamma H_0 t$ which shows a damped harmonic oscillation. In this case, transverse magnetizations precess around the z-axis with angular frequency $\omega_0 = \gamma H_0$ in the clockwise direction. ω_0 is called the Larmor frequency.

If the coordinate system (x, y, z) is the laboratory frame of reference, then the rotating frame having coordinates (x', y', z) rotates around the z-axis of the laboratory frame. The frame (x', y') rotates with ω around the z-axis. Hence, this motion leads to an effective magnetic field, $h_0 = H_0 - \omega/\gamma$. When $\omega = \gamma H_0$, the magnetization $\mathbf{M}$ is constant in the rotating frame rotating with ω by $h_0 = 0$. When an alternating magnetic field $H_1(t) = H_1\cos\omega t\hat{\mathrm{x}} + H_1\sin\omega t\hat{\mathrm{y}}$ is applied, the Bloch equation in the rotating frame can be written as

$$\frac{d}{dt}M'_x = \Delta\omega M'_y - \frac{M'_x}{T_2}, \tag{1.6}$$

$$\frac{d}{dt}M'_y = -\omega_1 M'_z - \Delta\omega M'_x - \frac{M'_y}{T_2}, \tag{1.7}$$

$$\frac{d}{dt}M'_z = \omega_1 M'_y + \frac{M_0 - M'_z}{T_1}, \tag{1.8}$$

where $\mathbf{M}'$ is the magnetization in the rotating frame, $\omega_1 = -\gamma H_1$ and $\Delta\omega = \omega_0 - \omega$. In the steady state, the Bloch equation can be solved. Resonance phenomena can be explained from solutions of Equations (1.6) and (1.7) as followings,

$$M'_x = \frac{\gamma H_1 \Delta\omega T_2^2 M_0}{1 + (\Delta\omega T_2)^2 + \gamma^2 T_1 T_2 H_1^2}, \tag{1.9}$$

$$M'_y = \frac{\gamma H_1 T_2 M_0}{1 + (\Delta\omega T_2)^2 + \gamma^2 T_1 T_2 H_1^2}, \tag{1.10}$$

where M'_x is in plane with H_1, referred to as dispersion, and M'_y is 90° out of plane with H_1, referred to as absorption, as shown in Fig. 1.1. The detected signals are proportional to the components M'_x and M'_y in continuous wave mode.

1.1.2. Magnetic Moment

The magnetic properties of paramagnetic compounds can be described based on magnetic dipole moments. These dipoles are randomly oriented in the zero magnetic field. However, in applied external magnetic fields the dipoles are preferentially oriented along the magnetic field. The dipoles possess orbital angular momentum and spin angular momentum. Their combination causes a total angular momentum. The magnetic dipole moment of an electron can be written as

$$\vec{\mu} = \gamma \hbar \vec{J}, \tag{1.11}$$

where $\vec{\mu}$ is the magnetic dipole moment, $\hbar (= h/2\pi)$ is the reduced Planck constant, $\vec{J}$ is the total angular momentum and $\gamma (= -g(e/2m_e))$ is the gyromagnetic ratio with the dimensionless quantity g.

When a free atom is in magnetic field $\vec{H}$ along the z-axis, the magnetic dipole moments are quantized with respect to the field direction. However, if only a spin angular momentum exists, its energy is given by

$$E = -\vec{\mu} \cdot \vec{H} = g\mu_B \vec{S} \cdot \vec{H} = g\mu_B m_s H_z, \tag{1.12}$$

where μ_B is the Bohr magneton, g is the g-factor, m_s is the eigenvalue of the z-component of the spin operator $\vec{S}$, and H_z is the z-component of magnetic field $\vec{H}$. Equation (1.12) shows the interaction of the magnetic dipole with an applied field H which is called the Zeeman effect. The spin states of the isotropic atoms are degenerated in the absence of an external magnetic field. The external field affects the spins differently depending on their own quantum numbers. When an atom is placed in the presence of an external field the energy levels are split according to the Zeeman effect.

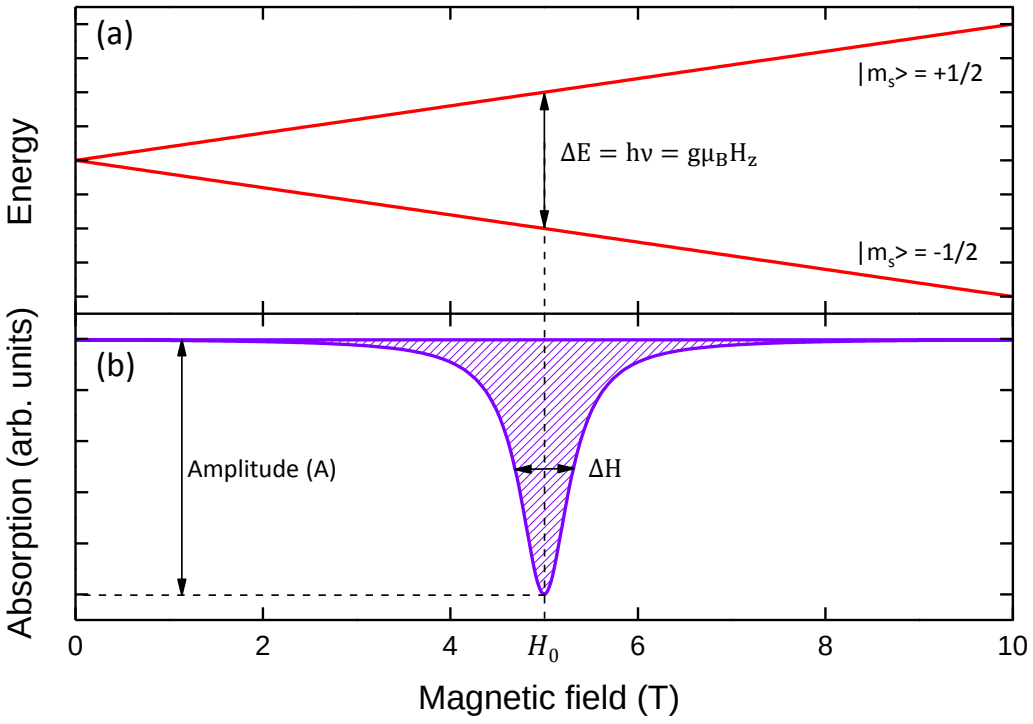

Figure 1.2: (a) Energy diagram for a spin system of $S = 1/2$. Linear Zeeman splitting depends on the external magnetic field H. Microwave radiation $h\nu$ induces a transition between the neighboring energy levels. (b) ESR absorption line with Lorentzian line shape, a linewidth parameter ΔH, and an amplitude A at the magnetic field H_0.

Depending on the total spin number S, the spin states are split into $N = 2S + 1$ states in the magnetic fields. A magnetic dipole transition between the energy levels can occur by the absorption of microwave radiation with energy $h\nu$, which is a difference between the neighboring energy levels. When an isolated free electron system of $S = 1/2$ is considered, the energy levels are split into two energy states, $|m_s\rangle = +1/2$ and $|m_s\rangle = -1/2$ in a magnetic field as shown in Fig.1.2 (a). At low temperatures the population of electrons in the lower energy state $|m_s\rangle = -1/2$ is higher than that in the higher energy state $|m_s\rangle = +1/2$, according to the Boltzmann distribution. Therefore when the system is exposed to microwave radiation with appropriate frequency, the induced excitation from the lower state to the higher state is dominant compared with induced relaxation

from the higher state to the lower state.

1.1.3. Selection Rule

When a system is in magnetic fields, transitions between the different spin states induced by an electromagnetic radiation obey the selection rule,

$$\triangle L = 0, \triangle S = 0, \triangle m_s = \pm 1. \tag{1.13}$$

In this chapter, the selection rules are discussed. Let's assume that there is an isolated spin in magnetic field $\vec{H}$ which is applied along the z-axis. If an alternating magnetic field is applied perpendicular to a strong external magnetic field $\vec{H}$ along the z-axis, there will be an additional perturbation.

$$H^{'} = H_x \mu_x + H_y \mu_y, \tag{1.14}$$

where $\mu_x = g\mu_B S_x$ and $\mu_y = g\mu_B S_y$. Equation (1.14) can be rewritten with the components of oscillatory fields $H_x = H_1 \cos \omega t$ and $H_y = H_1 \sin \omega t$ as follows,

$$H^{'} = g\mu_B H_1 \{\cos wt S_x + \sin wt S_y\}. \tag{1.15}$$

It can be calculated as follows,

$$H^{'} = \frac{1}{2} g\mu_B H_1 \{S_+ e^{-i\omega t} + S_- e^{i\omega t}\}, \tag{1.16}$$

where $S_+ = S_x + iS_y$ and $S_- = S_x - iS_y$ are ladder operators and ω is the angular frequency of the microwave radiation. The sum of all states $\mid \varphi_n >$ can be described as

$$\mid \psi(t) >= \sum_n a_n(t) e^{-\frac{iE_n t}{\hbar}} \mid \varphi_n >, \tag{1.17}$$

where $a_n(t)$ is the transition amplitude and E_n is the energy of the nth state. From the Schrödinger equation the derivative of $a_n(t)$ with respect to time can be calculated as follows,

$$\sum_n a_n(t) e^{-\frac{iE_n t}{\hbar}} H'(t) \mid \varphi_n >= \sum_n i\hbar \frac{da_n(t)}{dt} e^{-\frac{iE_n t}{\hbar}} \mid \varphi_n > . \tag{1.18}$$

Applying $< \varphi_k \mid e^{\frac{iE_n t}{\hbar}}$ on both sides,

$$i\hbar\frac{da_k(t)}{dt} = \sum_n a_n(t)e^{\frac{i}{\hbar}t(E_k-E_n)} < \varphi_k \mid H'(t) \mid \varphi_n > . \tag{1.19}$$

Transition from an initial state $\mid \varphi_n >$ to a final state $\mid \varphi_k >$ can be known from $da_k(t)/dt$. In this case S_+ and S_- in the Hamiltonian H' increase or decrease a quantum number of an eigenstate of a system as follows [52],

$$S_\pm|s\, m_s\rangle = \hbar\sqrt{s(s+1) - m_s(m_s \pm 1)}|s\, m_s \pm 1\rangle, \tag{1.20}$$

which causes transitions $m_s \rightarrow m_s \pm 1$. Hence, the selection rules are $\Delta S = 0$ and $\Delta m_s = \pm 1$.

1.1.4. Line Position and g-factor

In an actual experiment, the magnetic field is swept while the frequency is kept constant. According to $h\nu = g\mu_B H_r$, the position of a resonance line indicates the magnetic field where the absorption in the sample takes place. From the resonance field H_r, the g-factor can be calculated as,

$$g = \frac{h}{\mu_B}\frac{\nu}{H_r} \approx \frac{1}{14}\frac{\nu}{H_r}, \tag{1.21}$$

where the frequency ν is in GHz and the resonance field H_r is in T. For example, when a microwave radiation with a frequency of 10 GHz is applied to a system of $S = 1/2$, and the resonance occurs at 0.23 T, it implies $g = 2$. However, there is not only the applied magnetic field but also a local field that is caused by an interaction between a metal ion and its surrounding ions and molecules. This local field and the external magnetic field produce total effective field B_{eff}. Therefore, the g-factor that is obtained in the experiment is also known as effective g-factor g_e. Consequently, the orbital motion of the metal ion is affected differently along the x, y, and z axes in a molecule. This results in anisotropic g-factors, which can be considered as a tensor, $\tilde{g}$. The Zeeman splitting can be written as,

$$E = \mu_B \vec{H} \cdot \tilde{g} \cdot \vec{S}. \tag{1.22}$$

Most cases can be simplified to describe the g-tensor in a principal axis system.

$$\tilde{g} = \begin{pmatrix} g_x & 0 & 0 \\ 0 & g_y & 0 \\ 0 & 0 & g_z \end{pmatrix}. \tag{1.23}$$

Matrix multiplication of Equation (1.22) with the components of $\vec{S} = (S_x, \quad S_y, \quad S_z)$ and $\vec{H} = (Hsin\theta cos\phi, \quad Hsin\theta sin\phi, \quad Hcos\phi)$ induces the effective g-factor

$$g = \sqrt{g_x^2\, sin^2\theta cos\phi^2 + g_y^2\, sin^2\theta sin^2\phi + g_z^2\, cos^2\theta}. \tag{1.24}$$

In axial symmetry, the directions of x, and y axes are equal, but the direction of the z axis may be different, which results in $g_x = g_y \neq g_z$. Equation (1.24) can be written as,

$$g = \sqrt{g_x^2\, sin^2\theta + g_z^2\, cos^2\theta}. \tag{1.25}$$

1.1.5. Line Shape

Even though a resonance occurs at an exact magnetic field, a spectrum has a finite line width, because electron spins interact not only with the external magnetic field but also their environment. Thus, information about line width and line shape can be used to study spin systems.

The exchange interaction among the spins themselves influences the line width as well. When the exchange interaction is isotropic the ESR resonance line focuses more in the center of the line [22]. It is called an exchange narrowing. It can be described by a Lorentzian line shape as shown in Fig.1.2 (b).

$$f(H) = \frac{1}{\pi}\frac{\Delta H}{(\Delta H)^2 + (H - H_0)^2}. \tag{1.26}$$

Additionally, the intensity of the line is affected by the power of the applied microwave radiation, by the temperature, and by the concentration of the ions. The absorbed power by the resonating spin system can be described as,

$$P = \frac{1}{2}\omega\chi^{"}(H - H_0)^2, \tag{1.27}$$

where $\chi^{"}$ is the imaginary part of the dynamic susceptibility and ω is the microwave frequency. ESR measurements observe only $\chi^{"}$ corresponding to the dissipated energy by absorption [23]. The absorbed power is proportional to the intensity of the ESR line corresponding to the integral of the lineshape. For the Lorentzian line shape, line area is proportional to the value of the amplitude A times the linewidth ΔH.

$$I \propto A\Delta H. \tag{1.28}$$

On the other hand, an anisotropic exchange interaction leads to an inhomogeneous line broadening. When a spin is located in a complex surrounding, all the individual spins experience different local magnetic fields. Then resonances occur at slightly different magnetic fields. A merging of all individual resonances of all different spins causes the inhomogeneous broadening. It can be described by a Gaussian line shape,

$$f(H) = \sqrt{\frac{1}{2\pi(\Delta H)^2}} \exp\left\{\frac{(H - H_0)^2}{2(\Delta H)^2}\right\}. \tag{1.29}$$

The interaction between spins with different Larmor frequencies is also one source of inhomogeneous broadening [24].

1.2. Effective Spin Hamiltonian

An atom consists a nucleus with a charge of +Ze and Z electrons with a charge of -e bound to the nucleus. The Hamiltonian of this system can be written as,

$$H = \sum\left\{-\frac{\hbar^2}{2m}\nabla_j^2 - \left(\frac{1}{4\pi\varepsilon_0}\right)\frac{Ze^2}{r_j}\right\} + \frac{1}{2}\left(\frac{1}{4\pi\varepsilon_0}\right)\sum\frac{e^2}{|r_j - r_k|}, \tag{1.30}$$

where $\hbar$ is the Planck constant, m is the mass of a particle, ε_0 is the dielectric permittivity, and r_j and r_k are the position vectors of the electrons with charge e. The first term includes the kinetic energy of the electron and its Coulomb potential of the nucleus. The second term represents the potential energy of the interactions between the spins. In a compound, atoms interact with each other, which results in crystal field effects, spin-spin interaction, quadrupole energy, and nuclear spin interaction which will be discussed in the next sections. When the compound is in magnetic fields, the Zeeman effect occurs. Note that the magnitude of the Zeeman interactions is ~ 1 cm^{-1} at the magnetic fields ~ 1 T. It is possible to analyze the ESR spectrum by an effective Hamiltonian because the ground manifold is within few cm^{-1}, considering the Zeeman effect. Hence a simple Hamiltonian considering only the effective spins in the ground state can be written as

$$H = H_{Zeeman} + H_{Exchange} + H_{Anisotropy}. \tag{1.31}$$

This simple Hamiltonian employs the concept of the effective spin $\tilde{S}$, which enables the interpretation and classification of the obtained spectrum [91]. The terms of the Hamiltonian can be modified depending on the particular investigated spin system where the energy hierarchy may be different.

1.3. Spin-Orbit Coupling and Dipolar Interaction

Spin-orbit coupling and dipolar interaction cause magnetic anisotropy. Spin-orbit coupling is a coupling between a spin angular moment of an electron and its orbital angular moment.

An electron has an orbital angular moment due to the movement around the nucleus. When the electron moves with velocity $\vec{v}$ around the nucleus, it interacts with the electromagnetic field generated by the nucleus. In the frame of the electron, the nucleus moves around the electron. Hence, the nucleus with velocity $-\vec{v}$ moves around the electron and the resulting current creates the magnetic field $\vec{B}$ at the electron site. $\vec{B}$ can be written as

$$\vec{B} = \frac{1}{c}\vec{v} \times \vec{\bigtriangledown}\Phi, \tag{1.32}$$

where Φ is the potential of the nucleus, $\vec{v}$ is the speed of the nucleus, and c is the speed of light. When the distance between the nucleus and the electron is r, Equation (1.32) can be rewritten as,

$$\vec{B} = \frac{1}{mcr}\frac{d\Phi}{dr}(m\vec{v} \times \vec{r}), \tag{1.33}$$

where m is the mass of the electron, and $m\vec{v} \times \vec{r}$ is substituted for the angular moment $\vec{l}$.

When this magnetic field interacts with the magnetic moment $\vec{\mu}_s$, the corresponding Hamiltonian equation can be written as,

$$\begin{aligned} H_{spin-orbit} &= -\vec{\mu}_s \cdot \vec{B} \\ &= \frac{1}{2m^2c^2}\left(\frac{1}{r}\frac{\partial V}{\partial r}\right)\vec{l} \cdot \vec{s} = \zeta\vec{l} \cdot \vec{s}, \end{aligned} \tag{1.34}$$

with the spin-orbit coupling parameter ζ. Here, the Thomas factor of $1/2$ is multiplied to consider the time dilation between the nucleus and the electron [25].

When the spin-orbit coupling is weak in a multiple-electron system, the individual orbital angular momenta can be added to a total orbital angular momentum L. Also, the individual spin angular momenta are combined to a total spin angular momentum S. Then the total angular momentum J is given by

$$\vec{J} = \vec{L} + \vec{S}. \tag{1.35}$$

This is called the LS-coupling or the Russell-Saunders coupling [26]. Equation (1.34) can be written as,

$$H_{LS} = \lambda \vec{L} \cdot \vec{S}, \tag{1.36}$$

where $\lambda = \pm \left(\frac{\zeta}{2S}\right)$. In the case of less than half-filled shells, λ is positive, otherwise, it is negative.

When both, orbital and spin angular momenta are present, the g-factor depends on their coupling. The appropriate g-factor is given by

$$g_L = \frac{3}{2} + \frac{L(L+1) - S(S+1)}{2J(J+1)}. \tag{1.37}$$

This value is called the Landé g-factor. In magnetic fields, a system splits into a multiplet of levels with different values of J. The magnitude of the splitting is $\sim 10^2$ cm^{-1} for $3d$ electrons in magnetic fields.

Magnetic anisotropy is also caused by dipolar interaction. This interaction is much smaller than the spin-orbit coupling. The magnitude of this interaction is less than 1 cm^{-1}. The dipolar interaction arises from the interaction between spins. One magnetic dipole creates a local magnetic field and neighboring dipoles experience it. The dipolar interaction can be written as,

$$H_{dipolar} = \frac{\mu_0}{4\pi r^3}[3(\mathbf{m}_1 \cdot \widehat{\mathbf{r}})(\mathbf{m}_2 \cdot \widehat{\mathbf{r}}) - \mathbf{m}_1 \cdot \mathbf{m}_2], \tag{1.38}$$

where $\mathbf{m}_1$ and $\mathbf{m}_2$ are magnetic moments, μ_0 is the permeability of free space, r is the distance between the two dipoles, and $\widehat{\mathbf{r}}$ is a unit vector parallel to the line from the centers of the two dipoles.

1.4. Crystal Field Effect

Not only the spin-orbit coupling and dipolar interaction but also the geometrical structure of the surrounding atoms/ions has an influence on the magnetic anisotropy. When an ion is surrounded by other ions, the degeneracy of electron orbital states can be broken, which is due to an electrostatic field produced by the surrounding ions. This is described by the crystal field theory [27].

In this chapter, d-orbitals of transition metal ions are considered. As an example, an isotropic ion such as Ni^{2+} is studied. Fig.1.3 (a) shows its electron orbital states. The Ni^{2+} ion has five d-orbitals. Originally, i.e. in the case of a free ion, they are completely degenerated.

Fig.1.3 (b) shows that the Ni^{2+} ion is located at the center of a ligand cage of octahedral symmetry. The six non-metallic ions, such as O ([He] $2s^2 2p^4$) or Cl ([Ne] $3s^2 3p^5$), occupy the vertices of the octahedron. Then the d-orbitals split into two groups. This splitting is caused by the Coulomb repulsion between the $3d$-orbitals of Ni^{2+} and the $2p$-orbitals of the oxygen ions.

The $3d$-orbitals in the e_g and t_{2g} states are shown in Fig.1.3 (b). The e_g states consist of two orbitals d_{z^2} and $d_{x^2-y^2}$. These orbitals point directly to the p-orbitals as shown in Fig. 1.4 (b). The t_{2g} state includes the three orbitals d_{xy}, d_{yz} and d_{zx}. They point between p-orbitals as shown in Fig. 1.4 (a). The orbitals of the e_g state overlap with the $2p$-orbitals more than the orbitals of the t_{2g} state. Hence, the e_g states have a higher energy than the t_{2g} states. On the other hand, when an ion is in the cage of a tetrahedral symmetry, the t_{2g} states have higher energy than the e_g states.

Now imagine a distorted octahedral symmetry with elongation along the z-axis. Then the octahedral symmetry changes to a tetragonal symmetry [28]. The resulting energy level splitting in tetragonal symmetry is shown in Fig.1.3 (c). The five d-orbitals are split into such four groups: b_{1t}, a_{1t}, b_{2t} and e_t. In this case, the d_{z^2} orbital energy is smaller than the $d_{x^2-y^2}$ orbital energy, because the distance between the d_{z^2} orbital and the p-orbitals is longer due to the elongation along the z-axis. Due to the axial distortion of the octahedral symmetry, there is an energetically favorable direction that causes an axial magnetic anisotropy. An elongation along the z axis causes an easy axis ($D < 0$). If there is a compression along the z-axis or an elongation along the x and y-axis, the d_{z^2} orbital energy state is higher than the $d_{x^2-y^2}$ orbital energy state. It generates an easy plane type ($D > 0$) magnetic anisotropy.

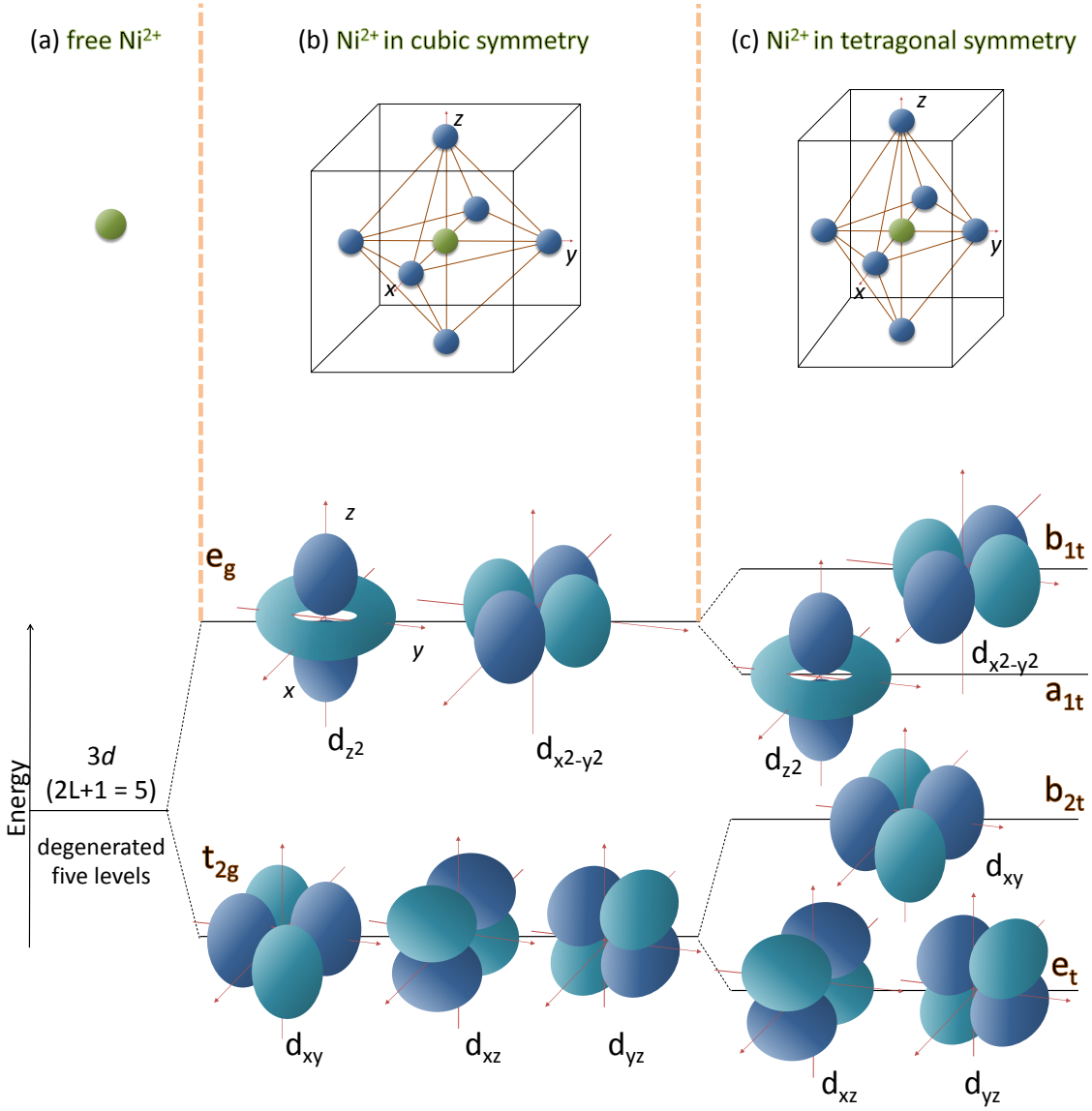

Figure 1.3: Effect of the crystal field depends on the local symmetry. (a) A free Ni^{2+} ion has a spherical symmetry. The five d-orbital ($2L + 1 = 5$) states are degenerated. (b) Ni^{2+} ion and six ligands form a cubic symmetry. There is splitting into two energy groups of energy levels. Due to a larger overlap between d-orbitals and p-orbitals of oxygen ions, the e_g states have a higher energy. The t_{2g} states are located at lower energy because of a lower overlap. (c) The Ni^{2+} ion is in the center of a distorted octahedron. The distances between the transition metal ions and the six ligands are different. Hence, the d-orbital states split into four groups as sketched.

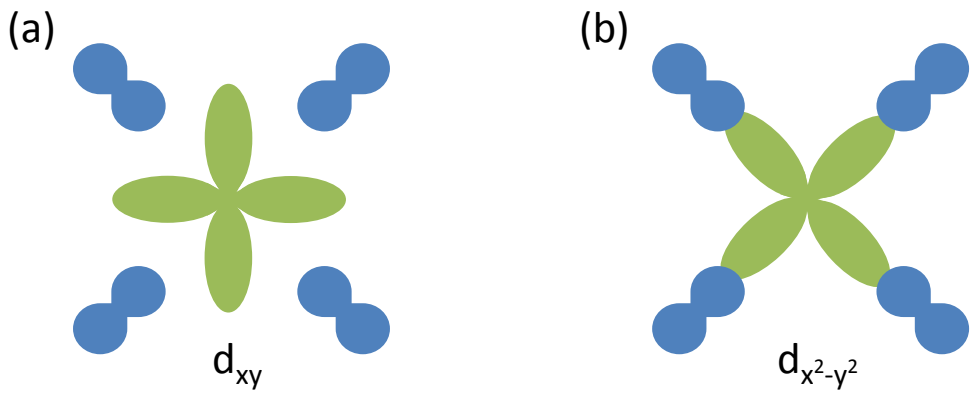

Figure 1.4: Electrostatic interaction between p- and d-orbitals in an octahedral symmetry. (a) The d_{xy} orbital overlaps less with the p-orbitals. In this case, the electrostatic energy is low. (b) The $d_{x^2-y^2}$ orbital points in the same direction as the p-orbitals, which leads to higher overlap. Hence, the electrostatic energy is high.

Quenching of the Orbital Angular Momentum The effective magneton numbers p $(= g\sqrt{J(J+1)})$ for $3d$ ions can be calculated with the values of S, L, and J using Hund's rules. However, the predicted effective magneton numbers of the transition metal ions do not agree with the value from experiments, except for $L = 0$ for $3d^5$ and $3d^{10}$. This is due to the crystal field interaction for $3d$ ions which is much stronger than the spin-orbit coupling. Hence, the third Hund's rule considering the spin-orbit coupling cannot be applied in this case. The $3d$ ions rather follow effective magneton numbers with $L = 0$. This means that the orbital angular momentum is quenched. The L_z in the spherical coordinate system can be described as $L_z = \left(\frac{\hbar}{i}\right)\left[\left(x\frac{\partial}{\partial y}\right) - \left(y\frac{\partial}{\partial x}\right)\right]$ [29]. For the ground state $\mid \psi >$, which is real, in case of completely non-degenerate levels (except for Kramers degeneracy), the expectation value of L_z is purely imaginary. Nevertheless, $< L_z >$ must be real because it is an observable quantity. Both L_z and $< L_z >$ can be imaginary and real, respectively, if $< L_z > \equiv 0$ [30].

For example, Ni^{2+} has the spin configuration $3d^8$. In an octahedral crystal field, the t_{2g} levels are fully occupied by antiparallel spin pairs. The t_{2g} orbitals do not contribute to the magnetism. However, the e_g levels are partially occupied by

unpaired single spins. The operator L_z acts on the e_g orbital state [31].

$$L_z|d_{x^2-y^2}\rangle = 2i|d_{xy}\rangle, \qquad L_z|d_{z^2}\rangle = 0. \tag{1.39}$$

Therefore, the expectation values of L_z on the e_g manifold are zero.

$$\langle d_{x^2-y^2}|L_z|d_{x^2-y^2}\rangle = 2i\langle d_{x^2-y^2}|d_{xy}\rangle = 0, \qquad \langle d_{z^2}|L_z|d_{z^2}\rangle = 0. \tag{1.40}$$

For L_y and L_x, the result will be the same.

$$\langle d_{x^2-y^2}|L_x|d_{x^2-y^2}\rangle = -i\langle d_{x^2-y^2}|d_{yz}\rangle = 0, \quad \langle d_{z^2}|L_x|d_{z^2}\rangle = -i\sqrt{3}\langle d_{z^2}|d_{yz}\rangle = 0, \tag{1.41}$$

$$\langle d_{x^2-y^2}|L_y|d_{x^2-y^2}\rangle = -i\langle d_{x^2-y^2}|d_{zx}\rangle = 0, \quad \langle d_{z^2}|L_y|d_{z^2}\rangle = i\sqrt{3}\langle d_{z^2}|d_{zx}\rangle = 0. \tag{1.42}$$

From this result, the orbital moment vanishes for the e_g orbitals. This is called orbital quenching. Accordingly, the effective magnetic moment is obtained only based on the spin contribution. Therefore the effective magneton numbers can be rewritten as,

$$p = g\sqrt{S(S+1)}. \tag{1.43}$$

Furthermore, $\vec{L}$ is also neglected to compute the Landé g-factor and the total angular momentum.

1.5. Exchange Interaction

In the following, an exchange interaction is described in terms of electrostatic interaction between particles with overlapping wave functions. In the total wave function of both particles, there are two possibilities for the spin part: one is the symmetric triplet state ψ_+ and the other is the antisymmetric singlet state ψ_-.

Let's assume that electrons 1 and 2 are in the states $\psi_a(1)$ and $\psi_b(2)$, respectively. The total wave function of these two electrons can be described by,

$$\psi_\pm(1,2) = A[\psi_a(1)\psi_b(2) \pm \psi_b(1)\psi_a(2)], \tag{1.44}$$

where a and b are the quantum states of spins and A is the spatial part wave function. When two wave functions of two electrons overlap, they have a force of repulsion. Because of the Pauli's exclusion principle, two fermions cannot

occupy the same spatial locus. Therefore, the wave function would have an antisymmetric combination of the exchange of two electrons. This will be the singlet state ($S = 0$). The other allowed state will be the symmetric triplet state ($S = 1$).

The exchange constant can be calculated from the difference between the energies $E_\pm$ of the two states $\psi_\pm$.

$$J = \frac{E_+ - E_-}{2}. \tag{1.45}$$

A negative J means that the spins are coupled antiferromagnetically. A positive J means ferromagnetically coupled spins. The spin dependent part in the effective Hamiltonian can be written as,

$$H_{Exchange} = -2J\vec{S_1} \cdot \vec{S_2}. \tag{1.46}$$

The Heisenberg exchange Hamiltonian contains the coupling between the nearest neighboring spins in a crystal. The generalization to a many-body system will be

$$H_{Exchange} = -\sum_{ij} J\vec{S_i} \cdot \vec{S_j}, \tag{1.47}$$

where i and j are spins and J_{ij} is the exchange constant between them. When the each pair of spins is summed twice, the factor 2 is eliminated.

1.6. Magnetic Anisotropy

For a system with total spin number $S \geq 1$, energy splitting can occur at zero field since spin-orbit interaction coupled the spin to the local crystalline environment. This is described by the phenomenological Hamiltonian

$$H_{Anisotropy} = \mathbf{S} \cdot \mathbf{D} \cdot \mathbf{S} = \begin{pmatrix} S_x & S_y & S_z \end{pmatrix} \begin{pmatrix} D_{xx} & D_{xy} & D_{xz} \\ D_{yx} & D_{yy} & D_{yz} \\ D_{zx} & D_{zy} & D_{zz} \end{pmatrix} \begin{pmatrix} S_x \\ S_y \\ S_z \end{pmatrix}, \tag{1.48}$$

where $\mathbf{D}$ is a traceless (the sum of the elements on the diagonal is zero) and a symmetric tensor ($D_{ij} = D_{ji}$). If D is diagonal, then Equation (1.48) can be rewritten as,

$$H_{Anisotropy} = D_{xx}S_x^2 + D_{yy}S_y^2 + D_{zz}S_z^2, \tag{1.49}$$

with the following relations for D and E

$$D = D_{zz} - (D_{xx} + D_{yy})/2, \qquad E = (D_{xx} - D_{yy})/2. \tag{1.50}$$

Considering Equation (1.50), Equation (1.48) can be rewritten as,

$$H_{Anisotropy} = D\left[\mathbf{S}_z^2 - S(S+1)\right] + E\left(\mathbf{S}_x^2 - \mathbf{S}_y^2\right). \tag{1.51}$$

In an octahedral symmetry, the tensor $\mathbf{D}$ follows the relation $D_{xx} = D_{yy} = D_{zz}$. Accordingly, the anisotropy parameters, D and E are zero. In a tetrahedral symmetry, the relation is $D_{xx} = D_{yy} \neq D_{zz}$. Hence, the anisotopy parameter $E = 0$, but $D > 0$.

Three Energy Levels of S = 1 Now a spin system $S = 1$ that is surrounded symmetrically by non-magnetic ions is discussed. For example, a magnetic ion is located in a cubic symmetry. Due to the total spin number, the spin system possesses three degenerated energy levels at zero magnetic field. When a magnetic field is applied along the z-axis, the energy states are split according to the Zeeman effect. Due to the symmetrical environment of the magnetic ion the anisotropy parameters are zero, $D = E = 0$. For $S = 1$, the spin energy states are $|+1\rangle, |0\rangle$, and $|-1\rangle$. The allowed ESR transitions according to the selection rules (Equation (1.13)) are $|+1\rangle \rightleftharpoons |0\rangle$ and $|0\rangle \rightleftharpoons |-1\rangle$. The two transitions show the same resonance field, and only a single resonance signal is obtained as shown in Fig. 1.5 (a).

For a tetrahedral symmetry, the situation is different, as shown in Fig. 1.5 (b). In this case, the crystal field has an axial symmetry along the z-axis. Thus, the three energy states are not degenerated at zero magnetic field due to a gap between the states $|\pm 1\rangle$ and $|0\rangle$. The Hamiltonian of the spin system can be described with the Zeeman term and the anisotropy term. From ESR spectroscopy the gap between the energy levels is obtained by extrapolating the frequency versus magnetic field diagram to zero field. The gap is related to the uniaxial anisotropy parameter D as $\Delta = |D|\left(S_z^2 - (S_z - 1)^2\right)$. In this case, the two transitions do not show the same resonance field due to the gap which is called zero-field splitting (ZFS). Therefore, multiple resonance lines are obtained.

Furthermore, the sign of D depends on the crystal field of the studied spin system. It can be deduced from the ratio of the intensities of the absorption lines in the temperature dependence of ESR spectra. At low temperatures, the lowest energy

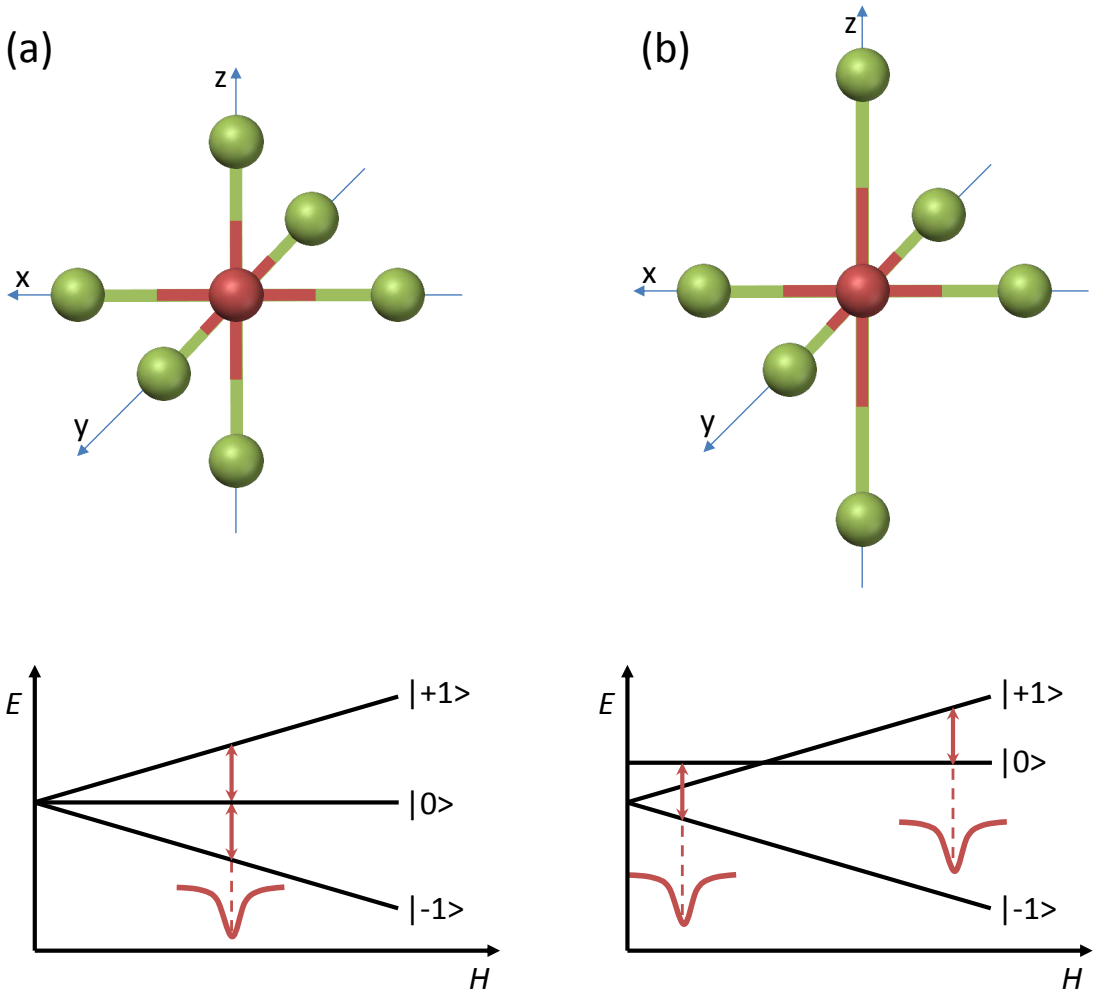

Figure 1.5: Schema of the energy levels of $S = 1$ system in a magnetic fields depending on the local structure. (a) Octahedral symmetry. The energy levels are degenerated at zero field and split in the magnetic field. Two transitions with the same resonance condition are obtained. (b) Tetrahedral symmetry. The two transitions exhibit different resonance fields due to finite ZFS.

states will have the highest population according to the Boltzmann distribution, if D is negative. The intensity of the signal at low magnetic fields will decrease

and the intensity of the signal at higher fields will increase when the temperature increases, i.e. spectral weight of the ESR lines shifts upon heating. In this case, the sign of D is negative, which implies a bistable magnetic ground state. This magnetic anisotropy is called the easy axis. When the weight of the ESR line shifts to the lower field when the temperature increases, the sign of D is positive. In this case, there is a singlet magnetic ground state, which is called the easy plane type magnetic anisotropy.

1.7. Multiple and Giant Spin Hamiltonian

The individual paramagnetic ions interact with each other via the exchange interaction and interact with an external magnetic field due to the Zeeman effect. Also, the ions have their individual magnetic anisotropy. Accordingly, Equation (1.31) can be written as,

$$H = \mu_B \sum_{i}^{j} g_i \vec{S}_i \cdot \vec{H} - J \sum_{ij} \vec{S}_i \cdot \vec{S}_j + \sum_{i}^{j} D_i \left[S_{z,i}^2 - S_i \left(S_i + 1 \right) \right], \tag{1.52}$$

where μ_B is the Bohr magneton, g_i is the g-factor of the ith ion, $\vec{S}_i$ and $\vec{S}_j$ are the spin vectors of the ith and the jth ions, D_i is the axial single-ion anisotropy of the ith ion, and J is the exchange constant. This is the so-called multiple-spin Hamiltonian. When the exchange interaction and the anisotropy of the spin system are comparable, the ground spin multiplet state and the excited spin multiplet state lie close to each other. In this case, the ground spin multiplet state cannot be isolated. The multiple spin Hamiltonian can be applied to these kinds of spin systems.

If the exchange interaction is much larger than the anisotropy of the spin system, the ground spin multiplet state is lowered down in energy. Then, the ground spin multiplet states can be isolated. In the case of SMMs, the spins in the ground state can be approximated to one total spin. Therefore, the Zeeman effect term and the anisotropy term determine the ground state. This is called the giant spin model. The giant spin model Hamiltonian can be written as,

$$H = g\mu_B \vec{S} \cdot \vec{H} + D \left[\vec{S}_z^2 - S \left(S + 1 \right) \right], \tag{1.53}$$

where g and D are the g-factor and the anxial magnetic anisotropy, respectively, of a spin system. Therefore, depending on the characteristics of the spin system and the experimental results, a suitable Hamiltonian should be chosen.

When a system contains many paramagnetic ions, the Hilbert space dimension is too large to solve the Hamiltonian analytically. The Hilbert space dimension of Mn_{12}-acetate, e.g., is 10^8, which corresponds to one spin species. Hence, it is associated to a $10^8 \times 10^8$ dimensional Hilbert space. But the giant spin Hamiltonian includes only one giant spin. The Hilbert space dimension is 21 which is suitable to diagonalize [32]. Therefore, the mesoscopic spin approach can explain the behavior of most SMMs. The giant spin Hamiltonian describes the ground spin system at low temperatures in a large variety of systems.

1.8. Antiferromagnetic Resonance (AFMR)

So far, isolated spin systems surrounded by the ligands have been discussed. Such finite spin systems may be described by rather simple Hamiltonians as shown above. However, in this chapter, spin systems with long range correlations will be discussed, i.e. in the case of long range spin order. Even though the spins are aligned antiferromagnetically or ferromagnetically, a resonance occurs. This phenomenon is called ferromagnetic resonance or antiferromagnetic resonance. The system of antiferromagnetic coupled spins is an interesting one due to the reorientation of spins by the temperature or the magnetic field.

When spins in a compound are correlated, the lowest lying excitations in simple cases are spin wave [33]. The ground state of the ideal ferromagnet consists of perfectly ordered spins at $T = 0$. When N spins are in a one-dimensional chain, the interaction between nearest neighbor spins can be described as,

$$H = -2J \sum_{i=1}^{N} \mathbf{S}_i \cdot \mathbf{S}_{i+1}, \tag{1.54}$$

where $\mathbf{S}_i$ and $\mathbf{S}_{i+1}$ are the neighboring spins, and J is the exchange constant. The first excited state of this ferromagnetic system can be described with one reversed spin. But when all the spins are slightly tilted to share the reversed spin, it costs

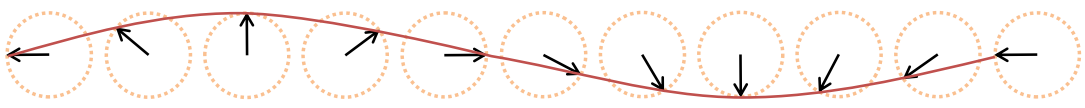

Figure 1.6: A spin wave with one wavelength from a chain of spins.

less energy. This situation creates a wave form of spin misalignment as shown in Fig. 1.6. The plot shows the tilted spins viewed from above with one wavelength. The relative orientations of spins generate oscillations that are spin waves.

In this chapter, antiferromagnetism will be discussed. In a simple Néel-type AFM, this magnetically ordered state has electron spins that are aligned in opposite directions with neighboring spins. A simple antiferromagnetic spin system is the combination of the two sublattices where each exhibits ferromagnetically coupled spins. It is illustrated in Fig. 1.7. The AFMR systems have been studied by Kittel, Nagamiya. Here, a uniaxial antiferromagnetic resonance is discussed.

1.8.1. Susceptibility of a Uniaxial Antiferromagnet

Now let's talk about the antiferromagnet that is constituted by two sublattices, 1 and 2. They have all identical spins and are aligned oppositely to each other along the ± z-axis. The macroscopic magnetizations of each sublattice can be described by $\mathbf{M}_1$ and $\mathbf{M}_2$, which are the sum of the average magnetic moments of the sublattices. In a mean-field approach, exchange fields $\mathbf{H}_{1E}$ and $\mathbf{H}_{2E}$ align the magnetic moments in sublattices, and are proportional to the magnetizations $\mathbf{M}_1$ and $\mathbf{M}_2$. The anisotropy fields $\mathbf{H}_{1A}$ and $\mathbf{H}_{2A}$ describe the effect of anisotropy on the orientation of the magnetizations.

At T = 0 K, all magnetic moments of the magnetic atoms on the sublattices are ordered which leads to zero net magnetism. The magnetization of the iden-

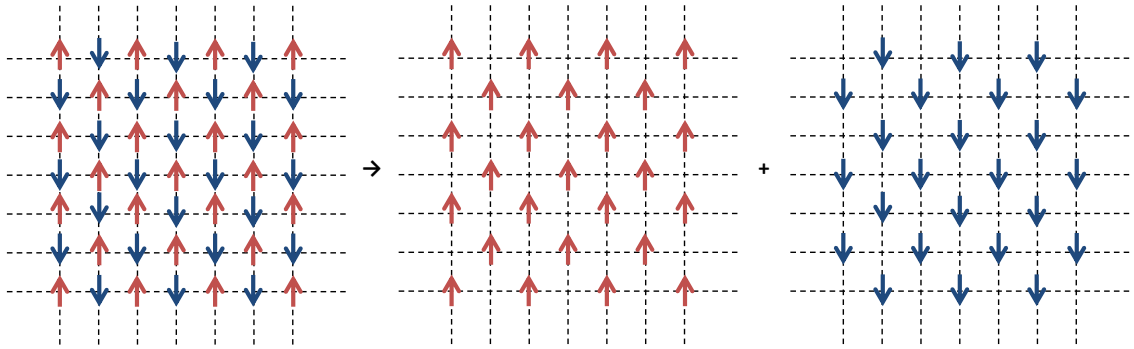

Figure 1.7: Antiferromagnetic lattice with two sublattices. Two interpenetrating sublattices of ferromagnetically aligned spins form the complete antiferromagnetic lattice.

tical sublattices can be considered as $M_1 = M_2 = M$. The anisotropy energy E_A in one sublattice with the angular variation can be written as the product of the anisotropy field $\mathbf{H}_A$ and the magnetization $\mathbf{M}$:

$$E_A = K(\alpha_1^2 + \alpha_2^2) = \sum \mathbf{H}_A \cdot \mathbf{M}, \tag{1.55}$$

where K is the anisotropy constant, and α_i is the direction cosine between the magnetization $\mathbf{M}$ and the z axis. If the preference axis of the anisotropy is the z-axis, the anisotropy field of the z-axis can be described as,

$$H_{Az} = \left(\frac{K}{M}\right)\alpha_i. \tag{1.56}$$

In the case of $K > 0$, the magnetization M is aligned along the z-axis. Also, the exchange field H_E can be considered as,

$$H_E = \lambda M_z, \tag{1.57}$$

where λ is the exchange constant. When small external magnetic fields H_0 is applied along the z-axis, the magnetization $\mathbf{M}$ is aligned along the z-axis. When H_0 is applied perpendicular to the z-axis, the magnetization $\mathbf{M}$ is tilted away from the z-axis by the angle θ. The angle θ is determined when the effect of torques of effective fields the $\mathbf{M}$ is zero. The torques for M_1 in sublattice 1 are

$$\begin{aligned} &|\mathbf{M}_1 \times \mathbf{H}_0| + |\mathbf{M}_1 \times \mathbf{H}_{1E}| + |\mathbf{M}_1 \times \mathbf{H}_{1A}| \\ &\quad = M_1 H_0 \cos\theta - \lambda M_1^2 \sin 2\theta - K \sin\theta \cos\theta = 0, \end{aligned} \tag{1.58}$$

Equation (1.58) can be calculated as,

$$\chi_\perp = \frac{2M_1 \sin\theta}{H_0} = \frac{1}{\lambda + K/2M_0^2}, \tag{1.59}$$

which is independent value of the temperature. However, it is dependent the anisotropy term $K/2M_0^2$. Below the Néel temperature, $\chi_\perp$ and $\chi_\parallel$ different. Generally, $\chi_\perp$ is independent of the temperature. In contrast, $\chi_\parallel$ increases gradually with increasing temperature. When the temperature reaches the Néel temperature, $\chi_\perp$ and $\chi_\parallel$ are equal [34].

When the external field H_0 is strong enough, the antiferromagnetically aligned spins start to align parallel to the field in order to gain Zeeman energy. At a

critical field H_c, a so-called spin-flop occurs where spin rotates roughly perpendicular to the external field direction. Here, the energies, $K - \frac{1}{2}\chi_\perp H_0^2$ (at $H_0 \perp \widehat{z}$) and $-\frac{1}{2}\chi_\parallel H_0^2$ (at $H_0 \| \widehat{z}$), are equal. It can be written as,

$$H_c = \sqrt{\left(\frac{2K}{\chi_\perp - \chi_\parallel}\right)} = \sqrt{\frac{2\lambda K}{1-\alpha}}, \qquad \alpha = \frac{\chi_\perp}{\chi_\parallel} \tag{1.60}$$

In this equation $\chi_\perp$ is approximated by λ^{-1} [18]. When $H < H_c$, the magnetizations M_1, and M_2 are alinged along the $\pm$ z axis. At $H = H_c$, the magnetization jumps from $\chi_\parallel H_0$ to $\chi_\perp H_0$ because the loss in anisotropy is compensated by a gain in Zeeman energy [35]. When $H > H_c$, the M_1, and M_2 start being aligned parallel to the z-axis. This behavior is observed in the magnetization versus magnetic fields [36].

1.8.2. Uniaxial Antiferromagnetic Resonance Theory

In this chapter the treatment of Keffer and Kittel for the uniaxial antiferromagnet is discussed [37,38]. Imagine two identical sublattices, 1 and 2, which are coupled antiferromagnetically. The change of angular momentum is the torques generated by the effective fields on each sublattice [40]:

$$\frac{1}{\gamma_i}\frac{d\mathbf{M}_i}{dt} = \mathbf{M}_i \times \mathbf{H}_{ieff}, \tag{1.61}$$

where γ_i is the gyromagnetic ratio. An effective molecular field $\mathbf{M}_{ieff}$ acting on the sublattices can be described as,

$$\mathbf{H}_{1eff} = \mathbf{H}_{10} + \mathbf{H}_{1E} + \mathbf{H}_{1A}, \qquad \mathbf{H}_{2eff} = \mathbf{H}_{20} + \mathbf{H}_{2E} + \mathbf{H}_{2A}, \tag{1.62}$$

where $\mathbf{H}_{10}$ and $\mathbf{H}_{20}$ are the magnetic fields which are applied on the two sublattices, $\mathbf{H}_{1E}$ and $\mathbf{H}_{2E}$ are the exchange fields, and $\mathbf{H}_{1A}$ and $\mathbf{H}_{2A}$ are the anisotropy fields of the two sublattices, respectively. The exchange fields are proportional to the magnetizations by a constant λ.

$$\mathbf{H}_{1E} = -\lambda \mathbf{M}_2, \qquad \mathbf{H}_{2E} = -\lambda \mathbf{M}_1. \tag{1.63}$$

The anisotropy energy makes the magnetization pointing to a certain crystallographic direction. The anisotropy fields are inversely proportional to the magnetizations by an anisotropy constant K.

$$\mathbf{H}_{1A} = \frac{K}{\mathbf{M}_1}, \qquad \mathbf{H}_{2A} = \frac{K}{\mathbf{M}_2}. \tag{1.64}$$

In case of zero external field, the effective fields acting on the spins of the sublattices 1 and 2 are,

$$\mathbf{H}_{1eff} = -\lambda \mathbf{M}_2 + \frac{K}{\mathbf{M}_1}, \qquad \mathbf{H}_{2eff} = -\lambda \mathbf{M}_1 + \frac{K}{\mathbf{M}_2}. \tag{1.65}$$

Both sublattices have the same g-factor due to the identical spin system on them. In absence of the external magnetic field, one assumes that $|\mathbf{H}_{1A}| = |\mathbf{H}_{2A}| = H_A$, $M_1 = M_2 = M_0$. When the external magnetic field is applied to the z-axis, the magnetizations $\mathbf{M}_i$ are aligned to $\pm$ z-axis. Then, the transverse components M_{ix} and M_{iy} are much smaller than the longitudinal component $M_{iz}(M_{iz} \gg M_{ix}, M_{iy})$, i.e.,

$$M_{iz}^2 = \left[M_i^2 - M_{ix}^2 - M_{iy}^2\right] \approx M_0^2, \tag{1.66}$$

which shows that M_{iz} is almost constant for the angular motion. Depending on the direction of the applied magnetic fields, there are three cases of AFMR resonance modes.

The case of $\mathbf{H}_0 \parallel$ z-axis, when $\mathbf{H}_0 < \mathbf{H}_c$ When $\mathbf{M}_1$ and $\mathbf{M}_2$ are along to the $\pm z$ axis, the equations of motion are

$$\frac{dM_{1x}}{dt} = \gamma \left[(H_0 + H_A - \lambda M_{2z})\, M_{1y} - (-\lambda M_{2y})\, M_{1z}\right], \tag{1.67}$$

$$\frac{dM_{1y}}{dt} = \gamma \left[(-\lambda M_{2x})\, M_{1z} - (H_0 + H_A - \lambda M_{2z})\, M_{1x}\right], \tag{1.68}$$

$$\frac{dM_{2x}}{dt} = \gamma \left[(H_0 - H_A - \lambda M_{1z})\, M_{2y} - (-\lambda M_{1y})\, M_{2z}\right], \tag{1.69}$$

$$\frac{dM_{2y}}{dt} = \gamma \left[(-\lambda M_{1x})\, M_{2z} - (H_0 - H_A - \lambda M_{1z})\, M_{2x}\right]. \tag{1.70}$$

Here, the z-component equations are negligible because only linear effects are considered. Using $M_i^{\pm} = M_{ix} \pm i M_{iy}$, Equations (1.67) - (1.70) become

$$\omega M_1^+ = \gamma \left[(-\lambda M_{1z})\, M_2^+ - (H_0 + H_A - \lambda M_{2z})\, M_1^+\right], \tag{1.71}$$

$$\omega M_2^+ = \gamma \left[(-\lambda M_{2z})\, M_1^+ - (H_0 - H_A - \lambda M_{1z})\, M_2^+\right], \tag{1.72}$$

$$\omega M_1^- = \gamma \left[-(-\lambda M_{1z})\, M_2^- + (H_0 + H_A - \lambda M_{2z})\, M_1^-\right], \tag{1.73}$$

$$\omega M_2^- = \gamma \left[-(-\lambda M_{2z})\, M_1^- + (H_0 - H_A - \lambda M_{1z})\, M_2^-\right]. \tag{1.74}$$

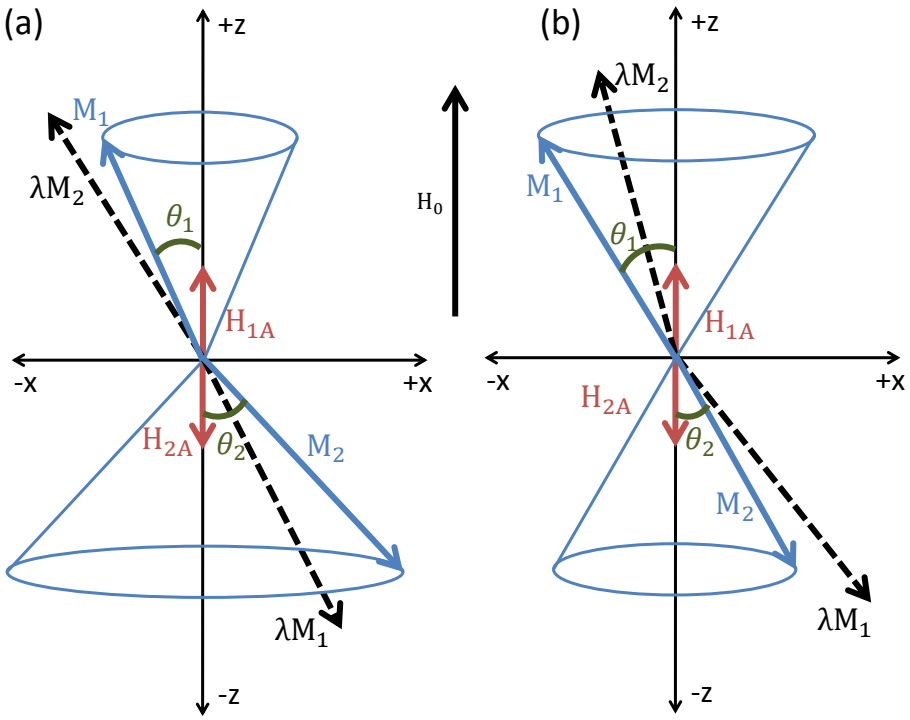

Figure 1.8: Schema of the modes of magnetizations when H_0 is applied along the z-axis. The uniaxial antisotropy fiels H_{iA}, the exchange fields λM_i and the precession angles θ_i are illustrated. The magnetization M_i is rotating with the angles θ_i. (a) The low frequency mode (b) The high frequency mode.

Then, let's assume that the average exchange field $H_E = \lambda\left(M_{1z} - M_{2z}\right)/2$ and $\lambda\left(M_{1z} + M_{2z}\right) = \left(\frac{\chi_\parallel}{\chi_\perp}\right) H_0 = \alpha H_0$ due to a finite $\chi_\parallel$ in the magnetic fields. Hence, the magnetizations on the two sublattices cannot be the same, i.e. $|M_{1z}| \neq |M_{2z}|$. With this assumption, Equations (1.71) - (1.74) are calculated as [39],

$$\omega_l/\gamma = -\left\{\sqrt{\left(2H_E H_A + H_A^2\right) + \left(\alpha H_0/2\right)^2} - H_0\left(1 - \alpha/2\right)\right\}, \tag{1.75}$$

$$\omega_h/\gamma = +\left\{\sqrt{\left(2H_E H_A + H_A^2\right) + \left(\alpha H_0/2\right)^2} + H_0\left(1 - \alpha/2\right)\right\}, \tag{1.76}$$

where "l" and "h" represent the precession modes of low frequency and high frequency, respectively.

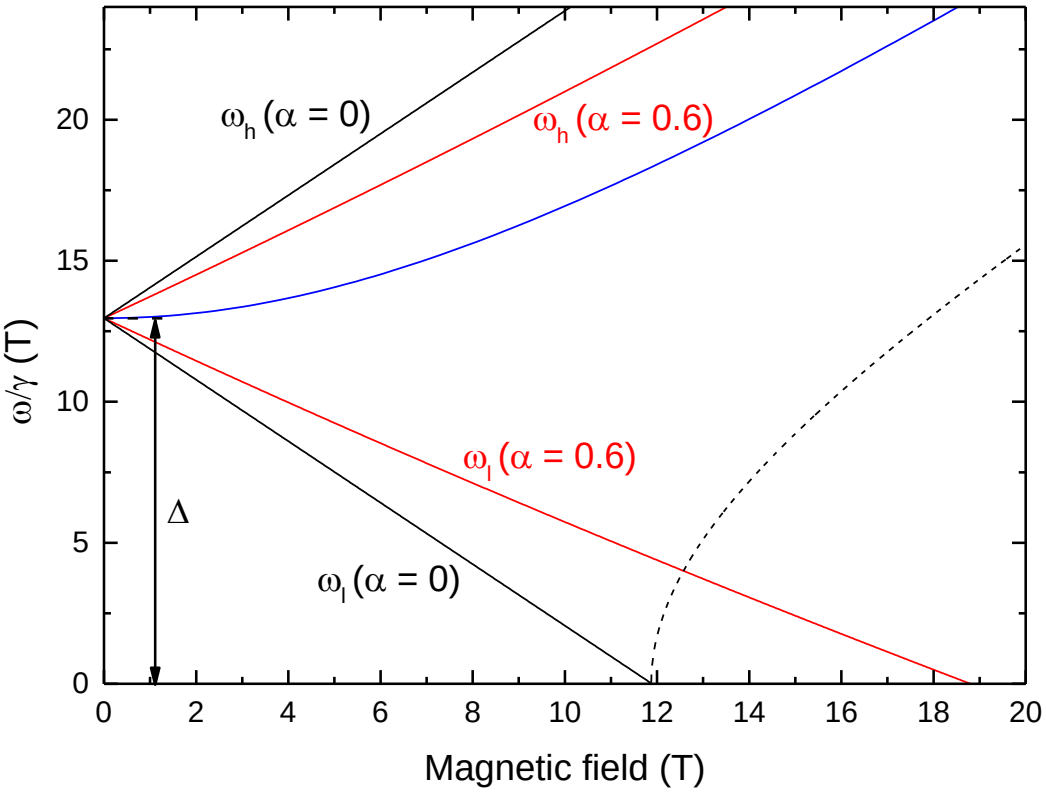

Figure 1.9: Field dependence of uniaxial magnetic AFMR modes with $\alpha = 0$ and $\alpha = 0.6$. The slope with $\alpha = 0$ is steeper than that with $\alpha = 0.6$. The AFMR gap Δ when $H_0 = 0$. The blue line shows resonances at $H_0 \perp \mathbf{z}$ perpendicular mode The dashed line shows the resonance of the spin-flop mode. The spin-flop mode is same in both cases of $\alpha = 0$ and $\alpha = 0.6$.

In absence of magnetic fields, the magnetization of the two sublattices rotate around the axes of the uniaxial anisotropies which is along the $\pm$ z-axis. The ratio of two angles θ_i, which are between the magnetization $\mathbf{M}_i$ and the $\pm$ z-axis, can be defined as $\eta = (\theta_2/\theta_1)$ [42]. However, when the resonance frequency is decreased by γH_0 in the presence of external magnetic fields, this situation is called low frequency mode with $\eta > 1$ (Fig. 1.8 (a)). In contrast, when the resonance frequency is increased by γH_0, it is called high frequency mode with $\eta < 1$ (Fig. 1.8 (b)).

At very low temperature, $\chi_{\parallel}$ of an ideal antiferromagnet approaches to zero.

When $\alpha = \chi_{\parallel}/\chi_{\perp} = 0$, and $H_E = \lambda M_{1z} = -\lambda M_{2z}$, and Equations (1.75) and (1.76) can be written as,

$$\frac{\omega}{\gamma} = \sqrt{(2H_E H_A + H_A^2)} \pm H_0. \tag{1.77}$$

However, the magnetic susceptibility in a real antiferromagnet shows a finite value $\chi_{\parallel}$ at low temperature. When a finite value of α is hence considered, Equations (1.75) and (1.76) can be rewritten as,

$$\frac{\omega}{\gamma} = \sqrt{(2H_E H_A + H_A^2)} \pm H_0(1 - \alpha/2). \tag{1.78}$$

Fig. 1.9 shows the four AFMR resonance modes when the external magnetic field is applied to the z-axis. The modes labelled by the black solid lines occur when $H_0 \parallel \widehat{z}$ above and below the AFMR gap Δ. With the parameter α, the other mode shown with red solid lines occurs. The slope of the lines is smaller with the positive α.

The case of $\mathbf{H}_0 \perp$ z-axis When the anisotropy field is much smaller than the exchange field, the resonance frequency can be described as,

$$\frac{\omega}{\gamma} = \sqrt{2H_E H_A + H_0^2}. \tag{1.79}$$

When $\mathbf{H}_0$ is perpendicular to the magnetizations, M_1 and M_2, and the exchange field H_E is much larger than H_0, H_0 can be neglected, i.e. [41],

$$\frac{\omega}{\gamma} = (2H_E H_A)^{1/2}. \tag{1.80}$$

A ZFS can be calculated by means of Equation (1.80). The ZFS is called the AFMR gap. This resonance mode, the blue line is shown on Fig. 1.9.

The case of $\mathbf{H}_0 \parallel$ z-axis, when $\mathbf{H}_0 > \mathbf{H}_c$ The spin-flop resonance occurs in this case. The resonance equation is written as,

$$\frac{\omega}{\gamma} = \sqrt{H_0^2 - 2H_E H_A}. \tag{1.81}$$

When the magnetic field reaches to the particular field which can overcome the anisotropy field, a spin-flop occurs. Accordingly, the parameter α is not considered. The spin-flop field is,

$$H_0 = (2H_E H_A)^{1/2} . \tag{1.82}$$

The resonance of the spin-flop mode is same in the two cases with $\alpha = 0$ or $\alpha = 0.6$. It is indicated by the black dashed line in Fig. 1.9.

1.9. Simulation

Susceptibility $\chi(T)$ Analysis To simulate the magnetic susceptibility curve of small spin clusters, the program *julX* is used [43]. This program is based on the Hamiltonian, Equation (1.31), with maximum of four spins. It calculates the magnetic moments from first order derivatives of the eigen values, E_i, $\mu_i = -dE_i/dB$ without eigenfunctions. With eigenfunction it can calculate it as $dE_i/dB =< \Psi \mid dH/dB \mid \Psi >$ [44].

Spectra Simulation To analyze and reproduce the experimental ESR spectra, the *EasySpin* of the MATLAB toolbox which is available for free is used. This program enables calculating spin systems with finite number of electron spins and nuclear spins [45]. There are many functions to modify the Hamiltonian depending on the spin system. For example, one can build up the program sources for the giant spin model or the multiple spin model, etc.

Fitting with the Lorentzian Function In chapter 1.1.2, there is explanation of the Lorentzian function of Equation (1.26). Normally, most compounds for ESR spectroscopy are constituted by ideal particles with homogeneous environment [46]. Hence, most ESR spectra have the shape of a Lorentzian. From the fitting with the Lorentzian function, relevant information on the magnetic properties of the materials under study can be analyzed. The information on linewidth, central field and area are obtained by the fitting. As discussed before, the intensity I of the line is proportional to the susceptibility χ. The intensity I is also proportional to the area of the line A. Therefore, the area A from the local static spin susceptibility is to be compared to the magnetic susceptibility χ.

2. Experimental Technique

The ESR experiment is performed with a sample placed in external magnetic fields under irradiation with microwaves and detected the transmitted radiation [20,47]. To perform the ESR measurements, external magnetic fields, microwaves, and a probe to place the sample and to propagate microwaves are required. In this chapter, the high field and high frequency ESR setup applied will be described.

2.1. High Field - High Frequency ESR Setup

High field and high frequency (HF)-ESR at Heidelberg University is a combination of a millimeter wave vector network analyzer (MVNA) [48] and a cryogenic superconducting magnet. The MVNA acts as the microwave source and detector. It enables to generate microwaves in a broad frequency range, from 8 GHz to 1000 GHz. This broad tunable frequencies are multiplied from fundamental frequencies of 8 GHz to 18 GHz which are generated by yttrium iron garnet (YIG) oscillators. The fundamental frequency is multiplied by Schottky diodes.

The MVNA is controlled by a computer. A schematic drawing of the operation principle within the frequency range of 8 GHz $\sim$ 300 GHz is shown in Fig. 2.1. The actual frequency for measurement is managed by two Schottky diodes. Firstly there are a harmonic generator (HG) and a harmonic mixer (HM). The two YIGs generate the frequencies F_1 and F_2, and the source frequency F_1 is multiplied by a harmonic number N by the Schottky diode in the HG [49]. Then, the HG emits the wave of the harmonic frequency NF_1 to the waveguide. This wave propagates to the sample. After a coupling between the wave and the sample in magnetic fields, the microwave propagates back and it is mixed with the wave NF_2 in the HM. This frequency NF_2 is multiplied at HM by the harmonic number N. Frequencies NF_1 and NF_2 are mixed at the Schottky mixer HM. It generates the intermediate frequency F_{if}, according to $F_{if} = NF_1 - NF_2 = NF_{diff}$, in order to down convert the radiation frequency. F_{if} is in the MHz range and enters to the network analyzer with an information of the amplitude and the phase which is compared with the reference signal.

Phase lock loop (PLL) generates an output signal according to the phase of an input signal. Here the PLL performs the phase locking of the signals from the two YIGs to minimize the phase noise. The F_2 is stabilized in accordance with the F_1 through the PLL. Hence, the PLL compares the F_{diff} and the reference frequency f [50]. Actually, the overall process is determined by the harmonic number which select the operating frequency F_{of} of the MVNA receiver. There

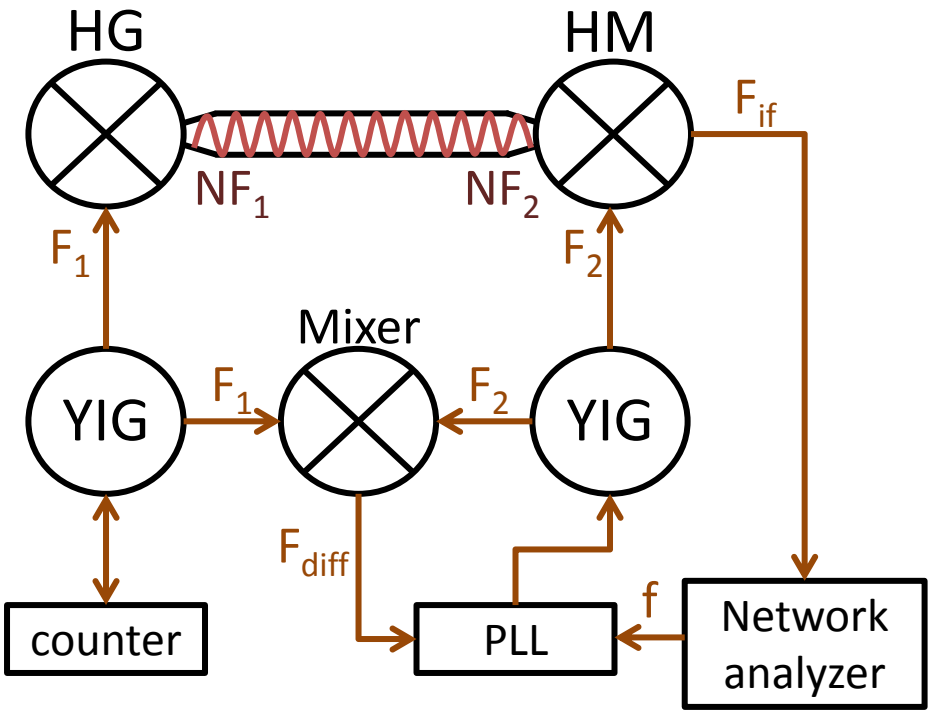

Figure 2.1: Schema of the working principle of high field and high frequency ESR spectroscopy. The harmonic generator (HG) and harmonic mixer (HM) multiply N times of the fundamental frequencies F_1 and F_2 which are generated by YIGs. F_1 and F_2 are slightly different frequencies because the YIG generated F_2 is stabilized by another YIG. The HM multiplies the NF_1 to the NF_2. Its result F_{if} in the MHz range is compared with the generated signals from the YIGs in the network analyzer and the phase lock loop (PLL).

are three operating frequencies, 9.010488 MHz, 34.010488 MHz, and 59.010488 MHz. The operating frequency is decided depending on the harmonic N. The previously described reference frequency f is decided by the operating frequency, $f = f_{of}/N$. And the F_{diff} is kept with an equal value of the reference frequency f by PLL. Depending on desired frequencies, the Schottky diodes multiply the frequencies by various harmonic numbers: X-band (ν = 8 - 18 GHz) by $N = 1$, K-band (ν = 18 - 28 GHz) by $N = 2$, V-band (ν = 44-74 GH) by $N = 4$, W-band (ν = 75-110 GHz) by $N = 6$, and D-band (ν = 110-170 GHz) by $N = 9$, and higher frequencies by higher N. Reaching higher frequencies is possible by

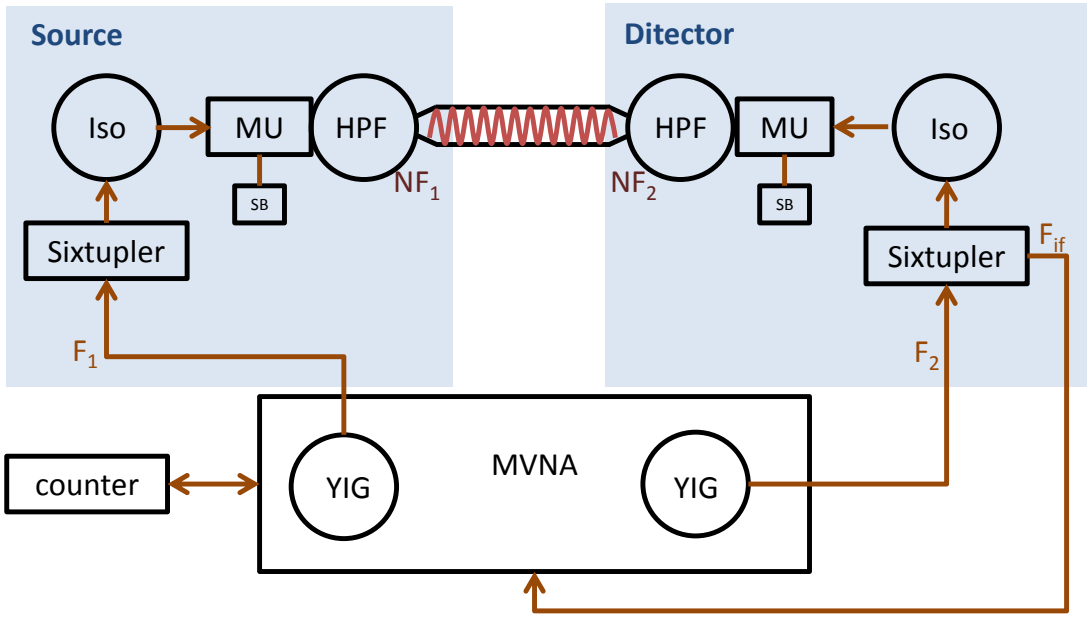

Figure 2.2: The configuration of the ASAs system. The sextupler provides a frequency range of 62 - 112 GHz. The combination of the two frequencies from the source and the detector is applied to the internal network to stabilize frequencies generated from YIGs.

applying the extensions of an automatic source association (ASA)-1 and ASA-2. The ASAs system enables to achieve high frequencies by applying multipliers. The configuration of the ASAs system is shown in Fig. 2.2. Both sides of the source (ASA-1) and detector (ASA-2) are connected with the multiplier $\times 6$ (Sextupler). Basically, the microwave is multiplied six times of the fundamental frequencies, F_1 and F_2 in the sextupler which covers the range of 62 - 112 GHz. The multiplied waves from both sides propagate Faraday isolator (Iso) and single Schottky multi-harmonic tunalble multipliers (MU). The waves are multiplied again at MU which performs the mechanical tuning. The self-bias (SB) boxes are connected to the cap of the MU to check the self-current because these Schottky diodes are fragile. By that, it is possible to check the emitting, the brokenness of the Schottky diode and the coupling of microwave with the Schottky. After passing the MU, the signal passes the high pass filter (HPF) which cuts off the harmonic signals lower than the concerning harmonics. The two harmonic microwave NF_1 and NF_2 are mixed at the mixer of the ASA-2 extension. Then the beat frequency

$F_{if} = NF_1 - NF_2$ is inserted to the internal network of the MVNA for analysis.

2.2. Waveguide and Cryostat

The microwave from the source propagates along a cylindrical waveguide as shown in Fig. 2.3. The length of a probe is 180 cm, because a sample will be mounted in the superconducting coils which are located at the bottom of the cryostat. The ends of the top of the two tubes are inserted to tapered horns which are connected with the diodes. The tapered horns help concentrating the microwaves. The generated microwave from the source part is reflected on a 45 degreed mirror on the top of the probe and propagates to the sample which is mounted of the bottom of the tube. The microwave couples with the sample. After the coupling between the microwave and the sample, the transmitted microwave reflects twice on 45 degreed mirrors. Finally the wave is detected by the MVNA.

If an electromagnetic wave propagates along a waveguide (the x-axis), it can be described as follows,

$$\mathbf{E}(x,t) = \mathbf{E}_0 e^{i(\kappa x - \omega t)}, \quad \mathbf{B}(x,t) = \mathbf{B}_0 e^{i(\kappa x - \omega t)}, \tag{2.1}$$

where $\mathbf{E}(x,t)$ and $\mathbf{B}(x,t)$ are perpendicular to each other, κ is the wave number and ω is the angular frequency.
If the waveguide is a perfect conductor, $E = B = 0$ is satisfied inside of the waveguide. Hence, the boundary condition on the surface can be

$$\mathbf{E}_{\parallel} = 0, \qquad \mathbf{B}_{\perp} = 0. \tag{2.2}$$

The electromagnetic waves satisfy the Maxwell equations inside the waveguide. The resulting electromagnetic wave propagation along the x-axis can be described as follows [52],

$$\left[\frac{\partial^2}{\partial y^2} + \frac{\partial^2}{\partial z^2} + \left(\frac{\omega}{c}\right)^2 - \kappa^2\right] E_x = 0, \tag{2.3}$$

$$\left[\frac{\partial^2}{\partial y^2} + \frac{\partial^2}{\partial z^2} + \left(\frac{\omega}{c}\right)^2 - \kappa^2\right] B_x = 0. \tag{2.4}$$

There are three modes from the solutions of Equations (2.3) and (2.4): a transverse electric (TE) mode at $E_x = 0$, a transverse magnetic (TM) mode at $B_x = 0$ and a transverse electromagnetic (TEM) mode at $E_x = B_x = 0$. Electric and

magnetic fields of TE and TM modes are perpendicular to the direction of propagation. The x-components, B_x and E_x, of TE and TM mode are parallel to the direction of propagation. A TEM mode cannot occur at an empty waveguide. A TEM mode is applied to transmission lines which use two conductors like coaxial cables, microstrips and so on [51]. A TE mode and a TM mode are applied to a general metal waveguide.

Let's think about the TE mode propagating in a rectangular waveguide with height a and width b along the y and z axes ($a \geq b$) [52]. Considering the boundary condition, the wave number $\kappa = \sqrt{(\omega/c)^2 - \pi^2(m/a)^2 + (n/b)^2}$ is calculated from Equation (2.4) [52]. The integers m and n are the number of half wavelengths of a and b, respectively. Considering an attenuated wave due to a imaginary part of κ, the cutoff frequency can be determined as [52, 53],

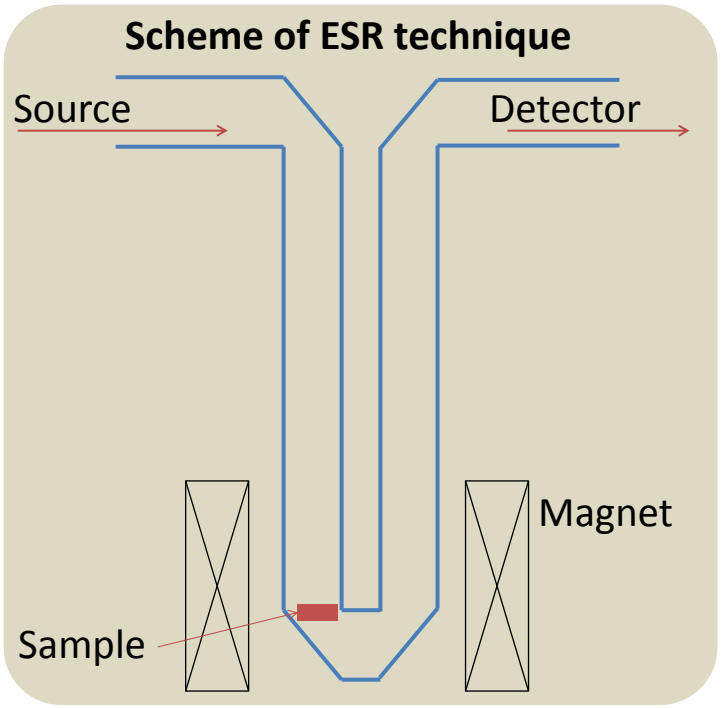

Figure 2.3: Schema of a probe for transmission. The probe preserves and carries microwaves. The entries on the top parts are connected with diodes.

$$\omega_{cut} = c\pi\sqrt{\left(\frac{m}{a}\right)^2 + \left(\frac{n}{b}\right)^2}. \tag{2.5}$$

In the case of a cylindrical waveguide, the cutoff frequency can be written as,

$$\omega_{cut} = c\frac{(k_c r)_{mn}}{2\pi r}, \tag{2.6}$$

where r is the radius of the waveguide, $(k_c r)_{mn}$ is the nth root of the mth-order Bessel function $J'_m(k_c r)$ [20]. The parameter $(k_c r)_{mn}$ is 1.84 and 2.405 for TE_{11} and TM_{01} modes, respectively. When an applied frequency is below the cutoff frequency, it cannot propagate through a waveguide. Furthermore, because of the Ohmic losses in the waveguide walls, the microwave power is attenuated by the factor $e^{-\alpha_R z}$ with the attenuation constant α_R [20]. The attenuation constant α_R is proportional to the surface resistance R_s. Accordingly, a waveguide of an ESR probe consists of brass and gold deposited brass. The overall of the two tubes are made of brass with $\alpha_R = 5.01\times\ 10^{-2}\ \Omega$ at 10 GHz [54]. And the bottom of the brass tubes are plated with gold which has a lower surface resistance of $3.12\times\ 10^{-2}\ \Omega$ at 10 GHz [54]. The waveguide consists of two cylindrical tubes with the diameter of 9 mm which implies the cutoff frequency of ∼9.7 GHz. These tubes allow using of a broad range of frequencies, which can be generated by the different settings of diodes.

ESR experiments are performed with a superconducting magnet system from Oxford Instruments. The magnet reaches the magnetic fields of 18 T. There is a variable temperature insert (VTI) in the inner part of the magnet coils. The VTI enables the experiment from low temperature $T = 2$ K to the high temperatures $T \simeq 300$ K. The height of the cryostat due to the space for the reservoir of the liquid He is the decisive factor for the length of the probe of about 180 cm. The total length for the transmission of microwaves is around 4 m. The attenuation during propagation through the probe is about 0.3 dB/m at an applied frequency of 300 GHz.

Part III.
Frustrated Transition Metal Oxides

3. Introduction to Frustrated Spin Systems

In addition to the bare size of magnetic coupling, one of components governing the magnetic ordering of the spin lattice is the geometrical arrangement of the spins. When a spin cannot simultaneously satisfy all magnetic couplings acting on it, the onset of long-range order can strongly suppressed as compared to the mean-field value. Such cases are due to a competition between different kinds of interaction due to the geometrical structure of its lattice [55]. It is called the magnetic geometrical frustration or frustration.

The study of the frustrated spin system began by G.H. Wannier with antiferromagnetically coupled spins on a triangular lattice in 1950 [56]. The word of frustration was introduced by G. Toulouse and J. Villain in 1977 [57, 58]. Representative frustrated lattices are triangular, one-dimensional spin chains, or Kagomé lattice. The spins in those lattice have an antiferromagnetic coupling with the nearest neighboring spins. It is ambiguous to predict the physical properties of the ground state due to the geometrical constraints. Therefore, the frustrated spin system is interesting to study.

Let's think about the triangular lattice with three spins on its vertices, respectively. Their coupling is expressed by the exchange constant J. When all the spins on the ground state are parallel to each other, $J > 0$, the satisfied spin configuration is clear and they couple ferromagnetically to each other. However, when the spins couple antiferromagnetically to each other, $J < 0$, the spin configuration of a lattice is ambiguous. Fig. 3.1 shows some examples of frustrated spin systems. Fig. 3.1 (a) shows the triangular lattice where the interactions of the spin pairs are not satisfied. When the three spin pairs, J_1, J_2 and J_3 are coupled antiferromagnetically in a strict ising situation, the direction of one spin is unpredictable. Contrastively, in the square lattice, the spin interactions can be satisfied for all the antiferromagnetic spin pairs (Fig. 3.1 (b)).

There is another case of a frustrated spin system, i.e., the one-dimensional spin chain. Fig. 3.1 (c) shows a coexistence of ferromagnetic and antiferromagnetic interactions in the spin chain system. For example, there is a ferromagnetic cou-

plings J_1 between neighboring spins and antiferromagnetic coupling J_2 with next nearest neighboring spins on the one-dimensional chain lattice. It is difficult to determine the ground state which depends on the so-called frustration parameter $\alpha = J_2/J_1$ [59]. When the magnitude of the exchange interaction is like as $J_3 < J_1, J_2$, all the spins align parallel on the ground state. However, if J_3 is comparable to J_1 and J_2 strong enough, the state of the spins cannot be determined properly.

The ESR spectroscopy allows to study magnetic properties of the ground state of frustrated spin systems. Especially the high field and high frequency ESR technique is helpful to study a frustrated spin system with a big anisotropy gap. Hence, the experimental result will offer information, like as g-factor, linewidth and so on. The analysis of the data yields interesting information like anisotropy gap, spin-flop, etc. From them, one can have an opportunity to investigate the behavior of the spin system in the ground state as well as studying the evolution of order in the temperature range between $T = 0$ and the actual 3D ordering temperature T_N.

In my thesis, I will discuss two different kinds of spin system, the honeycomb spin system and the Kagomé lattice.

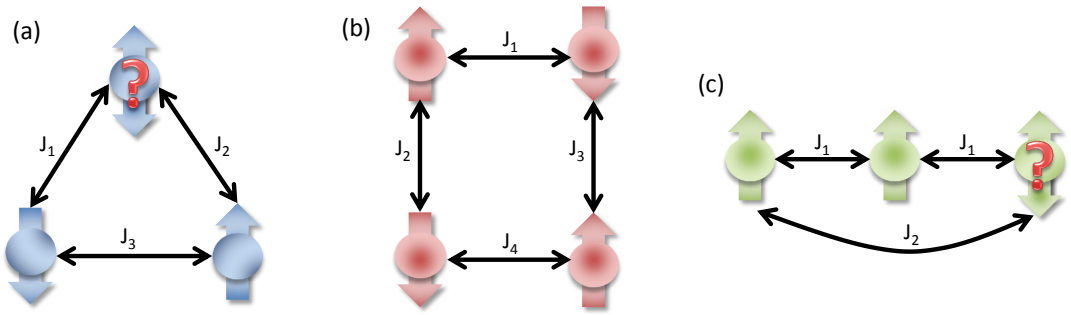

Figure 3.1: Various geometrical crystal lattices which have spins coupled antiferromagnetically. (a) Triangular lattice with antiferromagnetic couplings, J_1, J_2, J_3. The last spin is frustrated due to the constraints of the lattice geometry. (b) Square lattice with antiferromagnetic coupling. All the spin pairs are satisfied. (c) One-dimensional chain lattice with coexistence of ferromagnetic and antiferromagnetic couplings. Its spin system can be frustrated by the interaction of J_2.

4. Honeycomb-lattice spin systems $Na_3Ni_2SbO_6$ and $Li_3Ni_2SbO_6$

In this chapter, the two materials $Na_3Ni_2SbO_6$ and $Li_3Ni_2SbO_6$ are studied. Both are correlated spin systems with hexagonal structure by constituent Ni^{2+} ions in one plane. It is called, as well, honeycomb structure. This structure is, e.g., used to make cathodes for Na-ion batteries due to its capacity [60]. The two materials $Na_3Ni_2SbO_6$ and $Li_3Ni_2SbO_6$ began to be studied for possible development of Na-ion batteries, which can have a large scale energy storage because of the abundance and low price of Na [61]. Not only its value as a battery but also the physical phenomena appearing in a complex spin lattice make them interesting to be studied.

From the geometrical point of view, a system with honeycomb structure is not frustrated by antiferromagnetic interactions. But there can be a strong magnetic fluctuation due to their low coordination [62]. The spin gap behaviors of those systems can be studied by the temperature dependence of the magnetic susceptibility χ and the specific heat C [63,64]. In this chapter, the family of the honeycomb spin system is studied by HF-ESR.

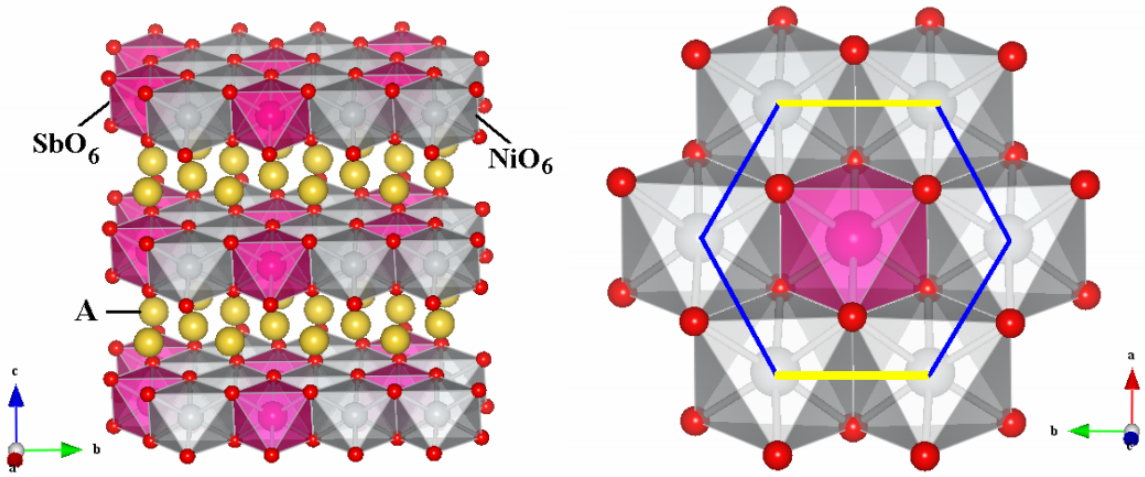

Figure 4.1: Structure of $Na_3Ni_2SbO_6$ [65]. The octahedral structure is formed by SbO_6 and NiO_6 in ab plane. There are Na^+ ions between layers. In ab plane Ni^{2+} ions form a hexagonal structure with Sb^{2+} ions in centers of the hexagons.

4.1. Crystal Structure and Magnetic Properties

$Na_3Ni_2SbO_6$ and $Li_3Ni_2SbO_6$ are provided by the group of Prof. V.B. Nalbandyan at Southern Federal University [65]. For $Na_3Ni_2SbO_6$, one Ni^{2+} ion constitutes the octahedral structure with six O^{2-} ions which are located edges of the octahedron. In the ab plane the six octahedral NiO_6 structures form a hexagonal lattice. Fig. 4.1 shows the overall structure of $Na_3Ni_2SbO_6$ and the hexagons in the ab plane. And the center place of the hexagons is filled with the octaheral SbO_6. Na^+ ions are located between the hexagon layers. Fig. 4.2 shows the exchange couplings between Ni^{2+} ions [66]. In the ab plane Ni^{2+} ions are coupled both antiferromagnetically and ferromagnetically. Ni^{2+} ions in ferromagnetic zigzag chains are coupled with $J_2 = -22$ K (FM) which is indicated by the green line [66]. The distance between Ni^{2+} ions is 3.06 Å [66]. The ferromagnetic chains are coupled antiferromagnetically to each other. Their exchange coupling is $J_1 = 15$ K (AFM) and their distance is 3.05 Å [66]. Ni-O angles in NiO_6 octahedral structure are between 81.2° and 96° [66].

$Li_3Ni_2SbO_6$ has the same structure as $Na_3Ni_2SbO_6$ as shown in Fig. 4.1. The ionic ion Na^+ is sustituted by the Li^+. Layers of honeycomb lattice which consists of octahedral structures of NiO_6 and SbO_6 are separated by the ionic ions

(a)

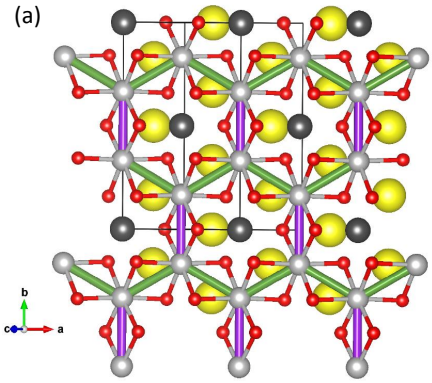

(b)

J_1	15 K (AFM)
J_2	-22 K (FM)
J_3	0 K
J_5	1 K (AFM)

Figure 4.2: (a) Schema of exchange couplings in $Na_3Ni_2SbO_6$. (b) Table of the exchange coupling resultings from band structure calculation [66]. The coupling between nearest neighbors J_1 is antiferromagnetic indicated by the purple line, the coupling between next nearest neighbor J_2 is ferromagnetic (green line). The next nearest neighbor coupling is J_3 and the coupling between the honeycomb layers is J_5 [66].

Li^+ [65]. Ni^{2+} ions are coupled ferromagnetically with $J_2 = -25$ K to lead zigzag chains. The distance between Ni^{2+} ions is 2.99 Å [66]. Those chains are coupled antiferromagnetically with $J_1 = 18$ K and their distance is 2.98 Å. The distance between Ni^{2+} ions on $Li_3Ni_2SbO_6$ is shorter than the one on $Na_3Ni_2SbO_6$. Because the ionic radius of Na^+ is larger than Li^+. It is caused by the different spin configurations between $Na^+(2p^6)$ and $Li^+(1s^2)$. Ni-O in NiO_6 octahedral structure have angles between 83.4° and 94.9° [66].

The magnetic measurements and the X-band ESR measurements on $Na_3Ni_2SbO_6$ have been done by the group of Prof. E. A. Zvereva in Moscow [65]. The magnetic susceptibility was measured with a Quantum Design SQUID magnetometer at $B = 0.1$ T within $T = 1.8 - 300$ K. The magnetic susceptibility curve steadliy increases as the temperature decrease. Below the Néel temperature of 17 K the susceptibility drops. This phenomenon indicates antiferromagnetic ordering. The inverse susceptibility is analyzed by a Curie-Weiss law with a diamagnetic term. It reveals a positive diamagnetism $\chi_0 \sim 1 \cdot 10^4$ emu/mol with the positive Curie-Weiss temperature of $\Theta \sim 12$ K which indicates dominating ferromagnetic coupling [65]. Band structure calculations indicate the existence of the ferromagnetic and antiferromagnetic couplings in the material [66]. Even though the antiferromagnetic coupling is observed from the shape of susceptibility curve, the ferromagntic coupling is predominant. The effective magnetic moment of $4.4\,\mu_B$ is calculated by the Curie constant [65]. The effective g-factor is 2.15 [65]. The saturated magnetization is $\sim 4.3\ \mu_B$ as taken from the magnetic field dependence of the static magnetization up to 25 T.

$Li_3Ni_2SbO_6$ has similar magnetic properties as $Na_3Ni_2SbO_6$. Its susceptibility curve increases when the temperature decreases. Then it drops below $T_N = 15$ K which shows the antiferromagnetic ordering transition. By using the Curie-Weiss law the inverse susceptibility is analyzed. The Curie-Weiss temperature is $\Theta \sim 8$ which indicates predominant ferromagnetic coupling between Ni^{2+} ions [65]. The effective magnetic moment is $4.3\,\mu_B$ [65]. The effective g-factor from the Curie-Weiss analysis of the static susceptibility is 2.5 which is corresponding to a total spin $S = 1$ of Ni^{2+} ion [65].

4.2. HF-ESR: Experimental Results and Discussion

$Na_3Ni_2SbO_6$ The HF-ESR measurement were performed on loose powder of $Na_3Ni_2SbO_6$ in the frequency range of 50 - 560 GHz at the temperature $T = 4$ K. Fig. 4.3 shows ESR signals at 4 K. At $f = 470$ GHz three AFMR peaks are

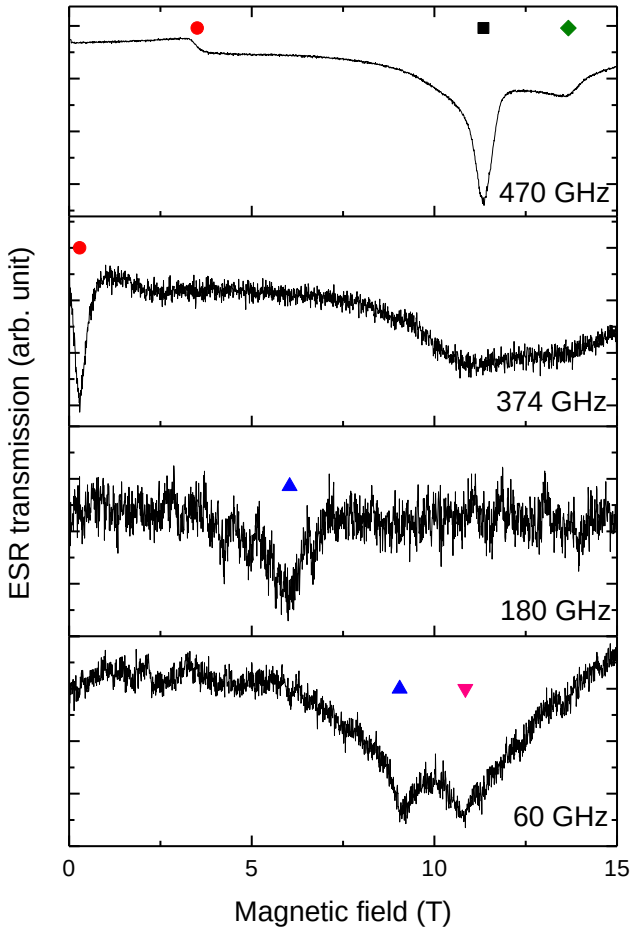

Figure 4.3: AFMR signals at 4 K in loose poder of $Na_3Ni_2SbO_6$. At $f = 470$ GHz three AFMR peaks are obtained. At 374 and 180 GHz, there is only one AFMR peak. At 60 GHz, there are two AFMR peaks around 10 T. Symbols are corresponding to the experimental data in Fig. 4.4.

obtained. There is only one AFMR line at $f = 374$ and 180 GHz. At 60 GHz, there are two AFMR peaks at around 10 T.

Fig. 4.4 shows the frequency dependence of the ESR resonance fields at $T = 4$ K. In this case, four resonance modes are obtained since powder particles are self-oriented in the magnetic fields. First of all, the first resonance mode shows the behavior of the spins when the magnetic field is perpendicular to the easy

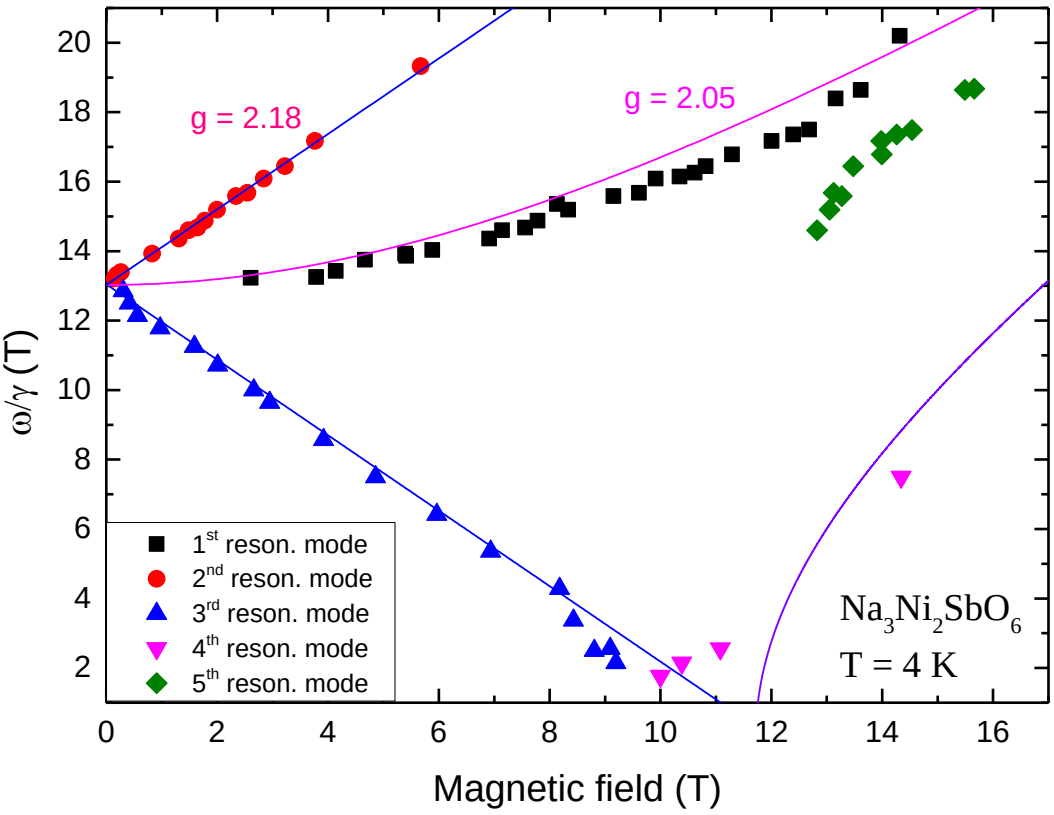

Figure 4.4: Experimental data ω/γ vs. magnetic field and in terms of the AFMR model simulation of the magnetic field dependence of ESR data. When the easy axis is parallel to **H**, the second and third resonance modes show the g-factor of 2.18. At zero field the AFMR gap is 12.8 T. When the easy axis is perpendicular to **H**, it reveals the g-factor of 2.05. At $H > H_c$ the spin flop region is simulated.

axis. The second and third resonance modes are obtained in the low field region when the field is parallel to the easy axis. They correspond to the high and low frequency modes which are introduced in chapter 1.8. Finally, the fourth resonance mode occurs in the spin-flop region if the magnetic field is applied along the easy axis.

The average of the total magnetic moments of the sublattices can be described as macroscopic sublattice magnetization $\mathbf{M}_i$ of each sublattice. $\mathbf{M}_1$ and $\mathbf{M}_2$ are almost parallel to $\pm\,\hat{z}$ in presence of the magnetic field. Their equations of motion

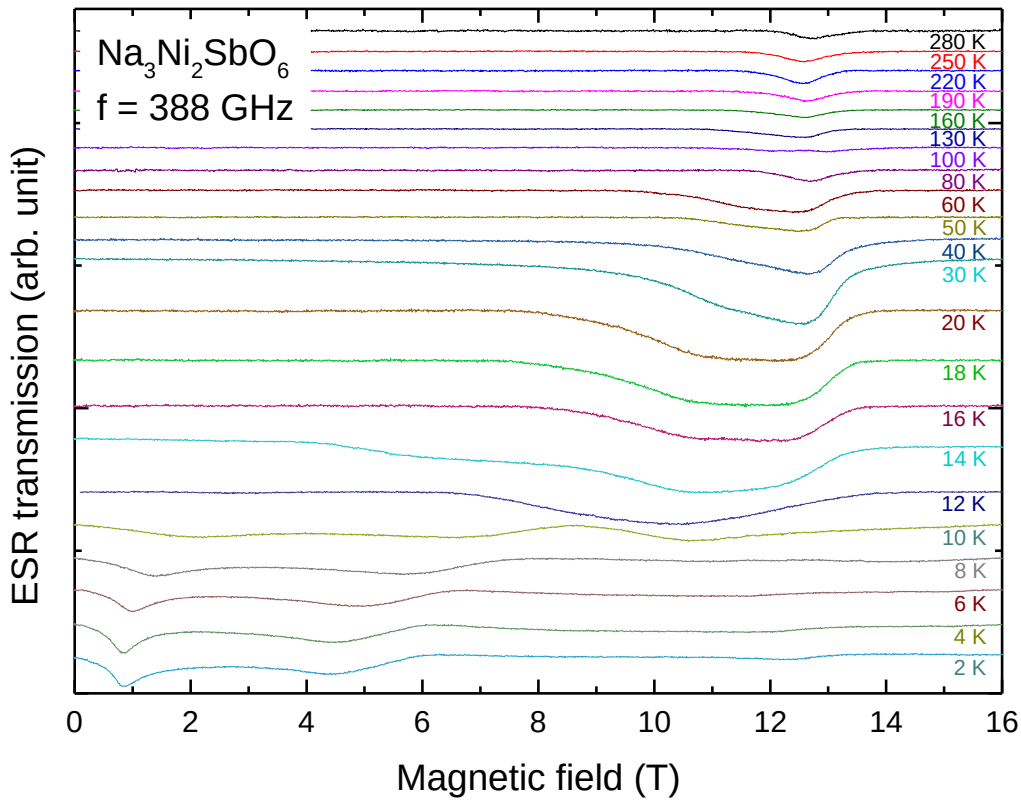

Figure 4.5: The temperature dependence of ESR spectra at 388 GHz. At $T < 10$ K, three resonance peaks are appeared on each spectrum. They move to higher magnetic fields when the temperatures increase. The intensity of the ESR spectra decrease at high temperature.

are described by Equations (1.75) and (1.76). The anisotropy field is assumed very small compared to the exchange field. Hence, the squared anisotropy field H_A^2 in both equations is neglected. Then those equations can be written as,

$$\omega/\gamma = \sqrt{2C + (\alpha H_0/2)^2} + H_0\,(1 - \alpha/2)\,, \tag{4.1}$$

where $C = H_A H_E$, $\alpha = \chi_\parallel/\chi_\perp$ and $H_0 = (g/2)H$. The blue solid lines in Fig. 4.4 are fits to the data by means of Equation (4.1). The obtained parameters are $C = H_A H_E \cong 82$ T, $\alpha \cong 0.0064$ and g-factor of 2.18. At zero magnetic field, the AFMR gap is $\omega/\gamma = 12.8$ T.

The saturated magnetization is 4.3 $\mu_B/f.u.$ at 4.2 K, i.e., 23.9 J/T^{-1}/mole. And the susceptibility at 4 K is 0.05 erg/G^2/mole (= 0.5 J/T^2/mole) [65]. From the parameter $\alpha = 0.0064$, $\chi_\perp$ can be approximated. The inversed exchange constant λ^{-1} is proportional to $\chi_\perp$ [67]. Hence, the calculation reveals an exchange constant λ of $\sim$ 1.34 mole T^2/J which leads to the exchange field $H_E = \lambda M_0 \cong 32$ T. The parameter $H_E H_A$ is the multiple of λK. Hence, an anisotropy constant K of $\sim$ 61 J/mole is calculated. The anisotropy field is around 2.55 T which is not a small value to be neglected. The frequency dependent ESR data are hence by following new equations including H_A. The modes for $H \parallel \hat{z}$ are simulated by [68],

$$\omega/\gamma = \sqrt{2H_E H_A + H_A^2 + (\alpha H_0/2)^2} + H_0\,(1 - \alpha/2)\,. \tag{4.2}$$

The initial parameters are $H_E = 32$ T, $H_A = 2.55$ T and $\alpha = 0.0064$. The simulation lines by applying Equation (4.2) are plotted in red in Fig. 4.4. Above the AFMR gap, the simulation lines (blue lines) reproduce the red dots well. Below the gap, there is a slight discrepancy between the simulation lines (blue lines) and the third resonance mode.
The modes for $H \perp \hat{z}$ are simulated by [68],

$$\frac{\omega}{\gamma} = \sqrt{2H_E H_A + H_A^2 + (H_A/H_E)H_0^2 + H_0^2}. \tag{4.3}$$

The pink line representing the best simulation of the first resonance mode is shown in Fig. 4.4. It reveals the g-factor of 2.05. The spin-flop mode is simulated with the same parameters of the other resonance modes (purple line).

The temperature dependent ESR spectra are measured at frequencies above and below the AFMR gap of 12.8 T ($\sim$ 358.4 GHz). Fig. 4.5 shows the temperature dependence of ESR spectra at 388 GHz which is above the AFMR gap. The spectra at low temperature are very broad. There are three resonance signals around 1 T, 4 T and 11 T, respectively. When the temperature increases, the linewidth of the ESR spectra decreases. At the Néel temperature $T_N = 17$ K, the resonance peak shifts to high magnetic field. By increasing the temperature, the intensity of the ESR spectra also decreases.

The temperature dependent ESR spectra are analyzed by Lorentzian functions. Fig. 4.6 shows the temperature dependence of the resonance fields. The main feature is the strong shift of the resonance field when cooling beelow T_N. Above T_N, there is a relative small shift as compared to the low field one. Here, the

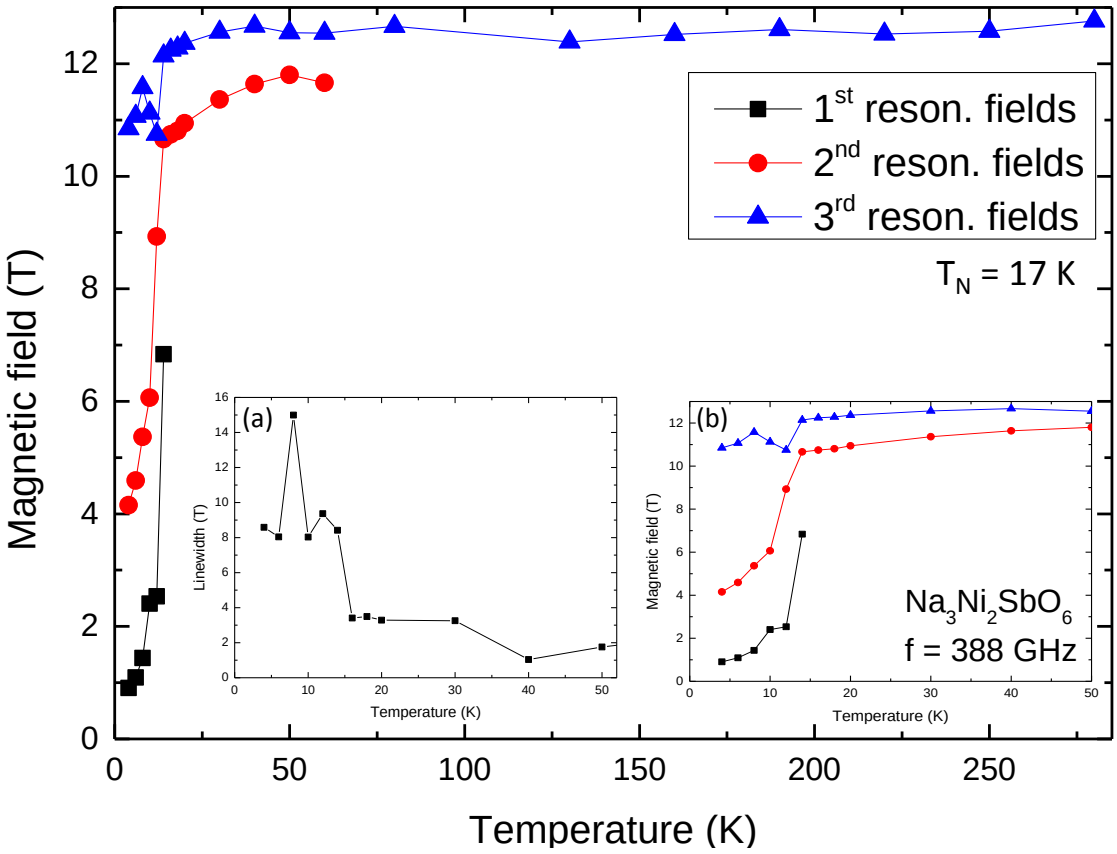

Figure 4.6: Temperature dependent resonance fields at 388 GHz above the AFMR gap. Insert: (a) The sum of the linewidths of the ESR resonance peaks. (b) The resonance fields shift to the higher magnetic fields in vicinity of T_N, and ESR peaks are merged.

resonance peaks shift to higher field upon heatings. Fig. 4.6 (b) shows the shifting of signals at $T < T_N$ (= 17 K) in more detail. The shifts of the resonance field below T_N occurs due to the developed internal field which is regarded as the antiferromagnetic resonance [69, 70]. The temperature dependence of the sum of the linewidths of the three resonance ESR peaks, Δ_L is plotted in Fig. 4.6 inset (a). When the temperatures approache to T_N the linewidths increase which indicate the critical evolution of spin-spin correlations and is consistent to the presence of long range order below T_N [71].

The temperature dependence of the ESR spectra at 280 GHz, i.e. below the AFMR gap, is shown in Fig. 4.7. Below the AFMR gap the ESR resonance spec-

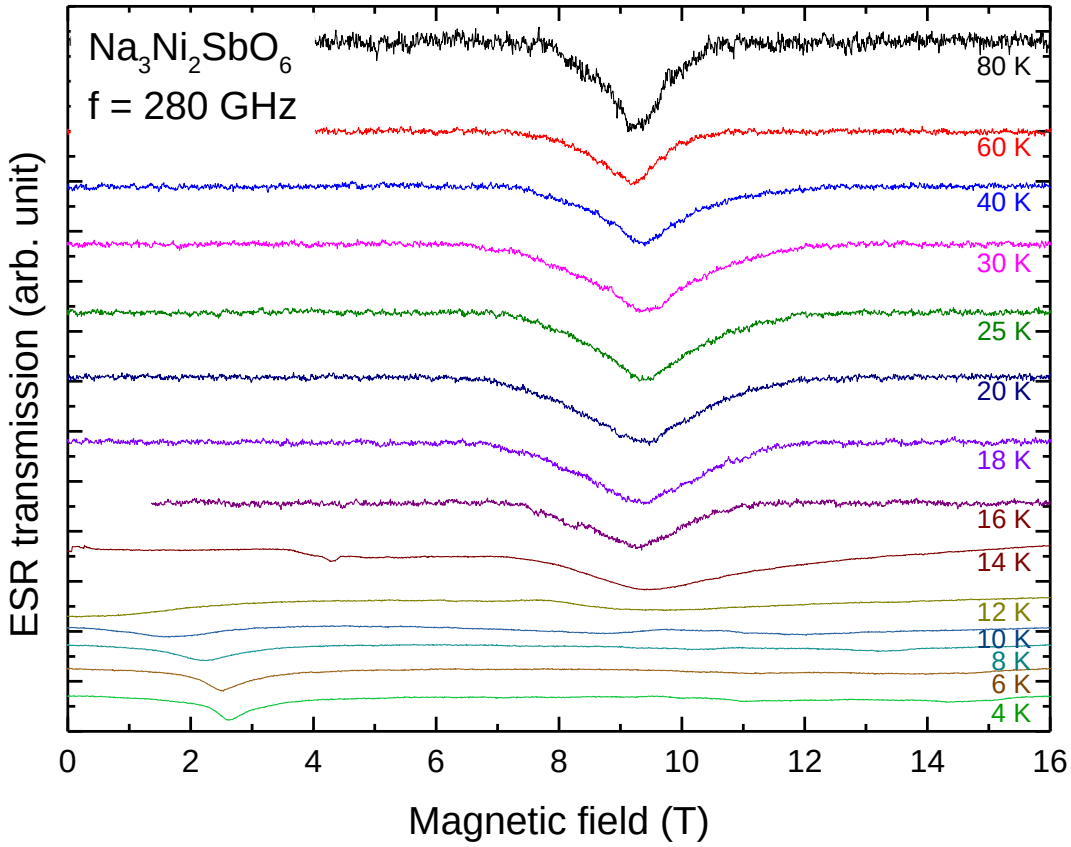

Figure 4.7: Temperature dependence of ESR spectra at 280 GHz. The broad resonance spectra at low temperatures have the three resonance signals. At T_N, the resonance fields shift to the higher fields and then merge to the one peak. The intensity of the ESR spectrum decreases at high temperature.

tra at low temperature are also very broad. The three resonance fields appear at 3 T, 11 T and 14 T, respectively, at 4 K. When the temperature increases, the resonance peaks shift to higher magnetic fields. In vinicity of the Neél temperature $T_N = 17$ K, the two resonance peaks disappear. And above the T_N only one resonance peak is observed.

Similar to the procedure at 388 GHz, the temperature dependent ESR spectra at 280 GHz are fitted by means of Lorentzian functions. Fig. 4.8 shows the temperature dependence of the resonance fields. The resonance signals move to

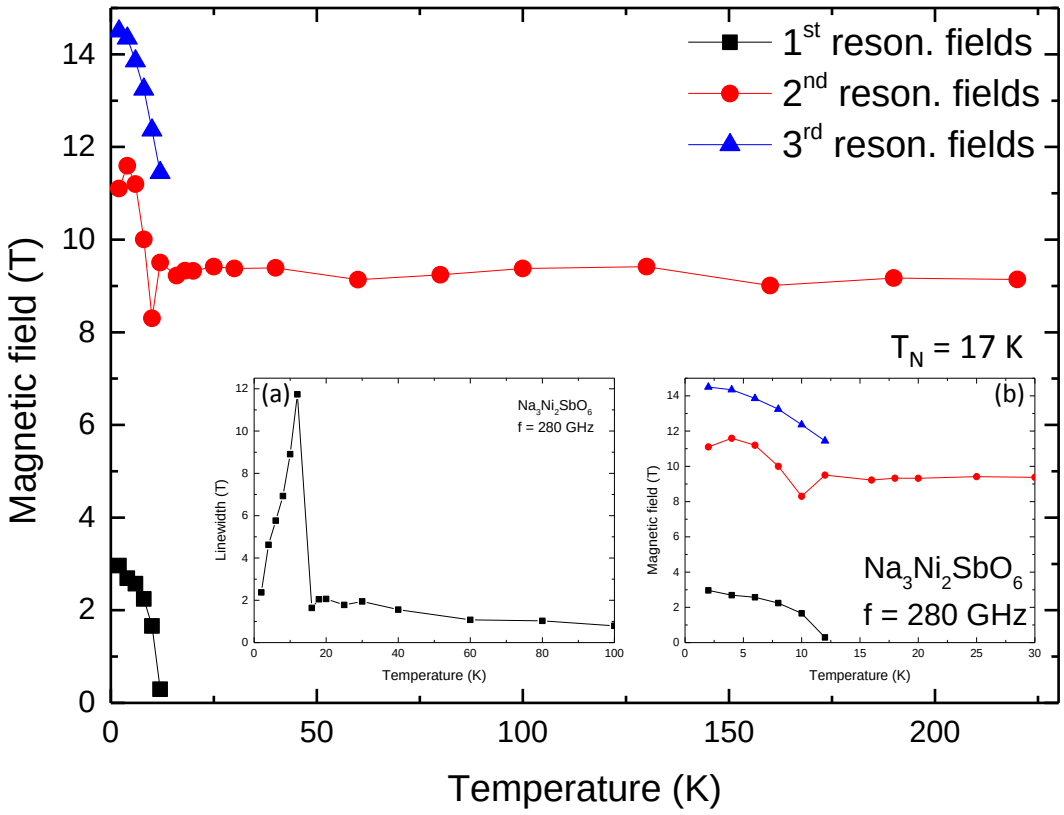

Figure 4.8: Temperature dependent resonance fields at 280 GHz below the AFMR gap. Insert: (a) The sum of the linewidths of resonance peaks of the ESR spectra. Around T_N an anomalous increase appears due to the developement a long range order. (b) The resonance fields shift to the lower magnetic field in vicinity of T_N and then are merged to one magnetic field.

lower magnetic field below T_N. Similar to the result at 388 GHz, the shift signals mean the evolution of the internal magnetic field in the long range ordered state [69]. But in this case the the resonance fields shift to the low field. Fig. 4.8 (a) shows the ESR linewidth versus the temperature. The increasing linewidth occurs at the Néel temperature which indicates a long-range order [71, 72].

$Li_3Ni_2SbO_6$ The HF-ESR measurement were performed on loose powder of $Li_3Ni_2SbO_6$ in the frequency range of 50 - 560 GHz at the temperature $T = 4$ K.

Fig. 4.9 shows the ESR signals at 4 K. At $f = 480$ GHz two AFMR lines are obtained around 15 T. At 300 GHz, there are two AFMR lines at 6 T and 10 T. At 150 GHz, one AFMR line at around 2.5 T is obtained. There are two AFMR lines at 70 GHz. One is at around 7 T, the other is a broad one at around 11.5 T.

Fig. 4.10 shows the magnetic field versus the frequency in units of T at $T = 4$ K. These resonance modes are analyzed by the mean field theory of an antiferromagnetic resonance with orthorhombic anisotropy [71]. In this case, two anisotropy

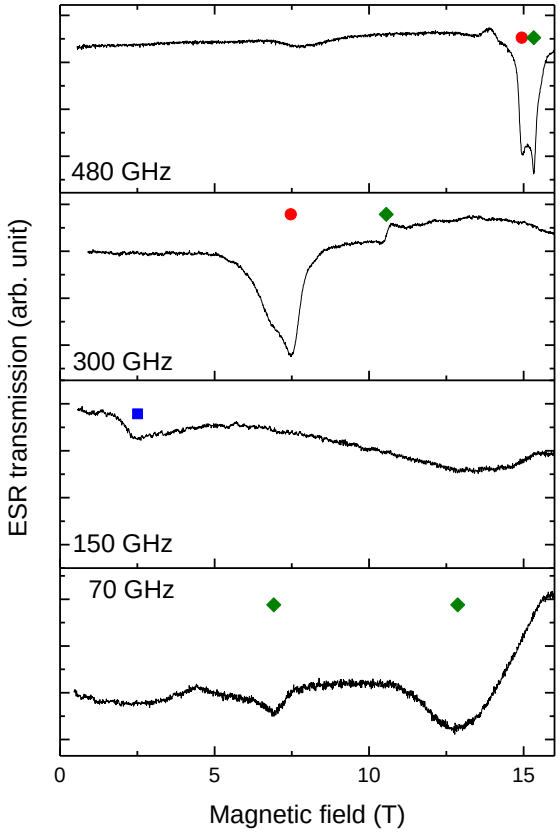

Figure 4.9: AFMR signals at 4 K in loose powder of $Li_3Ni_2SbO_6$. At 480 and 300 GHz two AFMR lines are obtained. At 150 GHz, there is only one AFMR line. At 70 GHz, there are two AFMR lines. Symbols are corresponding to the experimental data in Fig. 4.10

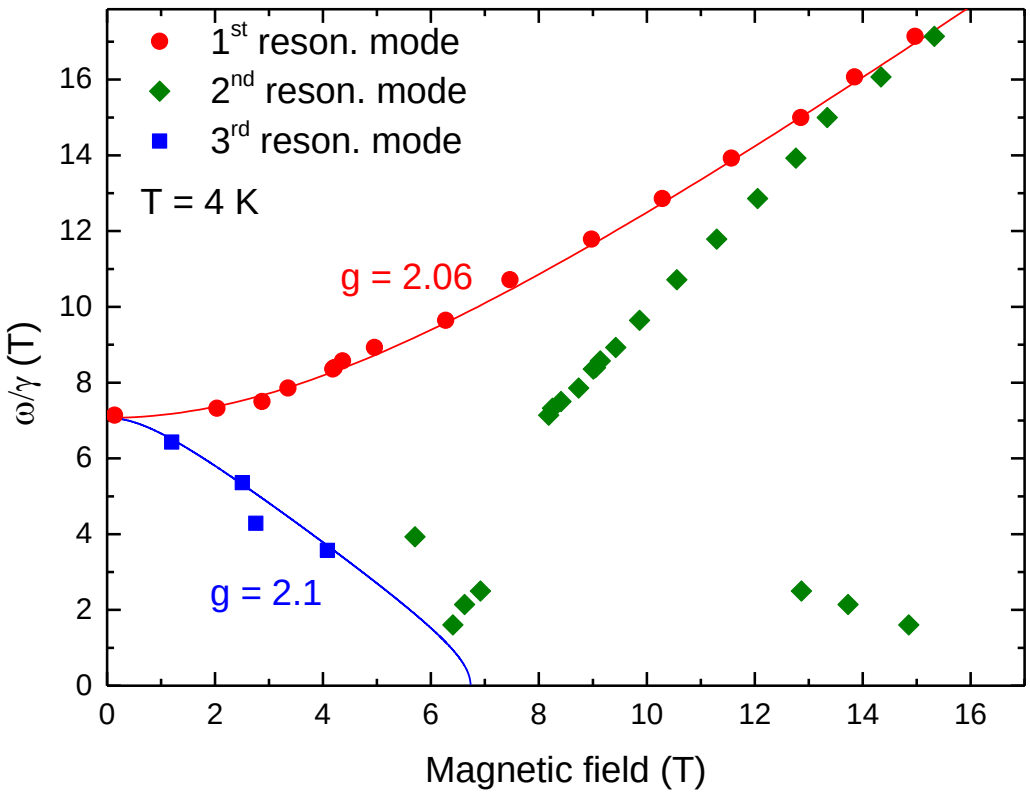

Figure 4.10: Experimental data ω/γ vs. magnetic field and in terms of the AFMR model simulation of magnetic field dependence of ESR data. When the easy axis is parallel to magnetic fields, the second resonance mode with a g-facotr of 2.1 is obtained below the AFMR gap of 7 T. When the easy axis is perpendicular to magnetic fields, the first resonance mode reveals the g-factor of 2.06.

fields exist in the sample. The first resonance mode means the behavior when the magnetic field is along to the second easy axis. The second resonance mode represents a situation when the magnetic field is applied along the easy axis.

When two anisotropy fields H_{A1} and H_{A2} are much smaller than the exchange field H_E, the AFMR frequencies can be described as follows,

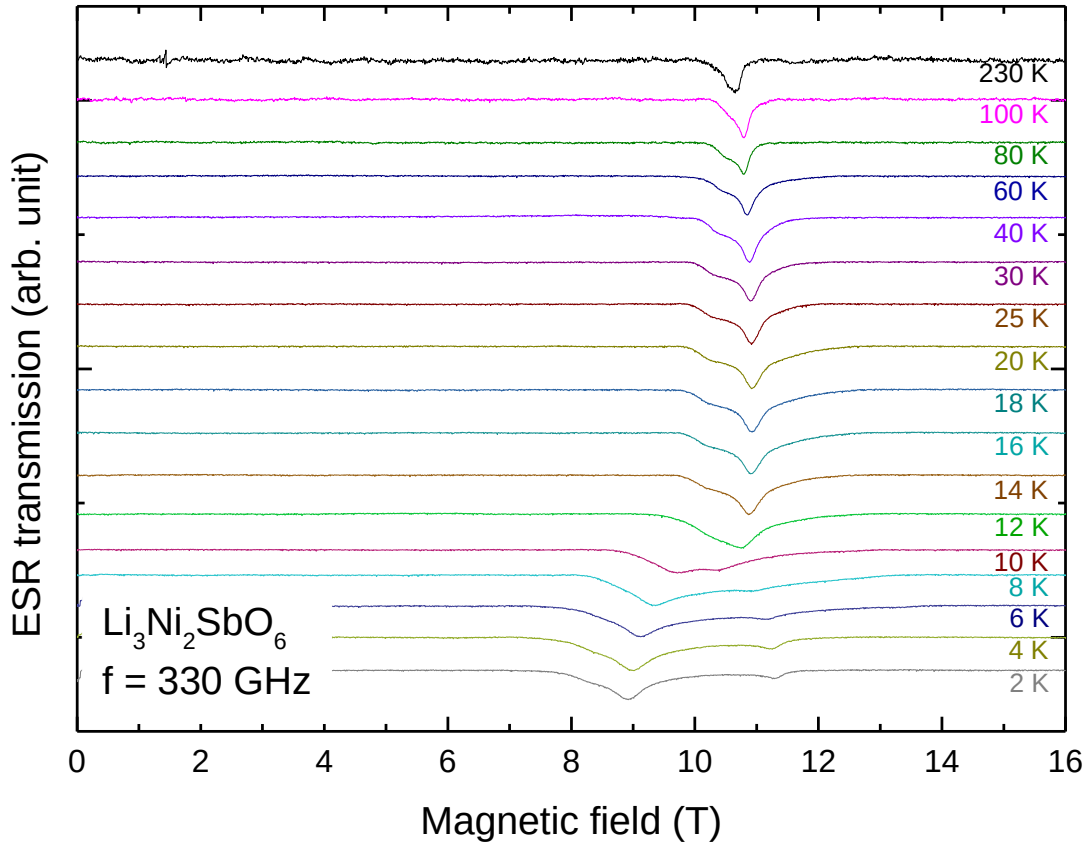

Figure 4.11: The temperature dependence of ESR spectra below the AFMR gap of 330 GHz. The broad resonance spectra at the low temperature is shrank when the temperatures increase.

$$\frac{\omega}{\gamma} = \frac{1}{\sqrt{2}}\sqrt{(1+\alpha^2)\,H_0^2 + C_1 + C_2 \pm \sqrt{(1-\alpha^2)^2\,H_0^4 + 2\,(1+\alpha)^2\,H_0^2\,(C_1+C_2) + (C_1-C_2)^2}}, \tag{4.4}$$

where $H_0 = gH/2$, $C_1 = 2\lambda K_1$, $C_2 = 2\lambda K_2$, and $\alpha = 1 - A\chi_{\parallel}$. The best simulation parameters are $C_1 = 88$ T, $C_2 = 50$ T, $\alpha = 1$ and $g = 2.1$. This simulation line is plotted as a blue line in Fig. 4.10. There is parameter $\alpha = 1$ which indicates a very small value of $\chi_{\parallel}$. Thus, $\chi \cong 0.06$ J T^{-2}/mole at 4 K [65] can be approximated as $\chi_{\perp}$. This yields the exchange constant λ is ~ 16.7 mole T^2/J. Also, the other parameters of the anisotropy constants can be calculated as $K_1 = 2.6$ J/mole, and $K_2 = 1.5$ J/mole.

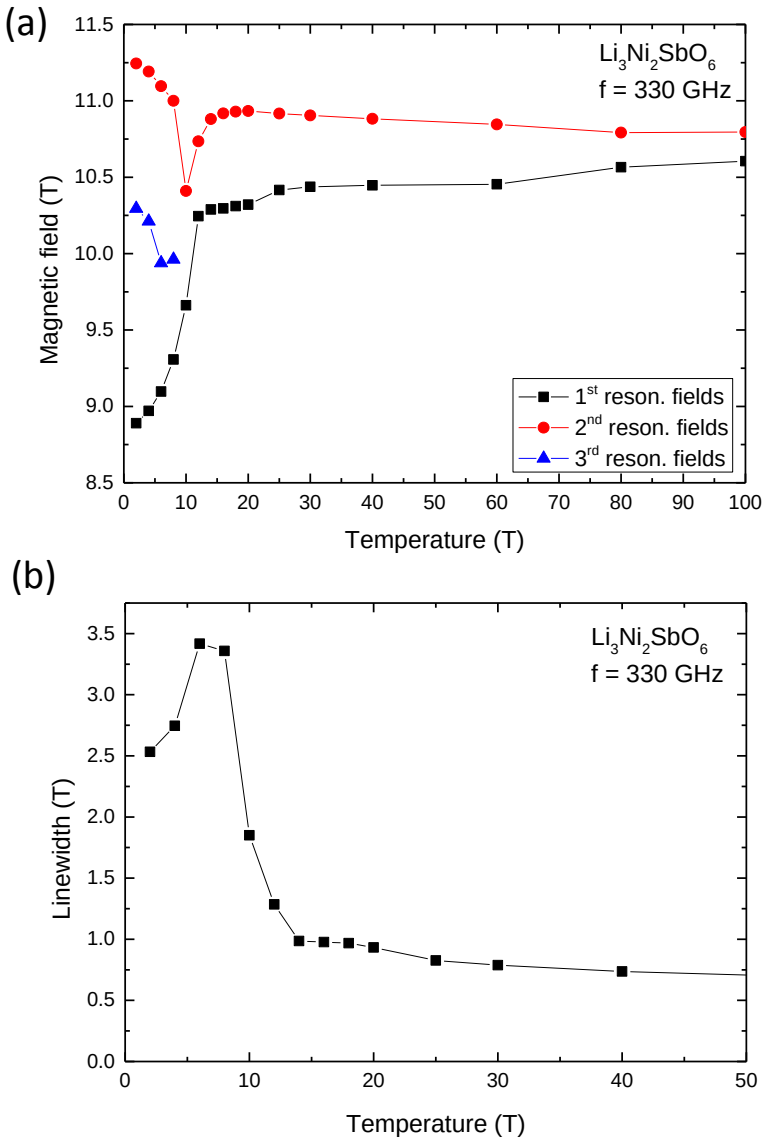

Figure 4.12: (a) Temperature dependent resonance field at 330 GHz above the AFMR gap. While the first and second resonance fields shift to the lower magnetic fields in vicinity of T_N, the third ones move higher fields. (b) The temperature dependent the sum of linewidths of the ESR resonance peaks. There is a shift at T_N due to the presence of long range order.

The second easy axis mode can be written as

$$\frac{\omega}{\gamma} = \sqrt{H_0^2 + C_1}. \tag{4.5}$$

With the obtained parameters, Equation (4.5) yiels the simulation line (red line) in Fig. 4.10 with the g-factor of 2.06. The AFMR gap is obtained as 7 T ($\sim$ 200 GHz). In this sample, the hard axis resonance mode is not observed. As well, there are many resonance fields (labelled by green dots) except the two main AFMR resonance modes. But those are not explained by the AFMR mode with orthorhombic anisotropy.

Temperature dependent ESR spectra at 330 GHz are shown in Fig. 4.11. At low temperature the resonance peaks appear at 9 T and 11.5 T. When the temperature increases, the width of ESR spectra decreases and the resonance field shifts to 11 T. Fig. 4.12 shows the temperature dependent resonance fields and linewidths. When $T < T_N$, the resonance fields are shifted due to the developing internal field, as in $Na_3Ni_2SbO_6$, as shown in Fig. 4.12 (a). The linewidths show an anomalous increase when the temperature approaches T_N which indicates a long range order occuring in the sample as shown in Fig. 4.12 (b).

4.3. Summary

HF-ESR studies are performed on $Na_3Ni_2SbO_6$ and $Li_3Ni_2SbO_6$. The frequency dependence of the ESR spectra of $Na_3Ni_2SbO_6$ shows four resonance modes which indicate a uniaxial antiferromagnetic resonance. When magnetic fields are applied along the easy axis, total three resonance modes are found which show a g-factor of 2.18 and an AFMR gap of 12.8 T ($\sim$ 358 GHz). But a spin-flop mode is not observable in this case. When the magnetic fields are applied perpendicular to the easy axis, a resonance mode is obtained which indicates a g-factor of 2.05. The temperature dependence of the ESR spectra is studied above and below the AFMR gap. The temperature dependence ESR data at 388 GHz and 280 GHz show a rapid shift around T_N which indicates the magnetic ordering at $T < T_N$. When the temperature increases, the resonance fields are shifted to higher magnetic fields or to lower magnetic fields at 388 GHz and 280 GHz, respectively. It is caused by the developed internal field. The experimental resonance modes are simulated with modified AFMR equations because the anisotropy field is not small enough to be neglected. The simulation lines reproduce the experimental ones quit well. But the simulation of the AFMR mode where the easy axis is perpendicular to the magnetic field cannot be well reproduced. The resulting

parameters are the anisotropy field of 2.55 T and the exchange field of 32 T.

$Li_3Ni_2SbO_6$ is measured as well by the ESR technique. The mean field theory of antiferromagnetic resonance with orthorhombic anisotropy is applied here to analyze the result. The frequency dependence of the ESR spectra shows two AFMR modes. One is the easy axis mode and the other is the second easy axis mode. From the easy axis mode, a g-factor of 2.1 is deduced, and a g-factor of 2.06 on the second easy axis mode. The exchange constant λ and the antiferromagnetic constants K_1 and K_2 are revealed as 16.7 mole T^2/J, 2.6 J/mole and 1.5 J/mole, respectively. The AFMR gap is 7 T ($\sim$ 200 GHz) at zero magnetic field. Temperature dependent ESR spectra are studied at 330 GHz which is above the AFMR gap. It shows the rapid shift around T_N. When the temperature increases, the resonance fields are shifted to higher magnetic fields which indicates the occurrence of internal antiferromagnetic fields in vicinity of T_N.

The mean field theory considers an averaged effect of many-body system. It cannot explain the details of the behavior of the sample. To achieve more successful simulations, second-nearest-neighbor exchange interactions or more interactions between spins should be considered. In the experimental point of view, the short range antiferromagnetic fluctuation shows up in the temperature dependencies of the resonance field and the linewidth.

5. Spin-1 Kagomé Antiferromagnet $Ca_{10}Cr_7O_{28}$

5.1. Kagomé Lattice

The antiferromagnetic Kagomé spin lattice is a good model to study spin frustration [73–75]. The first study was done by Ichiro Shoji in 1951 [76]. This structure named from the Japanese basket because the lattice pattern looks like a bamboo basket 'kagomé'. Fig. 5.1 (a) shows the kagomé lattice which has the pattern of two triangles and two honeycombs each sharing a vertex. Due to the corner sharing triangles, the spin frustration occurs when the kagomé lattice has antiferromagnetic coupling [77,78]. For example, Fig. 5.1 (b) shows that the spins in a honeycomb lattice align antiparallel and then the remaining spin in a triangle lattice frustrates. The spins on the three corners of the honeycomb lattice frustrate as sketched in Fig. 5.1 (c). The Heisenberg model for the kagomé lattice is

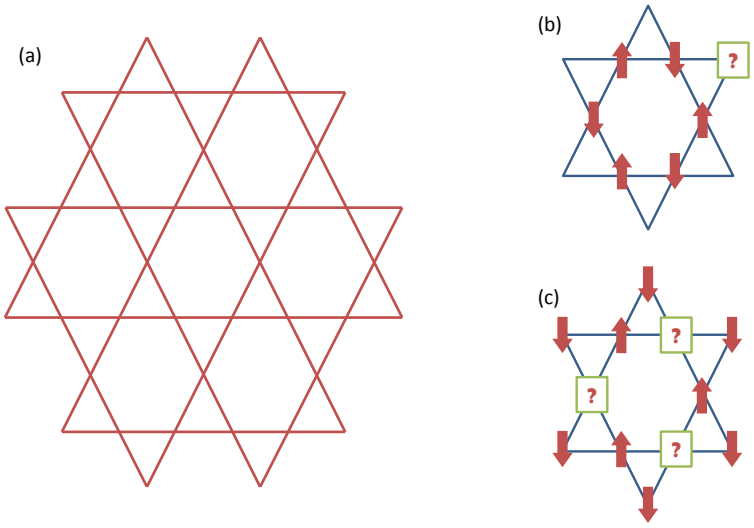

Figure 5.1: (a) Schema of a kagomé structure lattice. The triangles and honeycombs each a vertex share. (b) When all the spins on the honeycomb couple antiferrmagnetically, the spin frustrates in the triangle lattice. (c) Alternatively, the spins on the honeycomb lattice are frustrated.

$$H = J \sum_{\langle i,j \rangle} \vec{S}_i \cdot \vec{S}_j, \tag{5.1}$$

where J is the exchange constant, the sum of spin $\vec{S}_i$ and $\vec{S}_j$ runs over all the nearest neighbors [80]. Kagomé lattice systems are mainly studied by means of the magnetic susceptibility, the specific heat, neutron scattering, μSR and NMR.

Also, by means of the HF-ESR, the spin dynamics of a system can be studied. ESR measurments on the kagomé spin lattice have been used to study the temperature dependence of the g-factor and of the linewidths in the vicinity of the Néel temperature [81]. The observed properties are different. $SrCr_8Ga_4O_{19}$ with a total spin $S = 3/2$ and $Cu_3V_2O_7(OH)_2 \cdot 2H_2O$ with a total spin $S = 1/2$ show shifts of the g-factor at low temperature [82, 83]. In contrast, $ZuCu_3(OH)_6Cl_2$ with a total spin $S = 1/2$ has a g-factor which is temperature independent [84].

5.2. Crystal Structure

$Ca_{10}Cr_7O_{28}$ is provided by the group of Prof. B. Lake at TU Berlin [79]. Cr^{5+} ions ($3d^1$, $S = 1/2$) form the kagomé bilayers as shown in Fig. 5.2. Couplings between nearest neighbor Cr^{5+} ions along J_0 (green lines), along J_1 (orange lines), and along J_2 (red lines) are presented. The slightly tilted different bilayers show ferromagnetic interaction J_0 [79]. This yields an effective spin of $S = 1$. Cr^{5+} ions in the kagomé plane couple antiferromagnetically to each other [79]. In the center of the hexagon, there is a Cr^{6+} ion. The antiferromagnetic exchange interactions in the kagomé plane are J_1 and J_2. The bonding distance along J_0 is 3.9 Å, along J_1 is 5.09 and 5.04 Å in upper and lower layer, respectively [79]. Also, the bonding distance along J_2 is 5.70 and 5.75 Å in upper and lower layer, respectively [79].

5.3. HF-ESR and X-band ESR: Experimental Results and Discussion

HF-ESR: The crystal $Ca_{10}Cr_7O_{28}$ was measured along two different axes, the b-axis and the c-axis in magnetic fields up to 16 T. The frequency range was $\nu = 60 - 390$ GHz at the temperature T = 4 K. The kagomé plane is located in the crystallographic ab-plane as shown in Fig. 5.2 (a). The crystallographic c-axis is perpendicular to the kagomé plane.

Fig 5.3 shows the plot of the frequency versus the resonance field applied along the c-axis with several ESR spectra at 4 K. A single resonance peak is obtained up to 220 GHz. Above it, there are two resonance peaks. In contrast, at 300 GHz, there are five resonance features. Such behavior is not expected for the magnetic Cr^{5+} ion ($S = 1/2$). Hence, it is attributed the multiple scattering. When the sample size is compatible to the wavelength of the applied microwave, the microwave does not propagate along the direction of transmission. Then, the incident wave and reflected wave can make nodes where those waves are canceled.

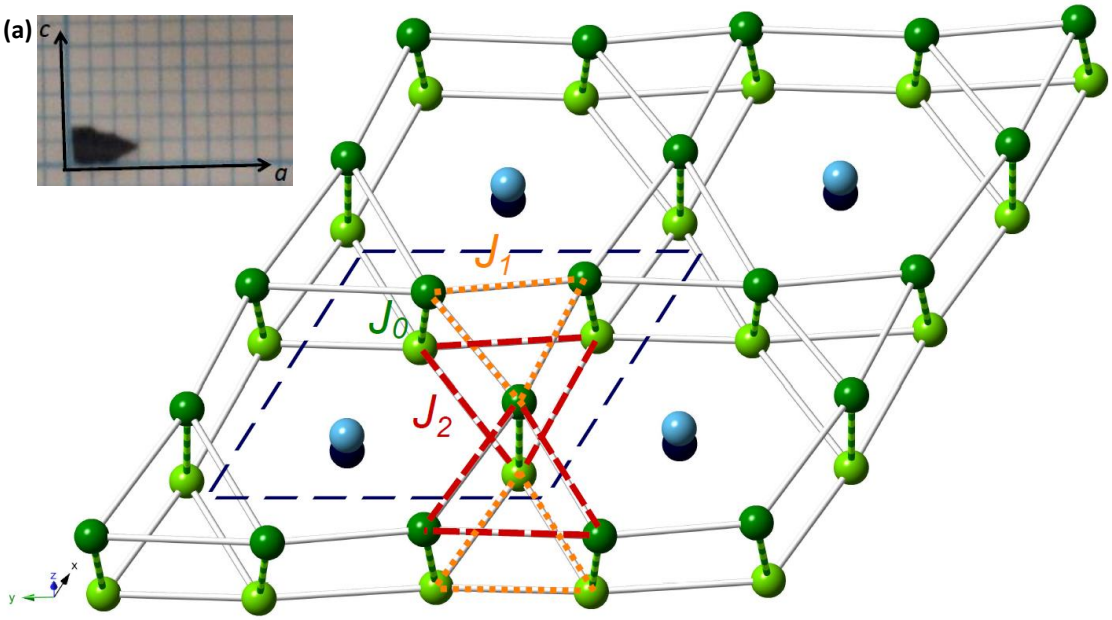

Figure 5.2: Structure of the bilayered $Ca_{10}Cr_7O_{28}$ [79]. J_0 is a ferromagnetic coupling. The green, light green, dark and light blue balls mean Cr^{5+} ion in one layer, Cr^{5+} ion in the other layer, and non-magnetic Cr^{6+} ions in both layers, respectively [79]. The bonding distance along J_0 is 3.9 Å, along J_1 (orange lines) is 5.09 and 5.04 Å in upper and lower layer, respectively [79]. Also, the bonding distance along J_2 (red lines) 5.7 Å ia 5.70 and 5.75 Å in upper and lower layer, respectively [79]. (a) Photographic picture of $Ca_{10}Cr_7O_{28}$. In crystallographic ab-plane, the kagomé lattices are presented. The crystallographic c-axis is perpendicular to the kagomé lattice.

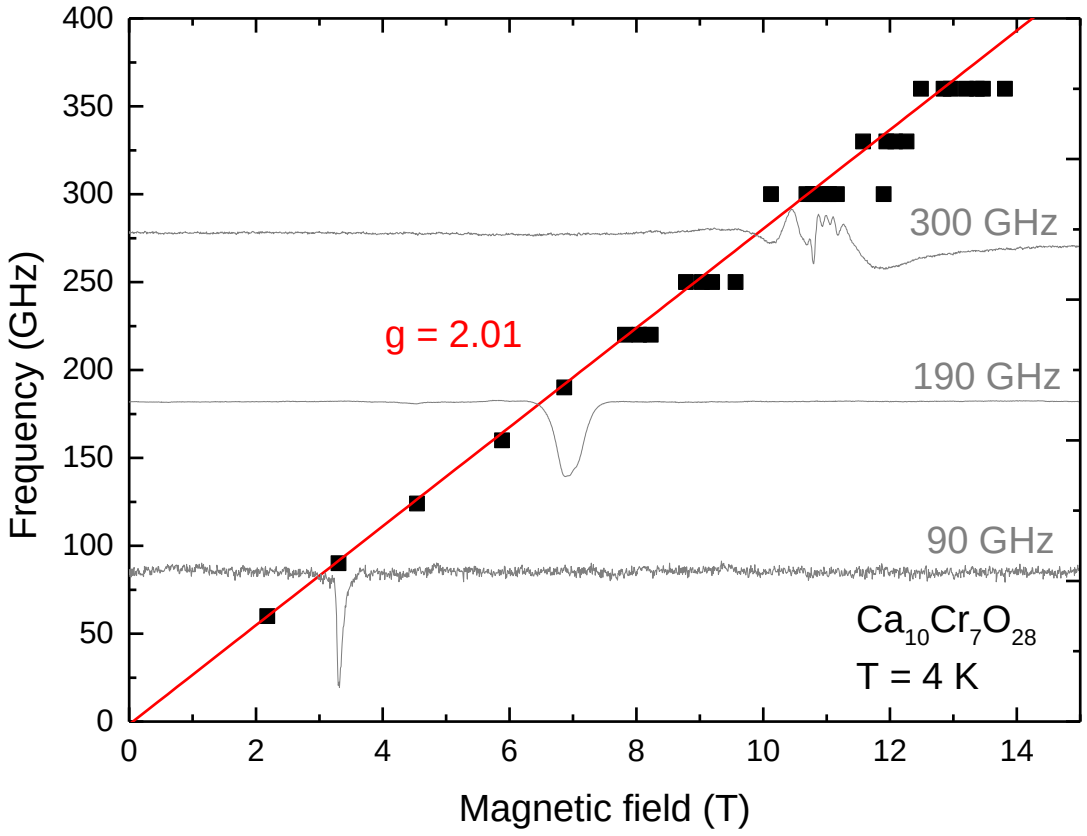

Figure 5.3: Plot of frequency versus resonance fields of the ESR resonance line with representative ESR spectra of the $Ca_{10}Cr_7O_{28}$ at 4 K. Magnetic field have been applied along the crystallographic c-axis. Above 220 GHz, multiple features are obtained presumingly due to the standing wave.

Those nodes do not change their positions which lead to a standing wave inside the sample. Multiple reflections can show up in ESR spectra as multiple features. For an exact analysis, the related spectra are ignored. Hence, the ESR spectra from 60 GHz to 190 GHz are analyzed. The analysis reveals the g-factor of 2.01 which is plotted by the red line, and the extrapolation of the red line to $H = 0$ implies that there is no ZFS.

The plot of frequency versus magnetic fields of ESR resonance line with ESR spectra of the c-axis at 200 K and at ν = 160 - 330 GHz is shown in Fig. 5.4. At

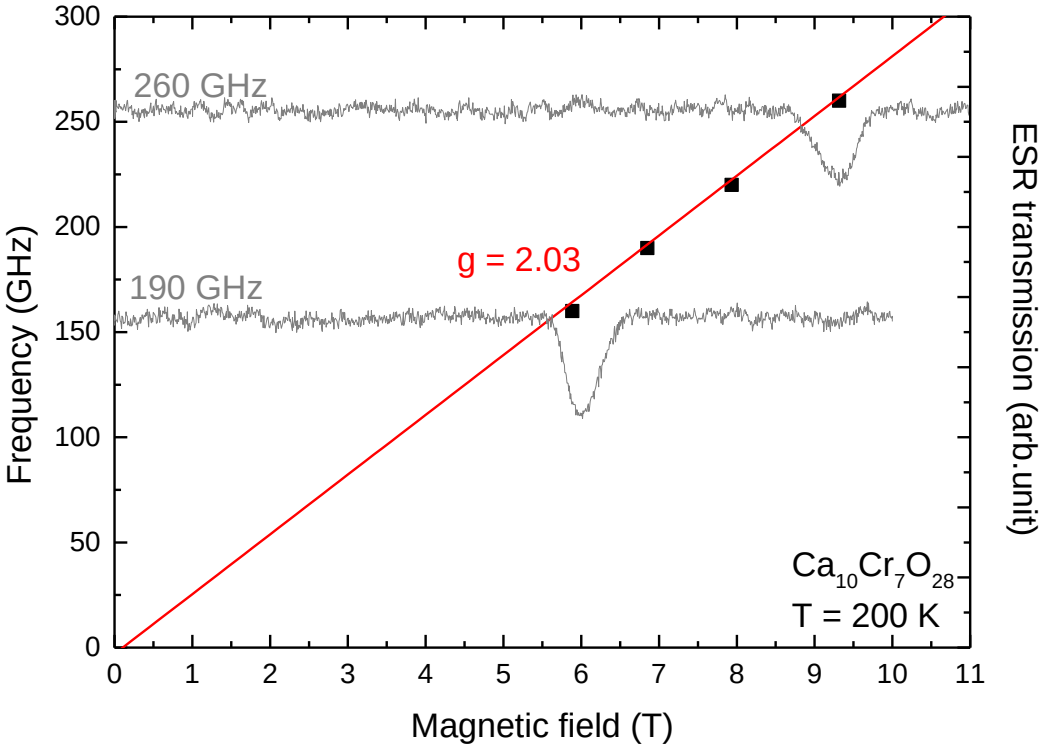

Figure 5.4: Plot of frequency versus resonance field of the ESR resonance line with representative ESR spectra on the crystallographic c-axis of $Ca_{10}Cr_7O_{28}$ at 200 K. The g-factor is 2.03 with no ZFS.

high enough temperature, multiple features are not observed. An analysis of the four resonance spectra reveals a g-factor of 2.03 and no ZFS. The material does not have the property of a magnetic anisotropy along the c-axis.

Along the crystallographic b-axis, the ESR measurements are performed in magnetic field up to 16 T at frequencies $\nu = 35 - 390$ GHz at the temperature $T = 4$ K. Fig. 5.5 shows the plot of frequency versus magnetic fields with representative ESR spectra. A single resonance peak is obtained up to 150 GHz. Similar to what is observed for the c-axis, multiple features show up due to standing waves inside the sample. Hence, the ESR spectra from 35 - 150 GHz are considered for analysis only. This reveals a g-factor of 1.94 which is smaller than the g-factor of 2.01 of the c-axis at 4 K. The frequency dependence of the ESR spectra at 30 K

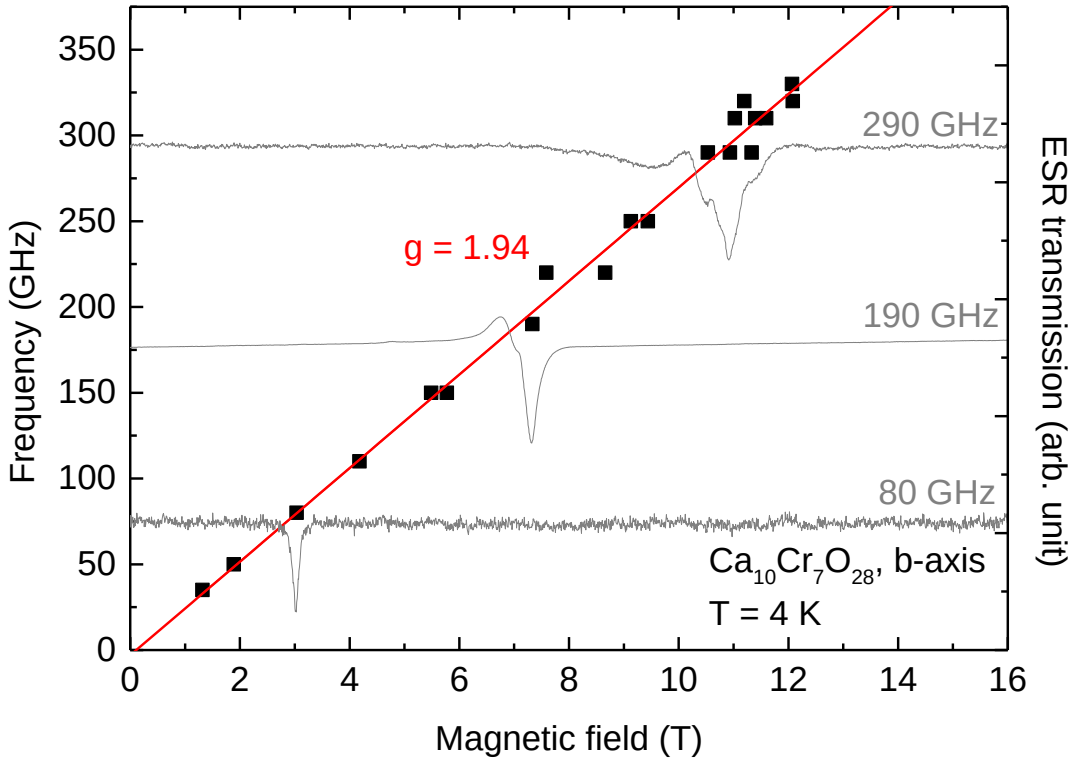

Figure 5.5: Plot of frequency versus resonance magnetic field dependence of the ESR resonance line with representative ESR spectra on the b-axis of the $Ca_{10}Cr_7O_{28}$ at 4 K. The g-factor is 1.94 and the no ZFS. The multiple features are obtained above 150 GHz.

is shown in Fig. 5.6. From the analysis it reveals a g-factor of 1.93 and no ZFS. Comparing those results, it shows that g-factors are different depending on the axes.

X-band ESR: The X-band (9.58 GHz) ESR measurements have been performed in the temperature range from 4 K to 230 K with a commercial EMX spectrometer from Bruker at IFW Dresden. By HF-ESR, the multiple peaks are obtained and the intensity of the spectra is quite small. In contrast, X-band ESR provides a clear signal with a cavity resonator.

The temperature dependence of X-band ESR spectra along the c-axis at fre-

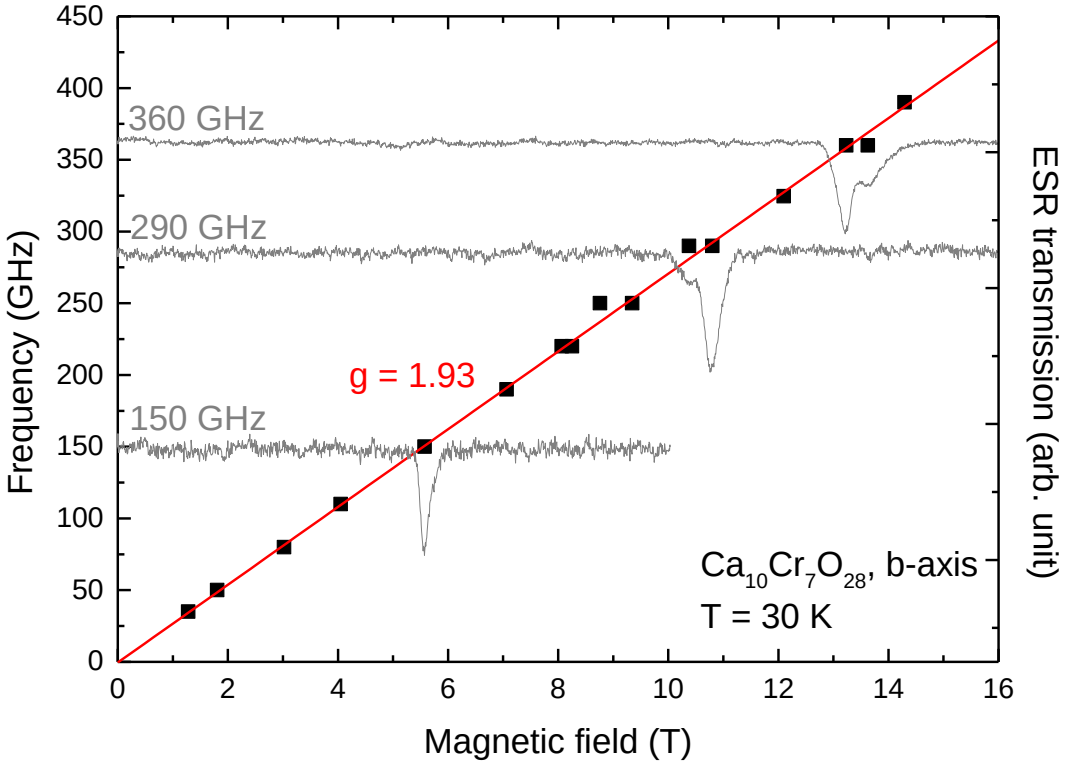

Figure 5.6: Frequency versus resonance magnetic field dependence of the ESR resonance line with representative ESR spectra along the b-axis of $Ca_{10}Cr_7O_{28}$ at 30 K. The g-factor is 1.93 and there is no ZFS.

quencies range $T = 4.07 - 230$ K is plotted in Fig. 5.7. The resonances occur at 0.36 T as well as the intensity of the spectrum is very high at 4.07 K. The spectra of the X-band ESR are analyzed with fitting the derivate Lorentzian function,

$$y = y_0 - 16\frac{A}{\pi}\left(\frac{1}{\omega}\right)\left(\frac{x - x_c}{\omega}\right)\left[4\left(\frac{x - x_c}{\omega}\right)^2 + 1\right]^2, \tag{5.2}$$

where y_0 is the background, x_c is the center field which means the magnetic resonance field, ω is the linewidth of the spectrum, and A is the area of the spectrum.
The fitting result of all spectra along the c-axis is in Fig. 5.7 (a) and (b) showing the peak area and the linewidth, respectively. Fig. 5.7 (a) shows the decreasing

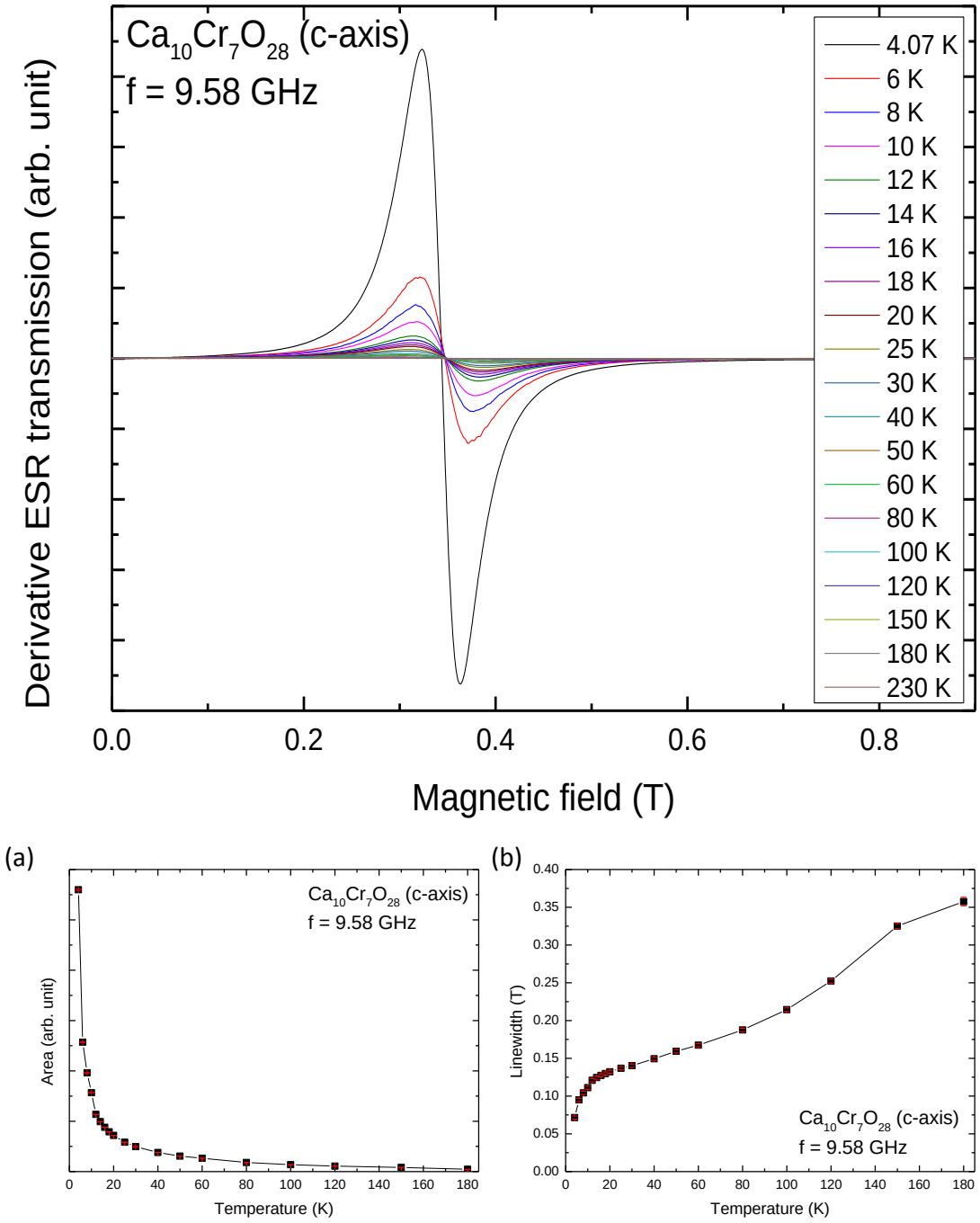

Figure 5.7: The X-band ESR spectrum of $Ca_{10}Cr_7O_{28}$ along the c-axis. (a) Resonance peaks area as derived by analyzing the spectra by means of a derivative Lorentzian. (b) Temperature dependence of the linewidth along the c-axis. The linewidth decreases upon decreasing the temperature.

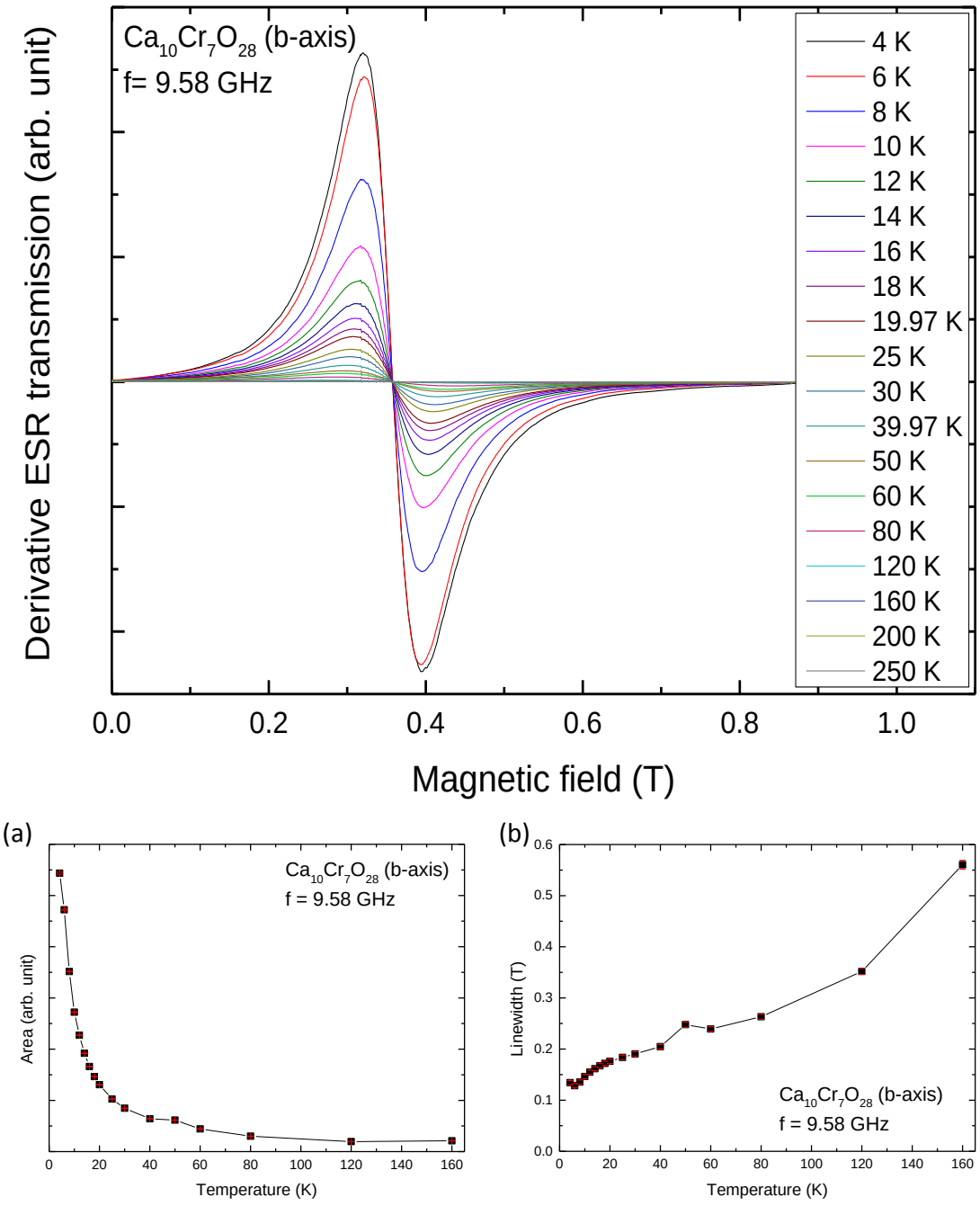

Figure 5.8: The X-band ESR spectrum of $Ca_{10}Cr_7O_{28}$ along the b-axis. (a) Resonance peak area as derived by analyzing the spectra by means of a derivative Lorentzian (b) Temperature dependence of the linewidth along the b-axis. The linewidth decreases upon decreasing the temperature.

area of the ESR spectrum as the temperature increases which means a decreasing absorbed power by the resonating spin system. The linewidth decreases when the temperature decreases as shown in Fig. 5.7 (b). Below 10 K, the linewidth increases rapidly and drops around 2 K. The temperature dependence X-band ESR data along the b-axis is plotted in Fig. 5.8. As well, the spectra are fitted with the derivative Lorentzian function, Equation (5.2). The area is shown in Fig. 5.8 (a). The area decreases when the temperature increases. Fig. 5.8 (b) shows the decreasing linewidths by decreasing temperatures. The behavior of the both the b-axis and the c-axis does not show clear differences.

5.4. Summary

HF-ESR studies have been performed along the crystallographic b and the c axis of the bilayer kagomé lattice system $Ca_{10}Cr_7O_{28}$. The b-axis is parallel, c-axis is perpendicular to the kagomé planes.
The frequency dependencies of the ESR spectra along the c-axis at 4 K and 200 K show one resonance line at low fields but multiple ones at higher fields. This is attributed to the presence of standing waves in the sample. The analysis hence disregards the multiple peaks. The analysis reveals the g-factor of 2.01 and 2.03 at 4 K and 200 K, respectively. Also, there is no magnetic anisotropy in the spin system of the material.
The temperature dependence of X-band ESR spectra is measured. By using the derivative Lorentzian function, the area and the linewidth of the spectra are derived from the data.
For the b-axis, the frequency dependences of the ESR spectra at 4 K and 30 K show a change in the g-factor from 1.94 at 4 K to 1.93 at 300 K. ZFS is not found. From the analysis of the temperature dependent ESR spectra at X-band the area and the linewidth of the spectra are obtained. Both the area and the linewidth for the b- and the c-axis show the same tendency depending on the temperature. The linewidth decreases when the temperature decreases. When the temperature decreases, the area increases which indicates a higher spin susceptibility at lower temperatures.

Part IV.
Metal-Organic Compounds

6. Introduction to Single Molecule Magnetism

Single molecule magnets (SMMs) are good model systems to study magnets comprising a finite numbers of interacting paramagnetic centers. SMMs are isolated spin systems and nanoscale magnets. Main characteristics of SMMs are following as: the large spin number, the anisotropy and the negligible interaction between the molecules. They offer a chance to study a quantum phenomenon of so-called quantum tunneling of the magnetization which will be described below.

SMMs are constituted by a magnetic core and non-magnetic ligands. They possess a finite number of paramagnetic ions in the magnetic core. Those ions can form a large spin due to exchange interactions between magnetic ions. Representative magnetic ions are transition metal ions such as Mn, Fe, Ni, and Co. There are several interesting SMMs, for example, Mn12 and Fe8 [85]. They have twelve Mn ions and eight Fe ions in a core, respectively. The magnetic core is

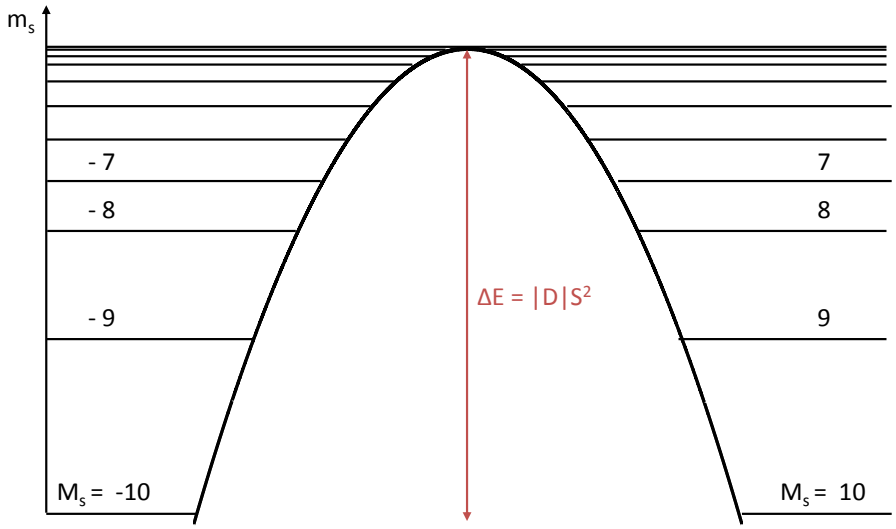

Figure 6.1: Schematic diagram with the spin states $S = \pm 10$ with an anisotropy energy barrier $\mid D \mid S^2$.

surrounded by the non-magnetic ligands. The intermolecular interaction is very small compared to the intramolecular interaction. Hence, the interaction between SMMs can be often neglected. Each molecule can be considered as an independent magnetic unit.

The other characteristic of SMMs is a magnetic anisotropy which is caused by the spin-orbit coupling. Anisotropy with a large spin number induces an energy barrier between the degenerated spin states in SMMs. Basically, the energy potential takes the form of the double wells because of the energy barrier as shown in Fig. 6.1. In this case, the spin state $\pm S$ lie lowest. With a given anisotropy parameter D, the larger spin number the bigger energy barrier as follows, $\Delta E =\mid D \mid S_z^2$. A spin has to overcome the energy barrier to reverse the magnetization.

Due to the large anisotropy barrier, the SMMs have a long relaxation time which leads to a hysteresis in magnetization [86]. This relaxation is affected by the temperature. When the relaxation time becomes longer compared to the measurement time below a certain temperature, the magnetization will not flip during the measurement. Thus, the spin states of SMMs depend not only on the external magnetic field but also on the measurement time. The related temperature is

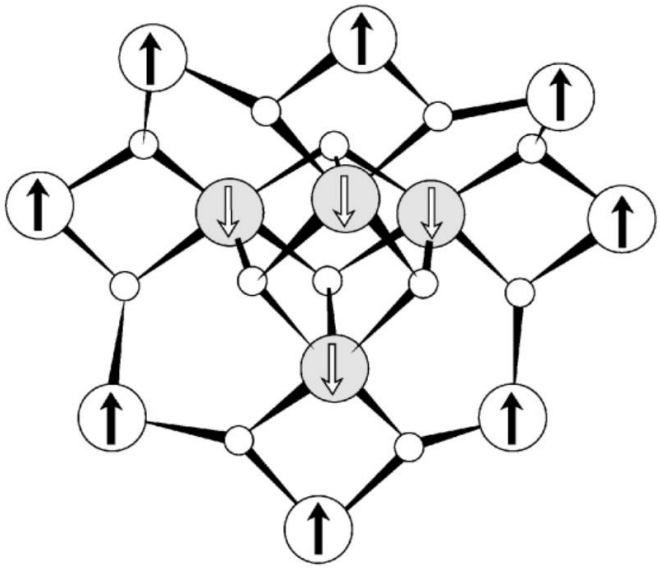

Figure 6.2: Image of the core of the Mn_{12}-acetate. Total twelve Mn ions are ferromagnetically or antiferromagnetically coupled to lead to the large spin number $S = 10$ [89].

called the blocking temperature [87, 88]. Therefore, measurements on SMMs are often performed at very low temperatures. In order to realize experimental situation where thermally activated, changes of the spin states are strongly suppressed.

The most prominent quantum phenomenon in SMMs is quantum tunneling of magnetization. In the case of Fig. 6.1, a transition between the spin states cannot be possible because the states are orthogonal. However, if there is a perturbation in xy-plane, it makes off-diagonal terms in a matrix which leads to a mixing of states. The perturbation can occur by x, y component of an applied magnetic field or a transverse anisotropy. Then, spins can transit from spin states $\mid m >$ in one side of the double potential well to spin states $\mid m' >$ in another side [90,91]. This phenomenon is observed in the magnetization data. SMMs show a hysteresis loop in the magnetization due to their energy barrier. Then due to the transverse anisotropy, there are multiple steps at points of energy mixing [92].

One of the well-known SMMs is Mn_{12}-acetate, which was synthesized firstly in 1980 [93]. Its unique magnetic properties were discovered in 1993 [94]; a large spin number, a large anisotropy. The structure of $[Mn_{12}O_{12}(CH_3\ COO)_{16}(H_2O)_4] \cdot 2CH_3COOH \cdot 4H_2O$ which is referred to as Mn_{12}-acetate is shown in Fig. 6.2 [95]. All Mn ions are connected via oxygen ions. The four inner Mn^{4+} ions are ferromagnetically coupled and the eight outer Mn^{3+} ions are also ferromagnetically coupled as well. And the four inner Mn^{4+} ($S = 3/2$) ions are antiferromagnetically coupled with eight outer Mn^{3+} ($S = 2$) ions. Hence, the ground state can be described by a total spin $S_{\mathrm{tot}} = 10$. Mn_{12}-acetate has a strong negative uniaxial anisotropy ($D \sim 60$ K) [96]. Mn_{12}-acetate shows the distinct properties of SMMs such as the slow relaxation time, the quantum tunneling, and the magnetic hysteresis curve of the magnetization [11, 97].

In the applicative point of view, SMMs may be in principle used for magnetic devices such as quantum computing, high-density storage [98]. SMMs are very small magnets in the unit of molecules. These molecules have large spins which can play a role as digits. Thus, it can be applied to high-density storage like as a hard disk [99]. On the other side, SMMs can be used to build up the quantum computer. Superposition of large spin states can make possibly quantum bits [100].

In this chapter, various characteristics of various metal-organic compounds are studied by ESR spectroscopy. Through ESR measurement, the total spin number and the magnitude of the magnetic anisotropy are determined.

7. Ni Dimer Complexes with Au Ligand

SMMs behave like small magnets. They are discussed as possible ingredients of future information storage devices. Hence, there is a requirement to deposit the SMMs on planar surfaces in order to be able to use them in applications such as high density information storage or quantum computing [101, 102]. However, SMMs can lose easily their unique magnetic properties and their structures on the surface [103].

Prior to the deposition on the surface, the behavior of Ni based SMMs with one Au atom was studied. This is a first step to understand the influence of ligand structure and metallic atoms on the magnetic properties of Ni^{2+} dimer complexes. The results described in the follows has been published in [104].

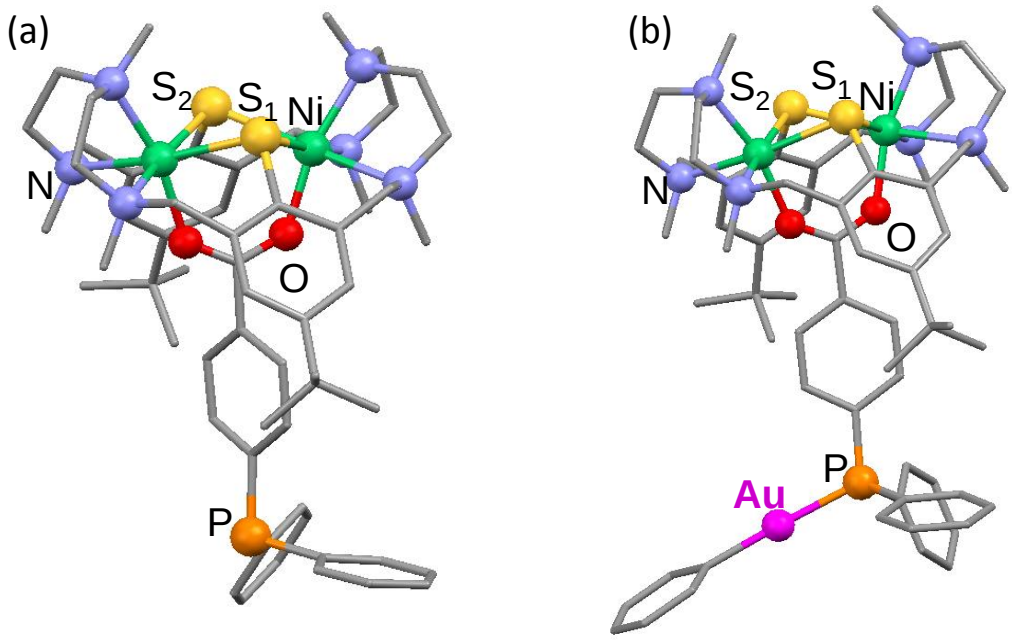

Figure 7.1: Structures of two Ni^{2+} dimer complexes. (a) $[Ni_2L(dppba)]ClO_4$ without Au atom and (b) $[Ni_2L(dppba)AuPh]BPh_4$ with Au atom. The two Ni^{2+} in the two complexes are connected by dppda ligand. The average angle of Ni-S-Ni of both complexes is around 90°. The green, yellow, red, orange, pink balls means nickel, sulfur, oxygen, phosphorus, gold atoms, respectively [104].

7.1. Crystal Structure

Two Ni^{2+} dimer complexes have been synthesized in the group of Prof. Kersting at TU Leipzig. The details of the synthesis and chemical characterization of them are described in [104]. The structures of the two complexes ($[Ni_2L(dppba)]ClO_4$) '$2ClO_4$' and ($[Ni_2L(dppba)AuPh]BPh_4$) '$4BPh_4$' are shown in Fig. 7.1. Both complexes are the carboxylato-bridged ones which can be isolated as an air-stable materials [104, 105].

For $2ClO_4$, the two Ni^{2+} ions are connected by two sulfur (S) bridges and an acetate bridge with the distance of 3.481(2) Å [104]. The angles of Ni-S_1-Ni and Ni-S_2-Ni are 89.47(5)° and 90.08(5)°, respectively [104]. The average distances of Ni-S, Ni-O, and Ni-N are 2.466(14)Å, 2.012(3)Å, and 2.229(4)Å, respectively [104].

For $4BPh_4$, the two Ni^{2+} are also connected by two sulfur (S) bridges and an acetate bridge. The angle of Ni-S_1-Ni and Ni-S_2-Ni are 89.54(5)° and 88.16(4)°, respectively [104]. The average distances of Ni-S, Ni-O and Ni-N are 2.472(1)Å, 2.0115(3)Å, and 2.229(4)Å, respectively [104]. An Au atom is attached to the phosphorus (P) atom of the head part and that forms an almost perfectly linear angle between C-Au-P of 177.8(2)° [104]. The distances of Au-C and Au-P are 2.048(7)Å and 2.3013(12)Å, respectively [104]. The binding of the Au atom to the P does not have a significant effect on the main structure of Ni^{2+} with dppda ligand.

7.2. Magnetization and HF-ESR: Experimental Results

Static magnetization measurements Static magnetization measurements on $2ClO_4$ and $4BPh_4$ were performed by Y. Krupskaya at IFW Dresden by means of a commercial SQUID (superconducting quantum interference device) magnetometer from Quantum Design in the temperature range from 2 to 300 K in magnetic fields from 0 to 5 T.

The field dependence of the magnetization of $2ClO_4$ and $4BPh_4$ measured at T = 1.8 K is shown in Fig. 7.2. The two complexes show similar magnetization curves. The magnetization is saturated at 5 T. For both compounds, a saturation magnetization is around 4.2 μ_B/f.u. which corresponds to the theoretical expectation of $S_{\mathrm{tot}} = 2$. It indicates a ferromagnetic coupling between the Ni^{2+} ions ($3d^8$, $S_{\mathrm{Ni}} = 1$) in the molecule.

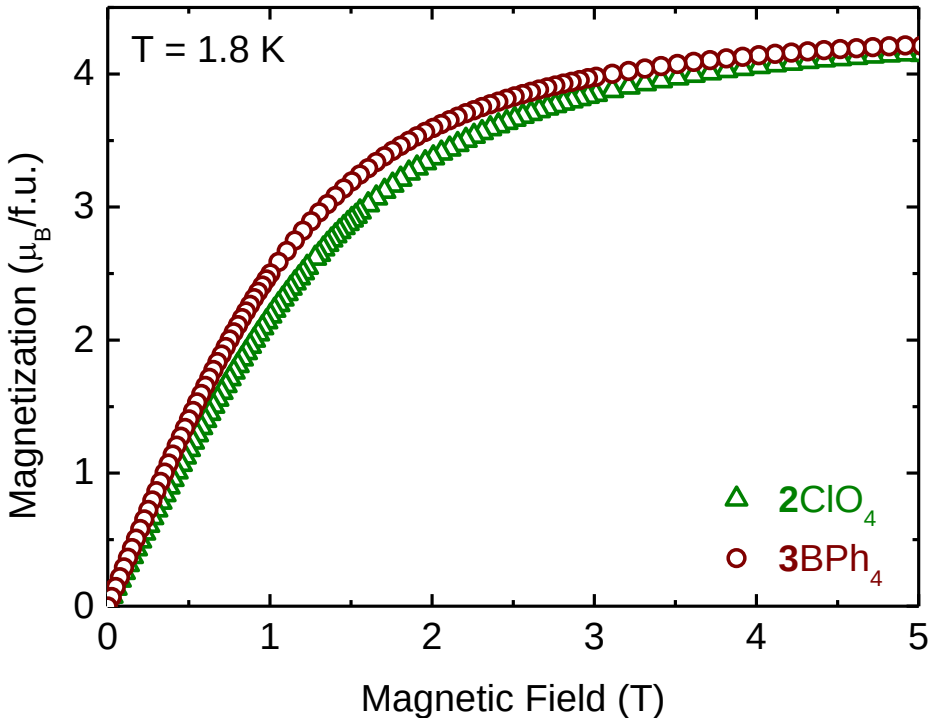

Figure 7.2: Magnetic field dependence of the static magnetization of $2ClO_4$ and $4BPh_4$ measured at $T = 1.8$ K. The magnetization increases by increasing magnetic field. And it is saturated at 4.2 μ_B/f.u.. Both compounds show a similar behavior [104].

The temperature dependence of the magnetic susceptibility $\chi(T) = M(T)/B$ and the inverse susceptibility $\chi^{-1}(T)$ of both complexes at $B = 1$ T is shown in Fig. 7.3. The susceptibility $\chi(T)$ and the inverse susceptibility $\chi^{-1}(T)$ were simulated by the *julX* simulation program [43] by Y. Krupskaya with the following Hamiltonian,

$$H = J\vec{S}_1 \cdot \vec{S}_2, \tag{7.1}$$

where J is the Heisenberg exchange constant and S_1, S_2 are the spin operators. In Fig. 7.3, the fitting lines are plotted with black solid ones. The fitting reproduces the magnetic susceptibility data well which reveals a ferromagnetic coupling of 23 K and 26 K between the two Ni^{2+} ions for $2ClO_4$ and for $4BPh_4$, respectively. The coupling between Ni^{2+} ions of $4BPh_4$ is slightly stronger than $2ClO_4$.

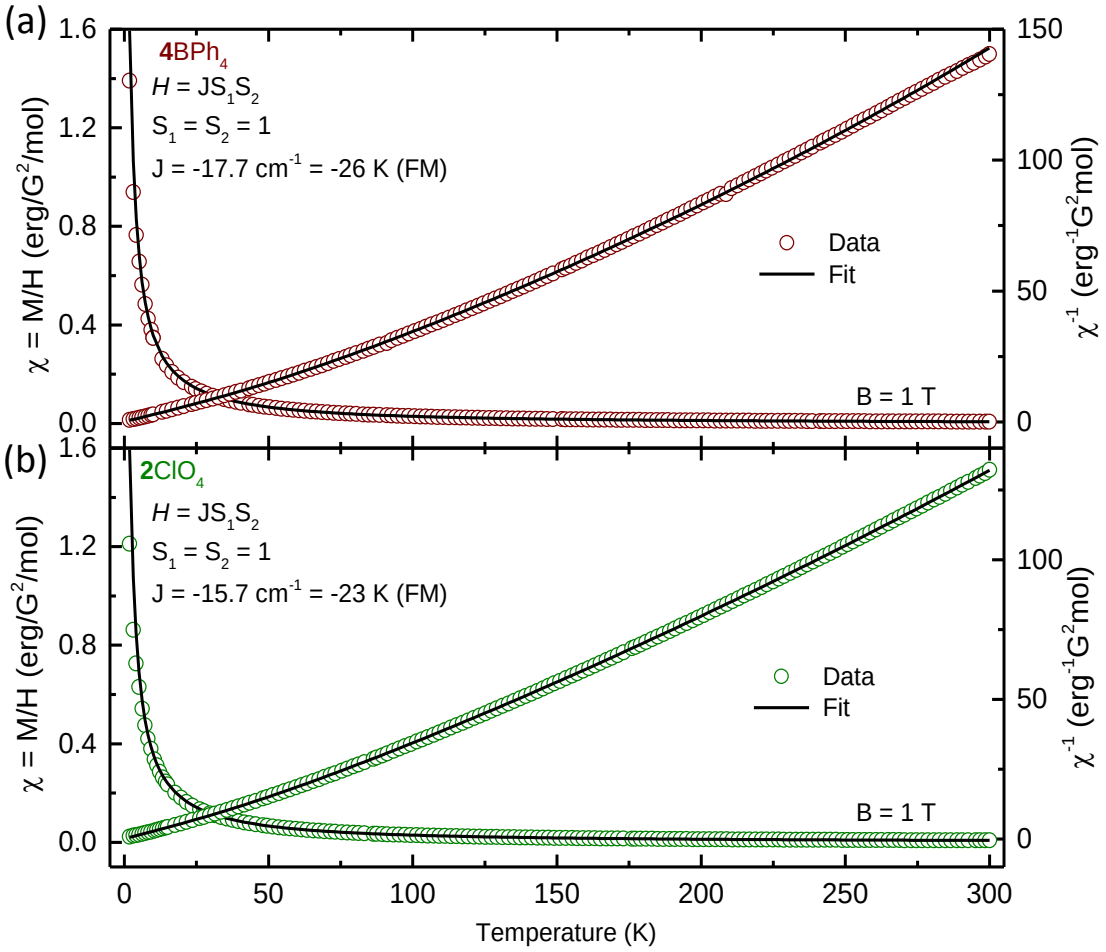

Figure 7.3: Temperature dependence of the static magnetic susceptibility, $\chi = M/B$ and the inverse susceptibility χ^{-1} of (a) $2ClO_4$ and (b) $4BPh_4$ measured at $B = 1$ T. Black lines correspond to experimental data using the Equation (7.1). Both complexes exhibit ferromagnetic couplings [104].

HF-ESR Measurements The $2ClO_4$ and $4BPh_4$ complexes are measured as oriented powders in magnetic fields up to 15 T within the temperature range from 4 K to 20 K at $\nu = 332$ GHz. Typical ESR spectra of $2ClO_4$ and $4BPh_4$ are plotted in Fig. 7.4.

Fig. 7.4 (a) shows the temperature dependent ESR spectra for $2ClO_4$. New peaks are appearing one by one when the temperature increases from 4 K to 20

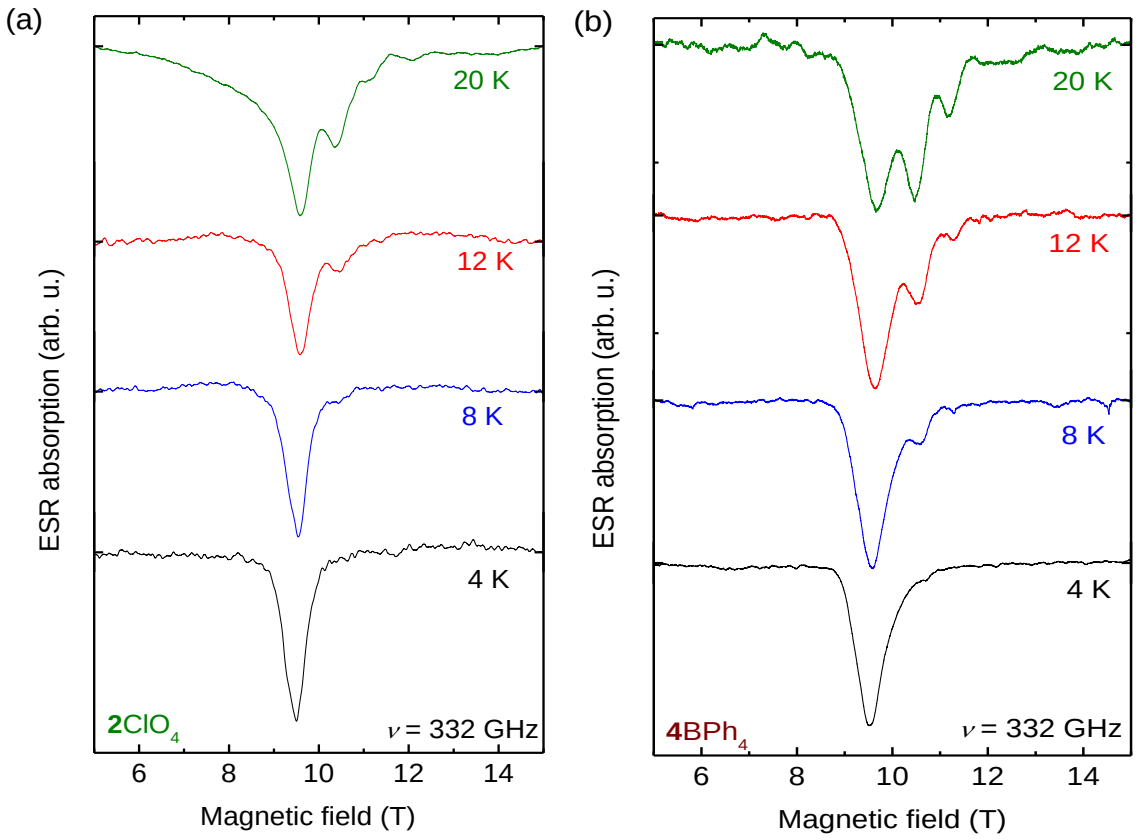

Figure 7.4: The temperature dependence of the ESR spectra of (a) $2ClO_4$ and (b) $4BPh_4$ at $\nu = 332$ GHz. Negative magnetic anisotropy is suggested with the change of the intensity of spectra according to the change of the temperature [104].

K. There are four resonance peaks at $T = 20$ K corresponding to the total spin $S = 2$. The important phenomenon is the change of the intensity depending on the temperatures. The intensities of four peaks are moved to the first resonance peak at lowest field when the temperature decreases to 4 K. This means that the axial magnetic anisotropy of the molecules is negative ($D < 0$).

The temperature dependent ESR spectra for $4BPh_4$ is shown in Fig. 7.4 (b). At $T = 20$ K, also four resonance lines are observed. Similar to $2ClO_4$, the observed spectral weight moves to lower magnetic fields when the temperature decreases, which demonstrates to the negative magnetic anisotropy.

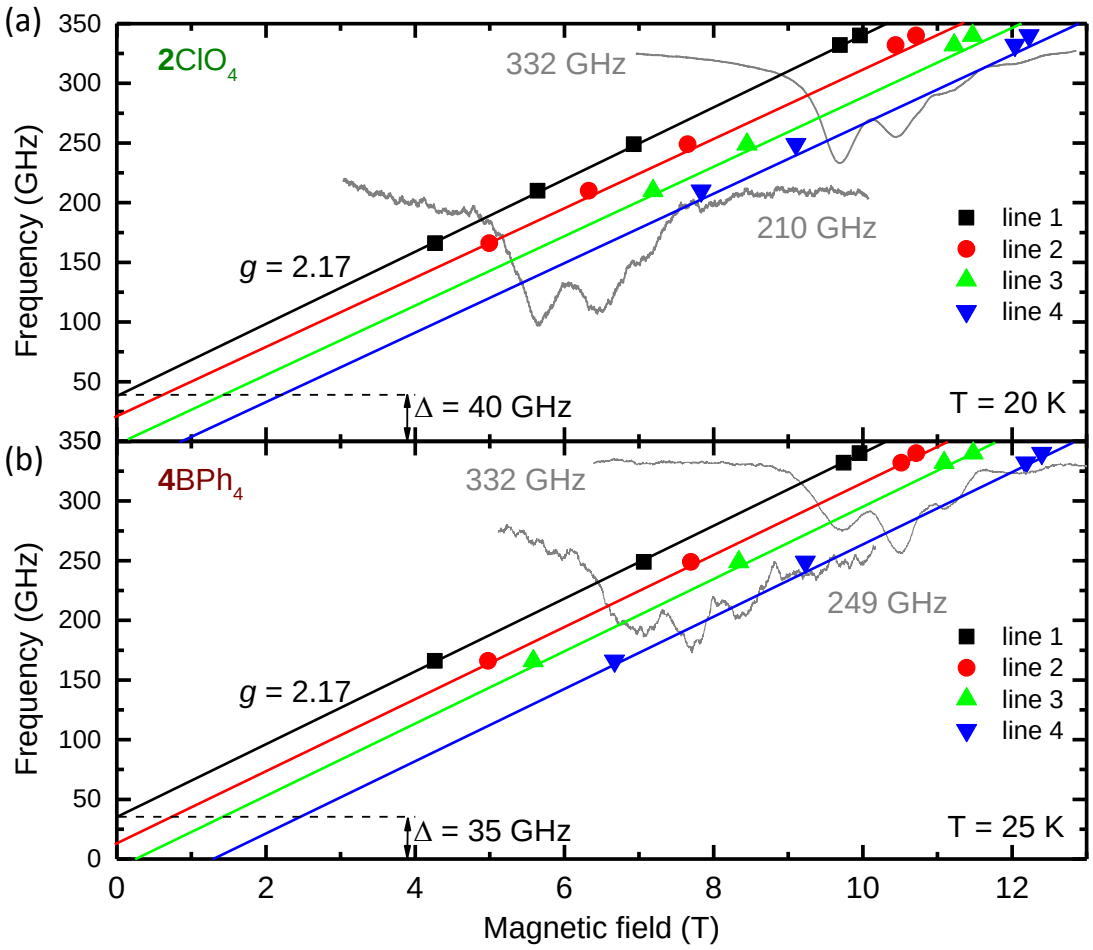

Figure 7.5: The frequency dependence of the ESR spectrum of (a) $2ClO_4$ at $T = 20$ K and (b) $4BPh_4$ at $T = 25$ K [104]. In both materials, there is the same g-factor of 2.17. Also, the ZFS are 40 GHz and 35 GHz for $2ClO_4$ and $4BPh_4$, respectively.

This change of the spectral weight can be explained by the change of the temperature dependent population. Firstly, $2ClO_4$ and $4BPh_4$ have the same total spin number $S = 2$ which yields to the five spin energy states $|-2\rangle$, $|-1\rangle$, $\cdots$, and $|+2\rangle$ in magnetic field. Due to the negative uniaxial anisotropy, the state $|\pm 2\rangle$ lie the lowest. According to the Boltzmann distribution, the population on the lowest spin state is higher than the other spin states at low temperature. Hence, the transition between $|-2\rangle \rightarrow |-1\rangle$ occurs at lower magnetic field much

more than the transition between $|-1\rangle \rightarrow |0\rangle$, and the peak at lower field has the highest intensity at low temperatures. When the temperature increases the population on the higher spin states increases as much as reduced the population on the lowest spin state. Therefore, at high temperature, the intensity of the peak at lower field decreases and the intensity of the higher field increases. The higher temperature up, the more ESR peaks appear. When the temperature reaches at certain point, all the spin states have the same population. Finally, ESR peaks disappear at high enough temperatures.

The ESR spectra for $2ClO_4$ and $4BPh_4$ are measured in magnetic fields up to 15 T at $T = 20$ K in the frequency range of $\nu = 150 - 330$ GHz. The frequency dependencies for $2ClO_4$ and $4BPh_4$ with representative ESR spectra are shown in Fig. 7.5. There are four resonance peaks in every ESR spectrum. The resonance fields are plotted with symbols in the figure. Linear slopes of them mean a g-factor of the sample by the resonance condition of $g = h\nu/\mu_B H_r$. A calculation reveals the $2ClO_4$ and the $4BPh_4$ have the same g-factor of 2.17. The extrapolation of the first resonance line (line 1) of both compounds reveals the zero field splitting (ZFS); 40 GHz and 35 GHz for $2ClO_4$ and $4BPh_4$, respectively.

7.3. Discussion

In order to analyze the ESR spectra of $2ClO_4$ and $4BPh_4$, the giant spin model Hamiltonian (Equation (1.53)) is applied. Also, the ZFS can be calculated from the magnetic anisotropy D. Simply, the ZFS Δ is the difference between the state $|\, 2, -2 >$ and the state $|\, 2, -1 >$. Therefore, it is,

$$\Delta = |D| \left(S_z^2 - (S_z - 1)^2 \right), \tag{7.2}$$

Considering the negative sign of the magnetic anisotropy, $|D|$ are - 13.3 GHz ($\sim$ - 0.63 K) and - 11.6 GHz ($\sim$ - 0.56 K) for $2ClO_4$ and $4BPh_4$, respectively.

Due to the magnetic anisotropy, the powder samples $2ClO_4$ and $4BPh_4$ are oriented along a preferred axis that the molecule acquires a minimum energy in the applied magnetic field. This preferred axis is called the easy axis. For a simulation of ESR spectra, it is assumed a parallel orientation of the easy axis to the external magnetic field. The simulation of the ESR spectra was done for $\nu =$ 332 GHz, $T = 20$ K by *EasySpin* [45]. The simulation parameters are the total spin $S_{\mathrm{tot}} = 2$, the g-factor of 2.17 for both compounds and the different value of the magnetic anisotropies $|D|$ of 13.3 GHz and 11.6 GHz for $2ClO_4$ and $4BPh_4$, respectively.

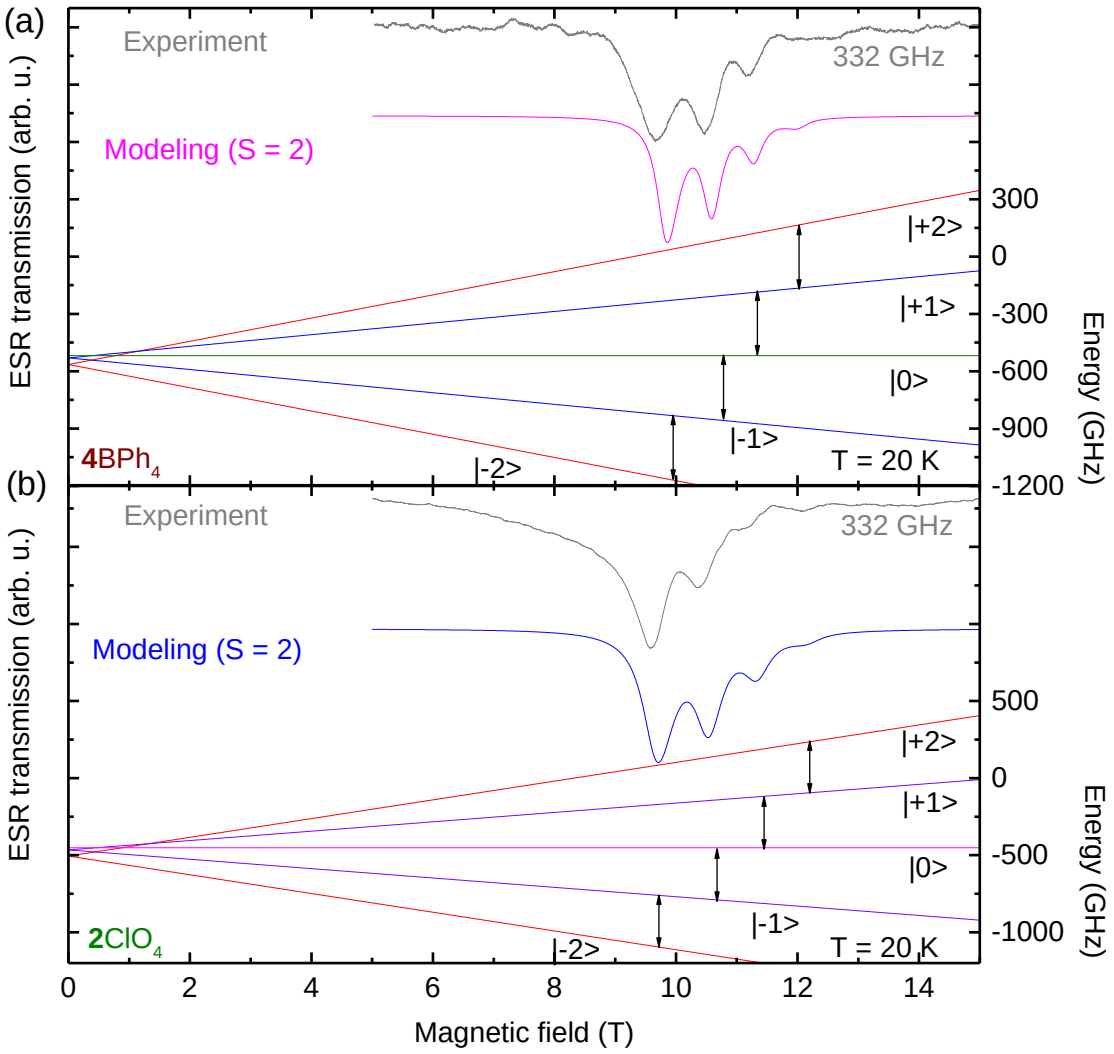

Figure 7.6: Experimental and simulated ESR spectra at $\nu = 332$ GHz, $T = 20$ K and corresponding energy level diagrams for (a) $2ClO_4$ and (b) $4BPh_4$. The simulation ESR spectra, red line for (a) and blue line for (b), reproduce the four resonance line of the experimental data [104].

The experimental and simulated ESR spectra are shown in Fig. 7.6 together. The simulation of the $4BPh_4$ at 4 K is shown in Fig. 7.6 (a). The experimental data (gray line) is reproduced well by the simulation line (red line). Also, the

resonance positions are well matched with the energy levels. Fig. 7.6 (b) shows the simulation of the $2ClO_4$. The simulation line (blue line) reproduces the experimental data (gray line) well according to the energy level diagram. Therefore, the parameters of the negative magnetic anisotropy, the g-factor are reasonable values.

7.4. Summary

Magnetization data on $2ClO_4$ and $4BPh_4$ shows the saturated magnetizations $M_s = 4.2\,\mu_B$/f.u. for both complexes corresponding to the total spin $S = 2$ in the magnetic ground state.
The frequency dependence of HF-ESR measurements on $4BPh_4$ show a g-factor of 2.17 and ZFS of 40 GHz ($\sim$ 1.9 K). The uniaxial magnetic anisotropy $D = -13.3$ GHz ($\sim$ 0.63 K) is negative which implies it is a magnetic easy axis. Hence, it has a bistable magnetic ground state where the energy levels $+2$ and -2 lie lowest in double potential wells.
The other complex, $2ClO_4$, has a g-factor of 2.17 and ZFS of 35 GHz ($\sim$ 1.7 K) and a negative uniaxial anisotropy D = - 11.6 GHz ($\sim$ 0.56 K). Similarly, $2ClO_4$ has a bistable magnetic ground state.
Magnetization and ESR measurements show no significant difference between $2ClO_4$ and $4BPh_4$. Therefore, one concludes that one Au atom does not significantly change the magnetic properties of the Ni^{2+} dimer complex. Although one Au atom causes an insignificant influence on the Ni^{2+} dimer complex, this is a possibility to deposit them on an Au surface. Further study can be found in the Ref. [104].

8. Mixed Valence Dinuclear Complex Ni(II)Ni(III)

Valence is a measure of how strong an element forms a chemical bond with another one. It was used to compute electrons forming bonds before the twenty first century. However, the term of the oxidation state is more widely employed [106]. Nowadays, valence is used as 'mixed valence' to indicate a certain situation such as Fe_3O_4. In a Fe_3O_4 compound, Fe ion has two different oxidation states, i.e. Fe^{2+} and Fe^{3+} leading to different number of electrons [107]. Note that Fe^{2+} and Fe^{3+} indicate the different formal oxidation states while the actual oxidation state can be different and the associated charge disproportionateness may be much smaller.

8.1. Crystal Structure

In the chemical point of view, mixed valence compounds are classified by the existence of delocalization of an extra electron [108]. In this chapter, the Ni^{2+}

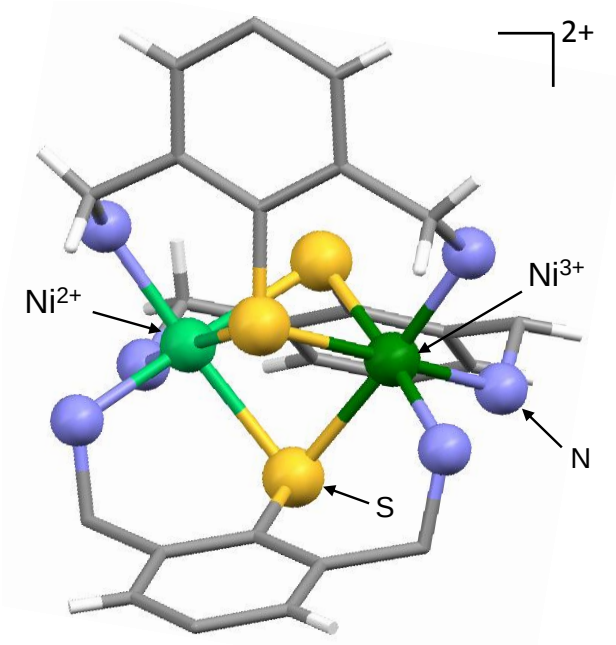

Figure 8.1: Structure of mixed valence complex $[Ni(III)Ni(II)(L^{DA})](BPh_4)_2$. Ni^{2+} and Ni^{3+} are connected by three sulphur bridges. The green, dark green, yellow, violet balls represent Ni^{2+}, Ni^{3+}, sulfur and nitrogen, respectively [110].

and Ni^{3+} ions form a mixed valence compound with the half-integer spin system. Fig. 8.1 shows the mixed valence dinuclear complex $[Ni(III)Ni(II)(L^{DA})](BPh_4)_2$ where L^{DA} indicates the tridentate N_2S ligand 2,6-di(aminomethyl)-4-tert-butyl-thiophenol [109]. It has been synthesized by the group of Prof. Kersting at TU Leipzig. The details of the synthesis and the structure were published [110].

The dinuclear $[Ni_2L_3]^{2+}$ complex is constituted by two units of N_3S_3Ni [110]. Two Ni ions are connected by three tiolate sulfur atoms. The average bond lengths of Ni-N and Ni-S are 2.089 Å and 2.380 Å, respectively [110]. The distance between the two Ni^{2+} ions is 3.064(1) Å and the average angle Ni-S-Ni is 80.16° [110]. Due to different oxidation states, the Ni(III) ion has shorter Ni-N and Ni-S bond lengths than the distance between the sulfur and the nitrogen and the Ni(II) ion. The average bond lengths of Ni(III)-N and Ni(III)-S are 2.085(3) Å and 2.3659(9) Å, respectively. The average bond lengths of Ni(II)-N and Ni(II)-S are 2.0923(3) Å and 2.395(10) Å, respectively [110].

8.2. Magnetization and HF-ESR: Experimental Results

Static magnetization measurements Static magnetization measurements of the mixed valence Ni(II)Ni(III) complex were performed by Y. Krupskaya at IFW Dresden with a SQUID magnetometer in the temperature range from 2 to 300 K in magnetic fields up to 7 T. Fig. 8.2 shows the field dependence of the magnetization of Ni(II)Ni(III) at $T = 1.8$ K. The saturated magnetization is ~ 3 μ_B which corresponds to a magnetic ground state of a total spin $S_{\text{tot}} = 3/2$ with $g = 2$. Also, it implies ferromagnetic coupling between the Ni^{2+} ion ($3d^8$, $S = 1$) and the Ni^{3+} ($3d^7$, $S = 1/2$).

The Ni^{3+} ion of the sample has the total spin $S = 1/2$ which is the low spin state. The Ni^{3+} ion has seven spins on five d-orbitals. According to the Pauli exclusion principle and the first Hund's rule, the seven spins fill one by one the five d-orbitals. However, in the case of cubic symmetry, there is an energy gap between e_g and t_{2g} levels. The t_{2g} is preferably occupied, because the energy cost of placing of a pair of spins on the t_{2g} state is less than the energy cost of placing spins in the e_g orbital state. Therefore, for Ni^{3+}, t_{2g} is fully filled up and then e_g is filled resulting in $S = 1/2$.

The temperature dependence of the magnetic susceptibility $\chi(T) = M(T)/B$ and the inverse susceptibility $\chi^{-1}(T)$ at $B = 1$ T are shown in Fig. 8.3. The susceptibility $\chi(T)$ and the inverse susceptibility $\chi^{-1}(T)$ were simulated by the *julX*

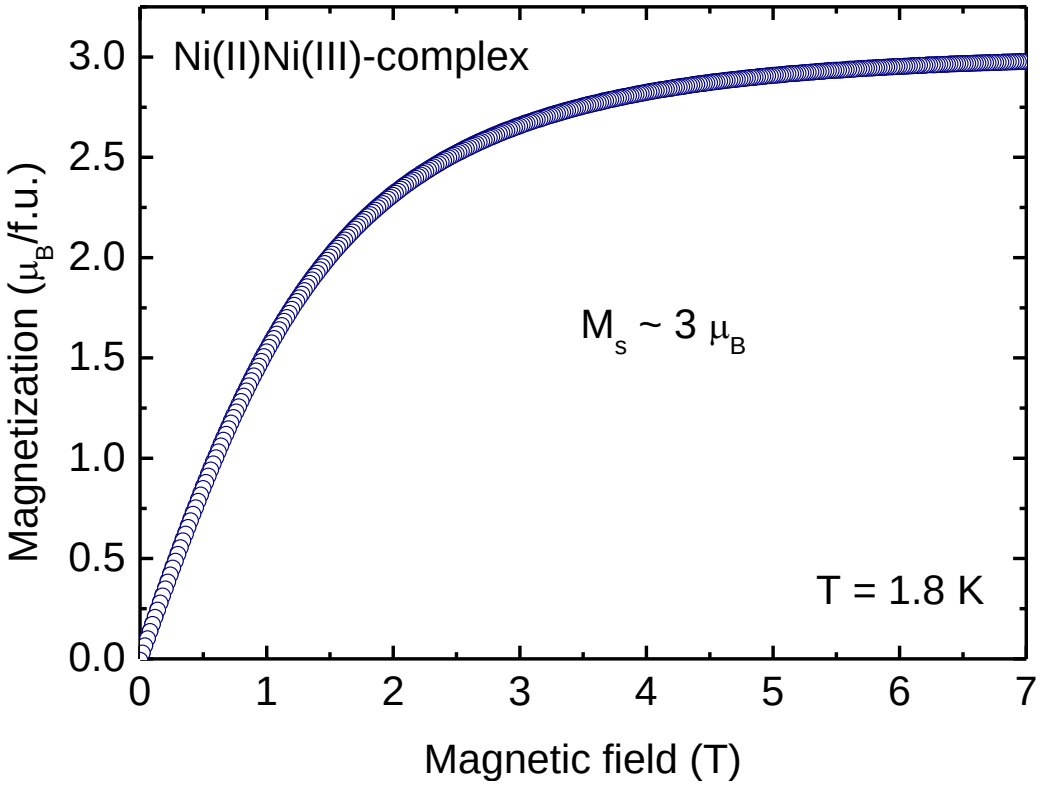

Figure 8.2: Magnetic field dependence of the static magnetization of Ni(II)Ni(III) at $T = 1.8$ K. The saturation magnetization is $\sim 3\ \mu_B$/f.u.. It indicates a ferromagnetic coupling [Y.Krupskaya].

simulation program [43] by using the equation (7.1). In Fig. 8.3, the simulation line (red line) reproduces the susceptibility curve which reveals a ferromagnetic coupling of ~ 48.5 K between the Ni^{2+} and the Ni^{3+} ions. There is temperature independent diamagnetic susceptibility χ_0 of $-1.153 \cdot 10^{-3}$ erg/G^2/mole which is caused by the non-magnetic ions of the organic ligands. Also, the analysis of the susceptibility curve reveals 25.9 % of independent paramagnetic impurity of $S = 1/2$.

HF-ESR Measurements Ni(II)Ni(III) was measured as oriented powder in the temperature range from 4 K to 20 K at $\nu = 249$ GHz. The temperature dependence of the ESR spectrum of the sample is presented in Fig. 8.4. At 4 K, there are two resonance peaks at 6.66 T and 8.25 T. At $T = 12$ K, a new peak appears at

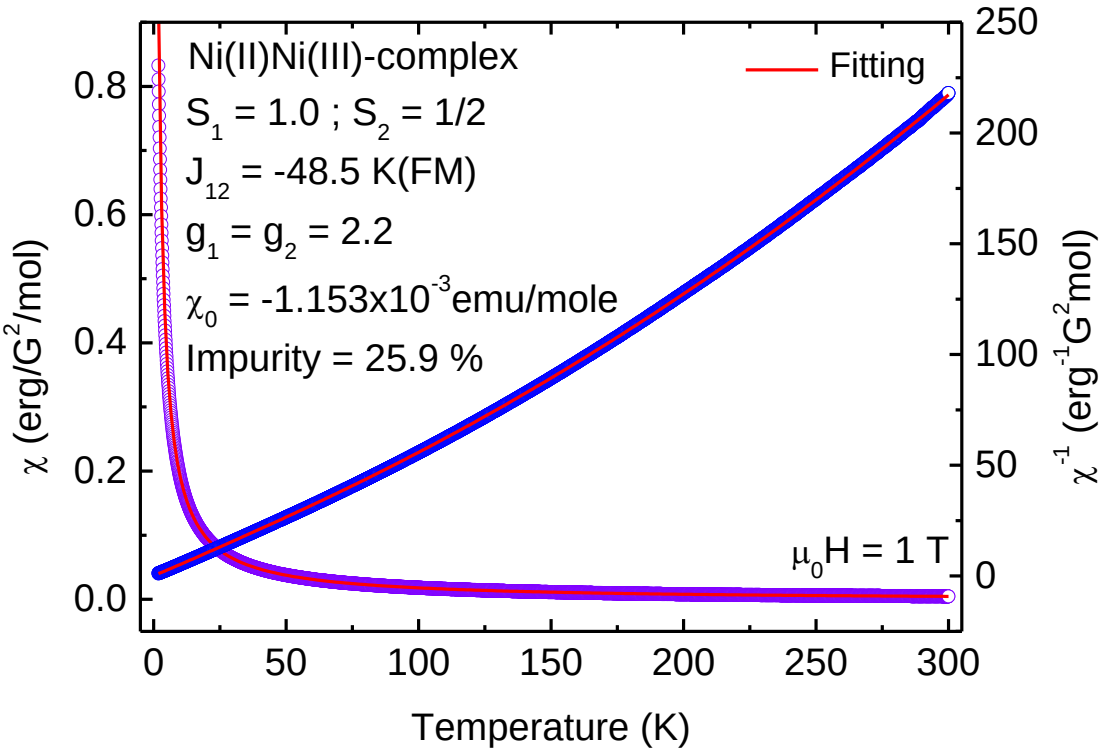

Figure 8.3: Temperature dependence of the static magnetic susceptibility, $\chi = M/B$ and the inverse susceptibility χ^{-1} of Ni(II)Ni(III) at $B = 1$ T. Red line is the simulation.

9.9 T. Finally, at $T = 20$ K, there are three main resonance peaks at 6.66 T, 8.25 T and 9.9 T corresponding to the transitions between spin states of $S_{\text{tot}} = 3/2$ of the molecule, i.e., $\mid 3/2, -3/2 > \rightarrow \mid 3/2, -1/2 >$, $\mid 3/2, -1/2 > \rightarrow \mid 3/2, 1/2 >$, and $\mid 3/2, 1/2 > \rightarrow \mid 3/2, 3/2 >$. When the temperature decreases, the intensity of the peaks at higher fields is shifted to the peaks at lower fields. This change of the spectral weight indicates a negative axial magnetic anisotropy of the molecule ($D < 0$).

There are additional small peak features around the main ESR resonance peaks. Due to the inhomogeneous local environment, each spin in the sample has slightly different local field, resulting in the misalignment of the spins in the applied magnetic fields. The resonances of the misaligned spins appear at slightly different magnetic fields from main resonance feature. In analysis, they are not considered because they are not main features of this sample.

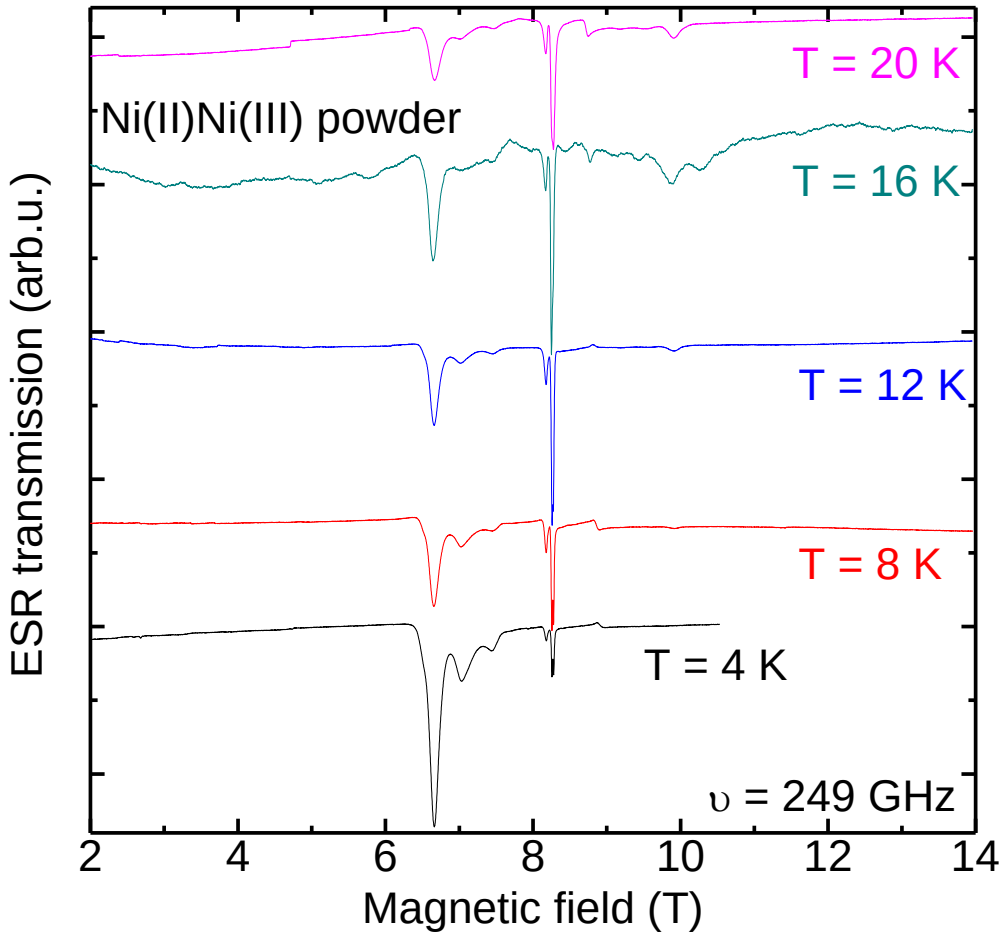

Figure 8.4: Temperature dependence of the HF-ESR resonance spectra at 249 GHz. Three resonance peaks appear at 20 K. When the temperature decreases, the spectral weight moves to the lower magnetic field which means a negative uniaxial magnetic anisotropy ($D < 0$).

In addition, HF-ESR measurements were performed on a loose powder sample in a magnetic field up to 13 T at 4 K at frequencies of 83, 166, 249, 332 GHz. Fig. 8.5 shows the frequencies versus magnetic fields of ESR resonance lines with representative ESR spectra. An ESR spectrum at 4 K exhibits three separate ESR lines. The blue resonance line reveals a g-factor of 4.2 which is almost twice bigger than the red lines. This demonstrates that the first resonance is a forbidden one which is presumptively associated with $\Delta m_s = \pm 2$. The forbidden

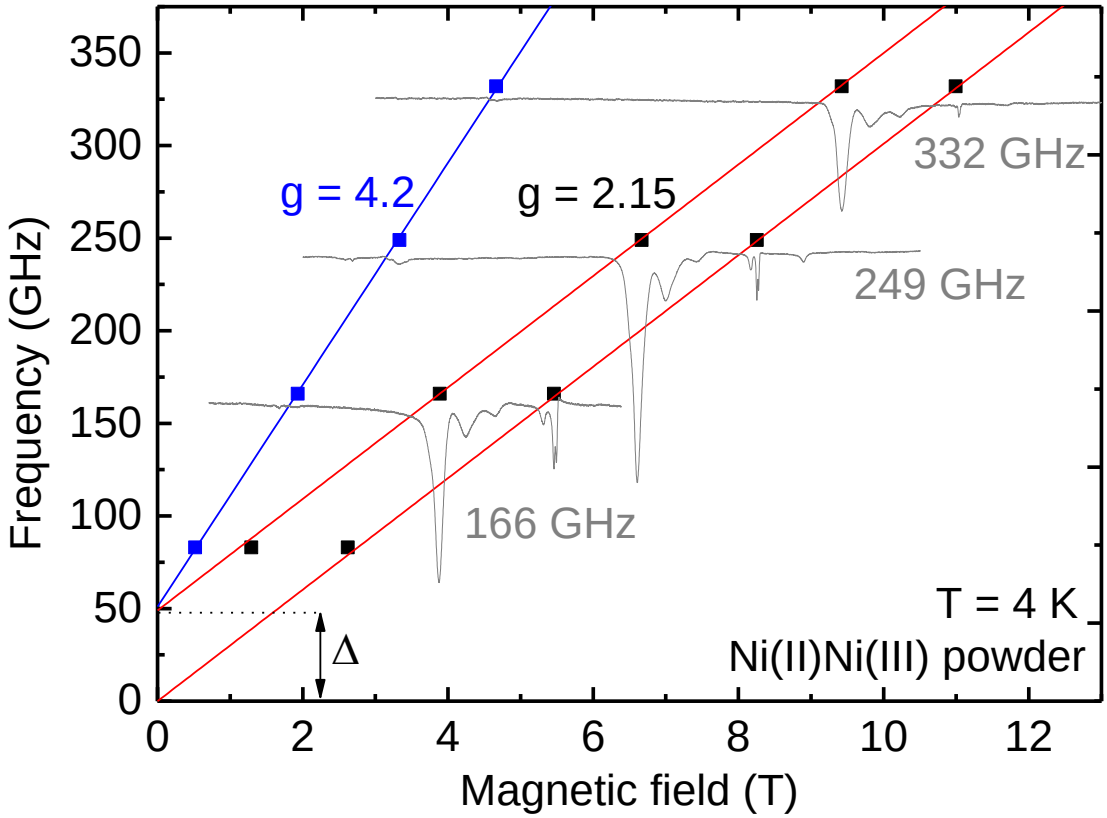

Figure 8.5: Frequency dependence of the ESR spectrum of Ni(II)Ni(III) at 4 K. Three g-factors of 3.7 (black line), 2.2 (red line) and 2.1 (blue line) are obtained for each resonance peak. There is a ZFS of 50 GHz.

transition occurs by an admixture of spin states by the off-diagonal terms in a spin Hamiltonian which considers an angle between z-axis of a crystal field and z'-axis of the direction of an applied magnetic field [111]. The red resonance lines have a g-factors of 2.15, and the extrapolation of the second resonance line to $H = 0$ implies a ZFS of 49 GHz ($\sim$ 2.4 K).

Fig. 8.6 shows the frequency dependence of the ESR spectra at 20 K. There are three resonance peaks for spin system $S = 3/2$. Three resonance lines reveal the g-factors of 2.15. The extrapolation of the first resonance line to $H = 0$ implies a ZFS of 49 GHz ($\sim$ 2.4 K).

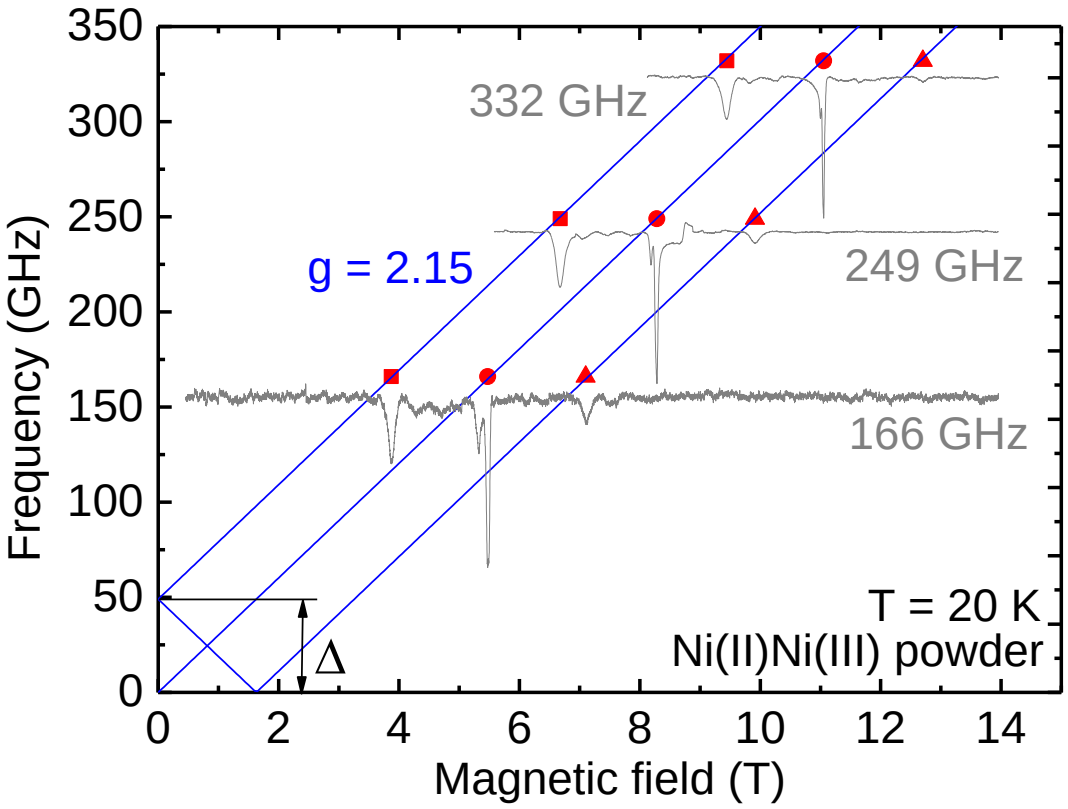

Figure 8.6: Frequency dependence of the ESR spectrum of Ni(II)Ni(III) at $T = 20$ K. the ZFS is 50 GHz. There are three resonance lines which corresponds to the total spin $S = 3/2$. The g-factor of the resonance lines is 2.15.

8.3. Discussion

For the analysis, a parallel orientation of the magnetic anisotropy axis along the magnetic fields is assumed. To analyze the ESR spectra, only the ground spin multiplet state is considered, because all three resonance peaks appearing at 20 K correspond to the ground spin multiplet state of the molecule. Note that not only a system of $S = 3/2$ but also a spin system of $S = 1/2$ is considered due to the impurity 25.9 % from the analysis of the susceptibility data. The Hamiltonian of the system can be written as,

$$H = \left[D \left(S_{1z}^2 + \frac{1}{3} S(S+1) \right) + \mu_B g \vec{S}_1 \cdot \vec{B} \right] + \mu_B g \vec{S}_2 \cdot \vec{B}. \tag{8.1}$$

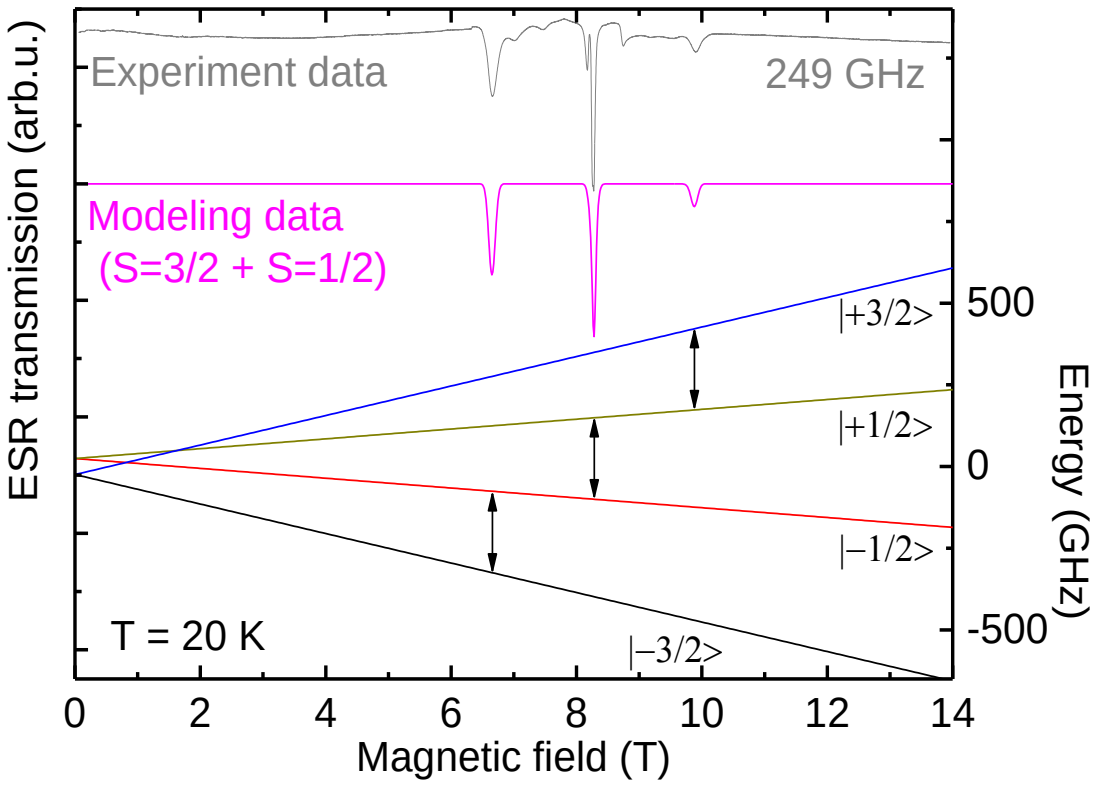

Figure 8.7: Experimental and simulated ESR spectra and corresponding energy level diagrams for Ni(II)Ni(III) at $\nu = 249$ GHz, $T = 20$ K. simulated data reproduce the experiment data well. Their resonances occur between the neighboring spin states.

The first two terms mean the spin system $S_1 = 3/2$ with an anisotropy and the last term indicates the spin system $S_2 = 1/2$. The first term accounts for a splitting among spin states at zero field due to the magnetic anisotropy. D is the uniaxial magnetic anisotropy parameter. The second and third terms are the Zeeman effect. Based on the experimental data, parameters for a simulation are g-factor of 2.15 and D = -24.5 GHz which is calculated by $\mid D \mid = \Delta / \left(S_{\mathrm{tot}}^2 - (S_{\mathrm{tot}} - 1)^2\right)$. A simulated spectrum by *EasySpin* [45] with the experimental spectrum at $\nu =$ 249 GHz and at $T = 20$ K, and the corresponding energy level diagram are shown in Fig. 8.7. The simulation spectrum reproduce the three observed ESR lines well which corresponds to a total spin of $S_{\mathrm{tot}} = 3/2$. Also, the simulation confirms the ZFS of 49 GHz and the negative sign of the uniaxial magnetic anisotropy of - 24.5 GHz. The second peak of the system of $S = 3/2$ is overlapped with a

single resonance peak of the system of $S = 1/2$. Due to this impurity the second resonance peak has the strongest intensity.

8.4. Summary

Magnetization data shows that the Ni-ions in Fig. 8.1 are coupled ferromagnetically leading to the saturation magnetization $M_s \sim 3\mu_B$/f.u. which corresponds to a total spin of $S_{tot} = 3/2$ in the magnetic ground state. The analysis of the susceptibility data reveals a ferromagnetic coupling of -48.5 K, a diamagnetic susceptibility of -1.153 $\times$ 10^{-3} erg/G^2/mole and an impurity of 25.9 % from a spin system $S = 1$. From the frequency dependent ESR measurements, three resonance lines are obtained. At 4 K, the g-factors of them are 4.2 and 2.15 which correspond to a forbidden transition and an allowed transitions, respectively. From the frequency dependent ESR spectra, at 20 K, there are three resonance peaks with the g-factors of 2.15. A uniaxial anisotropy $D = -24.5$ GHz corresponds to the zero field splitting of $\Delta = 49$ GHz (~ 2.4 K). Finally, the simulation reproduces the ESR spectrum at 249 GHz at 20 K well considering the effect of the impurity.

9. Gd Dimer Complex

Lanthanide (Ln) elements are called rare earth elements. They contain partially filled $4f$ orbitals which govern their magnetic properties. Usually, trivalent ions are realized in these elements. The outermost shell of Ln ions has the $5s^2 5p^6$ spin configuration [18]. It is possible to study the effect of $4f$-orbitals which are shielded by outermost electron shells. Contrary to the transition metal ions, Ln ions show the properties of the combination between the spin and orbital angular momentum. The results presented below have been submitted for publication [112].

9.1. Crystal Structure and Magnetic Properties

The dinuclear $[Gd(III)_2L(OAc)_4]$ PF_6 complex was synthesized by M. Grosshauser from the group of Prof. P. Comba at Heidelberg University. The crytal structure is shown in Fig. 9.1. It contains lanthanide(III) acetate salts and dinucleating ligands with methanol solvent. Two Gd^{3+} ions are connected by μ_2-OPh phenolate of the binucleating ligand and by two acetates. The distance between the two Gd^{3+} ions is 3.791 Å [112]. The L indicates the ligand which provides two

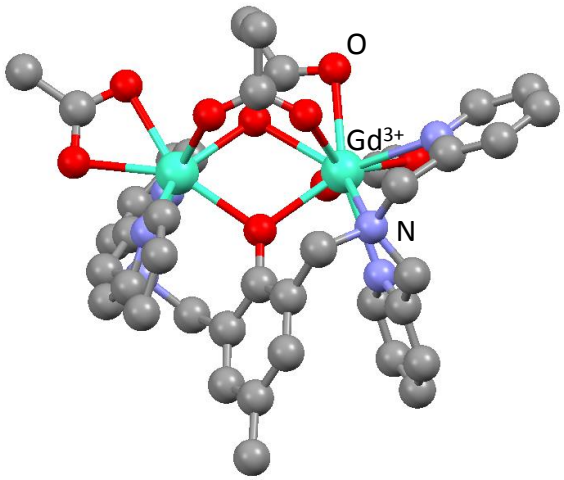

Figure 9.1: Structure of $[Gd(III)_2L(OAc)_4]$ PF_6. Two Gd^{3+} ions are connected by two oxygen bridges. The light green, red, and violet balls represent gadolinium, oxygen, and nitrogen, respectively [112].

pyridine and a tertiary amine donor to each site [112].

The magnetic susceptibility was measured on powder by M. Großerhauser [112]. At $T = 300$ K, $\chi_M T$ of the Gd dimer amount to 15.10 cm^3 K mole^{-1}, and the value of $\chi_M T$ decreases to 9.71 cm^3 K mole^{-1} at 2 K [112]. This indicates an antiferromagnetic (AFM) coupling between Gd^{3+} ions in the complex [112].

9.2. HF-ESR: Experimental Results

The HF-ESR measurements were performed on the powder dinuclear Gd^{3+} complex in magnetic fields up to 15 T and in the frequency range of $\nu = 32$ - 321 GHz at $T = 4$ K. Fig. 9.2 shows representative ESR spectra at $T = 4$ K. The plot shows ESR spectra with broad signals. Note that the spectra, however, exhibit distinct features where the absorption is maximal. A slope of the maximal absorption at low magnetic fields on all ESR spectra indicates a g-factor which is 2.01 ± 0.02. The extrapolation of the slope to $H = 0$ gives ZFS of $\Delta = 5.9 \pm 1.05$ GHz.

The temperature dependence of the ESR spectra of the dinuclear Gd^{3+} complex at 130 GHz is plotted in Fig. 9.3. From $T = 4$ K to $T = 40$ K, there is a pronounced shift of spectral weight to lower fields when the temperature decreases. This transfer of spectral weight shows a negative axial magnetic anisotropy of the molecule, $D < 0$, which implies the easy axis.

9.3. Discussion

The presence of magnetic anisotropy can be deduced from the detection of ZFS. In general, such a ZFS may originate from spin-orbit coupling and/or dipolar interaction. In most cases of the SMMs, the magnitudes of the dipolar interaction and the spin-orbit coupling are 10^{-1} cm^{-1} and $\sim 10^1$ cm^{-1}, respectively [19]. Thus, the dipolar interaction is usually ignored due to the relatively large magnetic anisotropy. In the case at hand, the orbital angular moment is not considered due to $L = 0$ of the half-filled $4f$-shells of the Gd^{3+} ion. Hence, the total angular moment is $J = S = 7/2$. Therefore, one expects vanishing spin-orbit coupling and may conclude that the experimentally observed ZFS is due to dipolar interaction.

Considering the dipolar interaction, the magnetic field by a dipole can be written as,

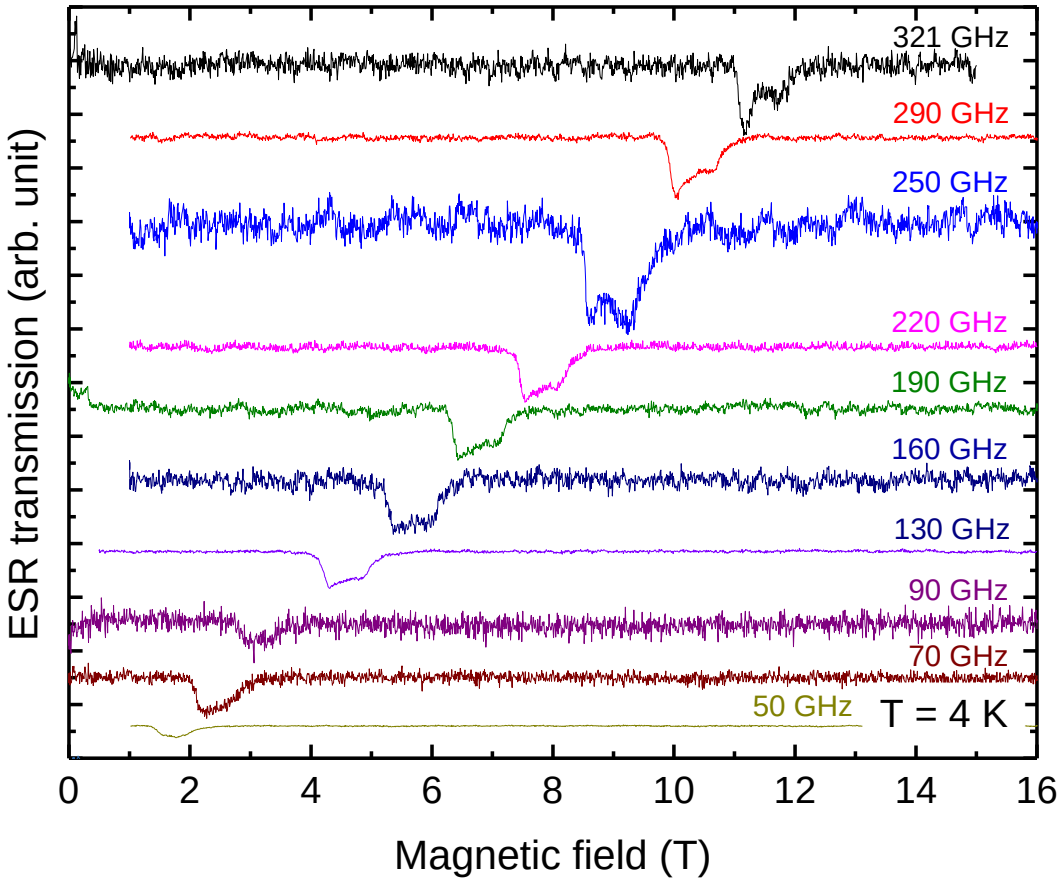

Figure 9.2: HF-ESR spectra of Gd^{3+} obtained at different frequencies $\nu = 50 - 320$ GHz.

$$\mathbf{B} = \frac{\mu_0}{4\pi}\frac{1}{r^5}\left[3\left(\mathbf{m}\cdot\mathbf{r}\right)\mathbf{r} - \mathbf{m}\right], \tag{9.1}$$

where μ_0 is the vacuum permeability of $4\pi \times 10^{-7}$ N/A^2, r is the distance between the two dipoles, $\mathbf{m}$ is the magnetic moment of the magnetic ion and $\mathbf{r}$ is the distance vector between two ions [52]. It is assumed that the magnetic dipole is aligned along the external magnetic field applied along the z-axis. Applying the value $g = 2.01$, the magnetic moment can be written as $\mathbf{m} = g\mu_B J \simeq 7.04\,\mu_B\,\widehat{z}$. These dipole make the magnetic field of $B = 0.24$ T $\simeq 0.32$ K (at $g = 2.01$). On the other hand, the exchange interaction J between Gd^{3+} ions is 0.13 cm^{-1} = 0.19 K as derived the analysis of χ_M [112], i.e, the magnetic field strength of the dipole is comparable to the exchange interaction and the magnetic field caused

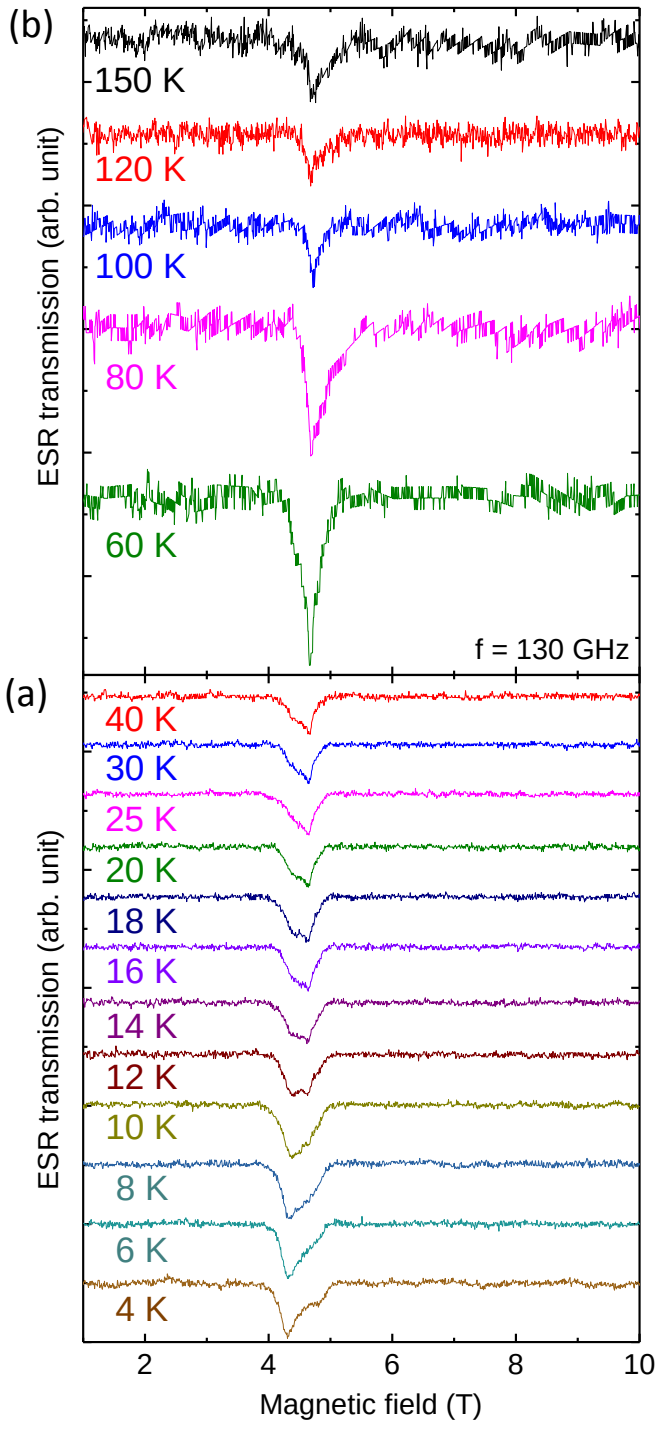

Figure 9.3: Temperature dependence of the ESR spectra at (a) T = 4 - 40 K and (b) T = 60 - 150 K, obtained at ν = 130 GHz. Resonance intensity in (b) are multiplied by a factor of 2 with respect to those in (a).

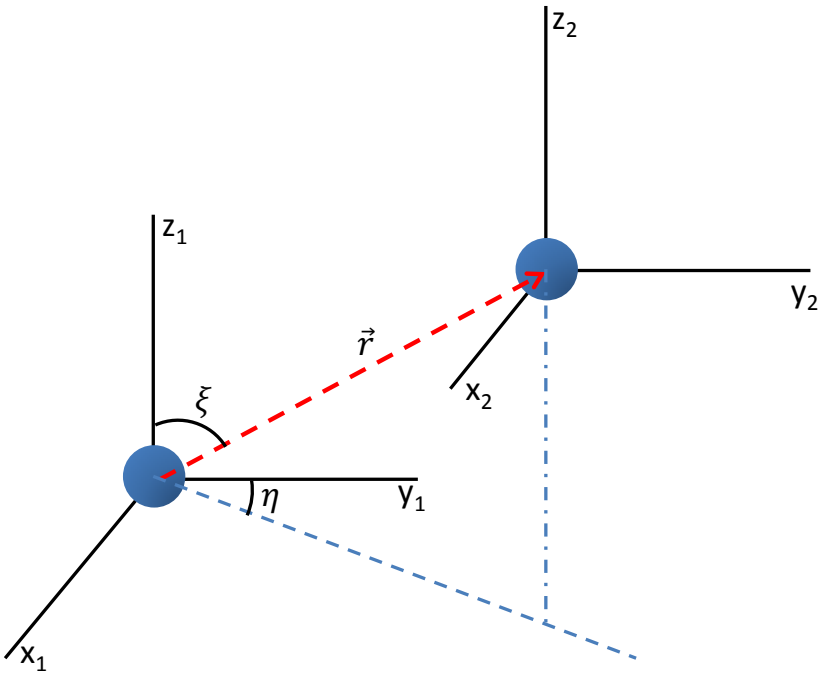

Figure 9.4: Two identical Gd^{3+} ions in principle coordinate axes. The blue balls are Gd^{3+} ions. r is the distance between them. ξ is the angle between the z-axis and the $\vec{r}$ and η is the angle between the y-axis and the projection of $\vec{r}$ [116].

by the dipolar interaction cannot be neglected [113, 114].

The two Gd^{3+} ions have their own coordinates as shown in Fig. 9.4. To calculate the magnetic anisotropy induced by the dipolar interaction there is the magnetic anisotropy tensor as follows [115, 116],

$$\mathbf{D}_{dipolar} = \begin{pmatrix} g_x^2(1-3\sin^2\eta\sin^2\xi) & -3g_xg_y\sin^2\xi\sin\eta\cos\eta & -3g_xg_z\sin^2\xi\cos\xi\sin\eta \\ -3g_yg_x\sin^2\xi\sin\eta\cos\eta & g_y^2(1-3\cos^2\eta\sin^2\xi) & -3g_yg_z\sin\xi\cos\xi\cos\eta \\ -3g_zg_x\sin\xi\cos\xi\sin\eta & -3g_zg_y\sin\xi\cos\xi\cos\eta & g_z^2(1-3\cos^2\xi) \end{pmatrix} (\mu_B^2/r^3), \tag{9.2}$$

where μ_B is the Bohr magneton, r is the distance between the two Gd^{3+} ions, η is the angle between the y-axis and the projection of $\vec{r}$ and ξ is the angle between the z-axis and $\vec{r}$. Equation (9.2) is applied for weakly coupled pairs of Gd^{3+} ions [116]. Equation(9.2) is applied to the following multiple spin Hamiltonian.

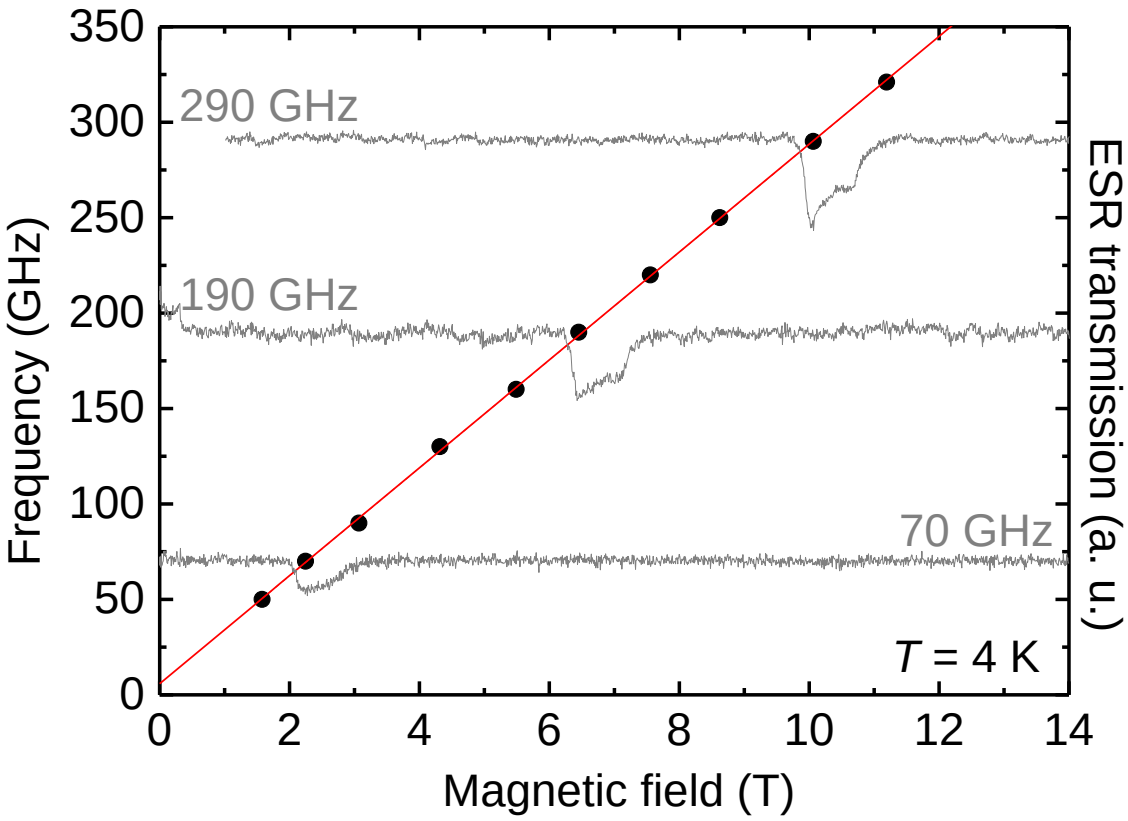

Figure 9.5: Frequency dependence of the ESR spectrum of Gd^{3+} dimer at 4 K. Red line represents the simulation of the resonance in the ground state when the magnetic field is applied parallel to the easy axis.

$$H = -J\mathbf{S}_1 \cdot \mathbf{S}_2 + g\mu_B \sum_{i=1}^{2} \mathbf{S}_i \cdot \mathbf{H} + \mathbf{S}_1 \cdot \mathbf{D}_{dipolar} \cdot \mathbf{S}_2, \tag{9.3}$$

where the first term describes the exchange interaction between two Gd^{3+} ions, the second term considers the Zeeman effect, and the third term represents the magnetic anisotropy of the system due to the dipolar interaction.

With the multiple spin Hamiltonian of Equation (9.3), the ground multiple spin state is reproduced. Fig. 9.5 shows the best simulation with the parameters of $\xi = 30°$, $\eta = 0°$, and $g_x = g_y = g_z \equiv g = 2.01$. The simulation line (red line) represents the simulation of the resonance in the ground state when the magnetic

field is applied parallel to the easy axis. Its result shows a ZFS of 6.00 GHz which agrees well with the experimental ZFS of 5.9 ±1.05 GHz.

9.4. Summary

HF-ESR studies on the aligned powder dinuclear Gd^{3+} complex show broad resonance spectra. The orbital angular moment of the Gd^{3+} is negligible because of $L = 0$. The origin of the magnetic anisotropy can be the dipolar interaction, not by the spin-orbit coupling. The coupling between the Gd^{3+} ions is 0.19 K which is small compared to the magnetic field of 0.33 K by the dipolar interaction. Considering the magnetic anisotropy induced by the dipolar interaction. The best simulation parameters are $\xi = 30°$, $\eta = 0°$ and $g = 2.01$. This means that $\vec{r}$, which is the distance vector between the two Gd^{3+} ions, is tilted as much as 30° from to the z axis. The simulation reproduced the ESR resonance line as well as the ZFS of 5.9 GHz which implies the easy axis of the system.

10. High-spin Cu_5 Complex

10.1. Crystal Structure and Magnetic Properties

The complex $(HNEt_3)_2Cu(II)[12\text{-}MC_{Cu(II)N(Shi)}\text{-}4]$ has been synthesized by the group of Prof. Rentschler at Universität Mainz. Its structure is shown in Fig. 10.1. The details of the synthesis and the structure were published [117]. The five Cu^{2+} ions are connected by oxygen and nitrogen atoms in a plain. The average bond lengths of Cu-O and Cu-N are 1.91(2) Å and 1.94(2) Å, respectively [117]. The average distance from the central Cu^{2+} ion to the other four Cu^{2+} ions is 3.2463(2) Å [117]. Also, four Cu^{2+} ions are bridged by oxygen with the Cu^{2+} ion in the center with the average angle of 117.22(5)° [117]. The Cu^{2+} ion in the center is connected to four oxygen ions with an average angle of 90.00(8)° [117].

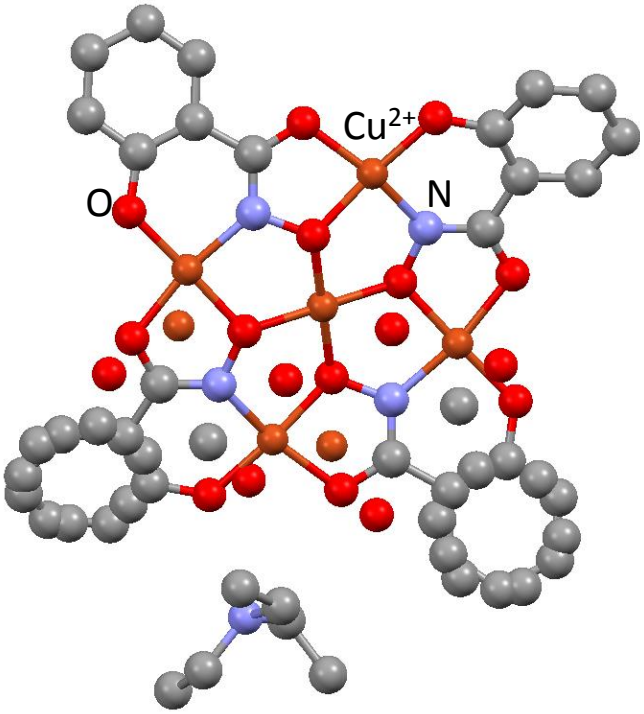

Figure 10.1: Structure of $(HNEt_3)_2Cu(II)[12\text{-}MC_{Cu(II)N(Shi)}\text{-}4]$. Five Cu^{2+} ions are connected to each other by oxygen and nitrogen bridges in a plane. The orange, red, light blue balls represent copper, oxygen and nitrogen, respectively [117].

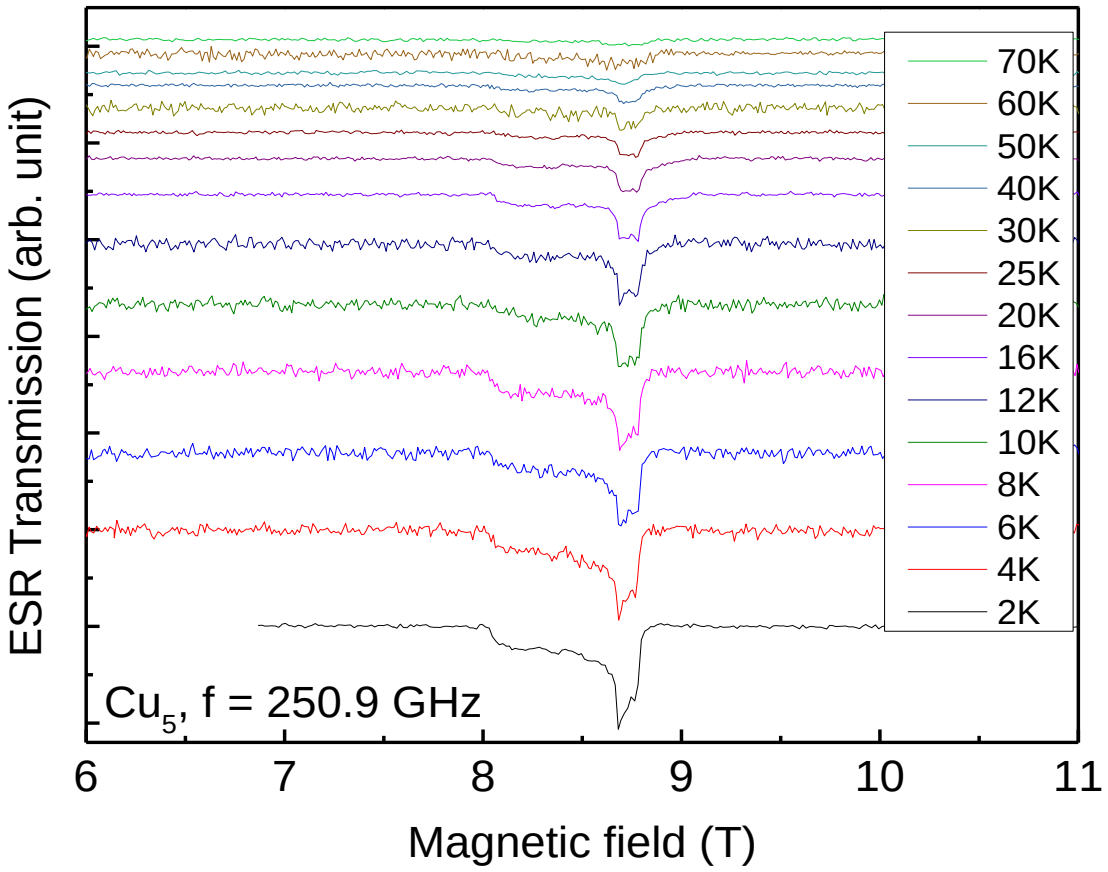

Figure 10.2: Temperature dependence of the ESR spectra of Cu_5 at $\nu =$ 250.9 GHz. Each ESR spectrum is broad and has a sharp peak at 8.76 T.

Static magnetization measurements on $(HNEt_3)_2Cu(II)[12\text{-}MC_{Cu(II)N(Shi)}\text{-}4]$ were performed in Mainz in the temperature range from 2 to 300 K in magnetic fields up to 7 T. The field dependence of the magnetization measured at $T = 2$ - 10 K. At 2 K, the saturated magnetization M_{sat} is $\sim 1.1\ \mu_B$ [117]. Also, there is a plateau below 60 K on the temperature dependence of the magnetic susceptibility χT curve which means the antiferromagnetic coupling among the Cu ions [117]. To analyze χT, the isotropic spin Hamiltonian is applied. Its result is all couplings are antiferromagnetic with $J_1 = 310.4\ cm^{-1}$ between Cu^{2+} ion at the center and four surrounding Cu^{2+} ions, and with $J_2 = 184.6\ cm^{-1}$ between four surrounding Cu^{2+} ions [117]. However, the ratio between these couplings is 1.7 which indicates a total spin $S = 1/2$ in the ground state [117].

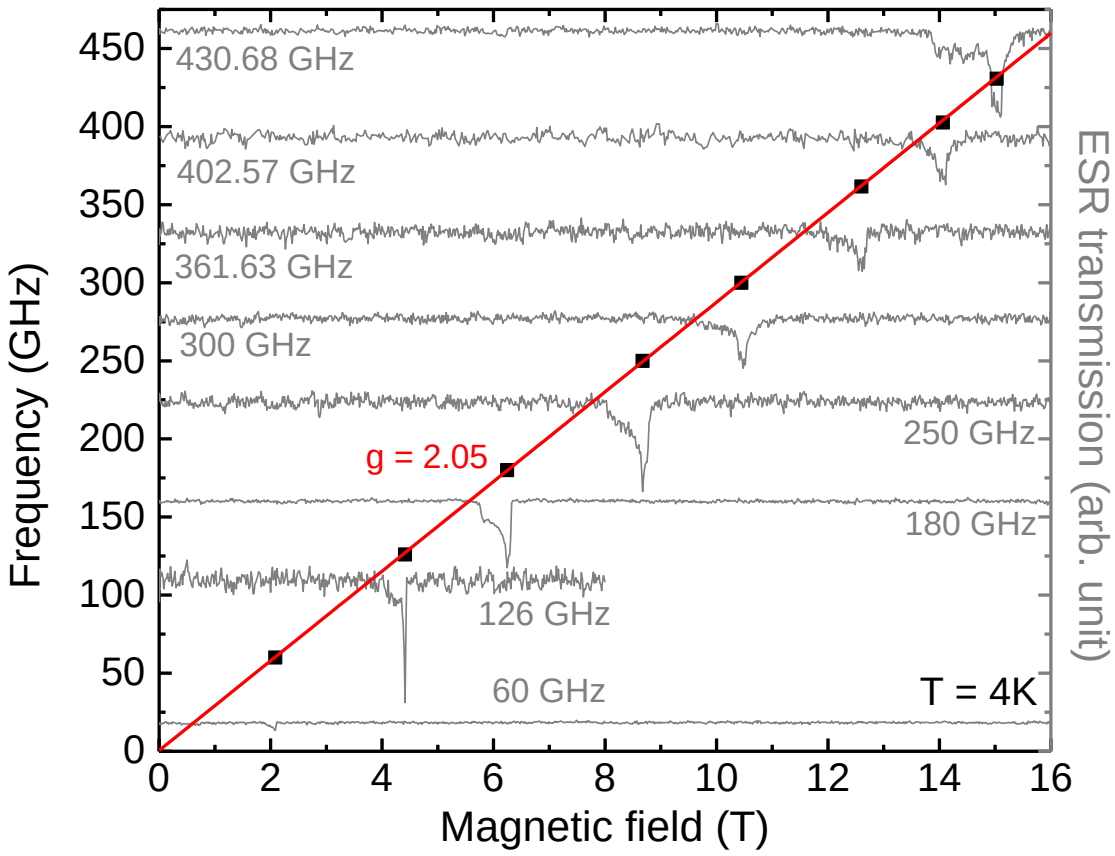

Figure 10.3: Magnetic field dependence of HF-ESR spectra of Cu_5 abstained at different frequencies $\nu = 60 - 430$ GHz.

10.2. HF-ESR: Experimental Results

Cu^{2+} ion has a spin configuration of $[Ar]\,3d^9$. Four of the five d-orbitals are fully occupied and there is one unpaired electron. According to the analysis of χT [117], the five Cu^{2+} ions make a total spin $S = 1/2$. The frequency dependent ESR measurements are performed in magnetic fields up to 16 T within the temperature range $T = 2 - 70$ K at the frequency $\nu = 250.9$ GHz. The ESR spectra of Cu_5 are plotted in Fig. 10.2. There is a broad resonance feature with a width of $\sim$ 1 T resonance width at $T = 4$ K. The intensity of the peak decreases when the temperature increases. Above $T = 70$ K, the ESR spectrum disappears.

The frequency dependence is measured in magnetic fields up to 16 T at $T = 4$

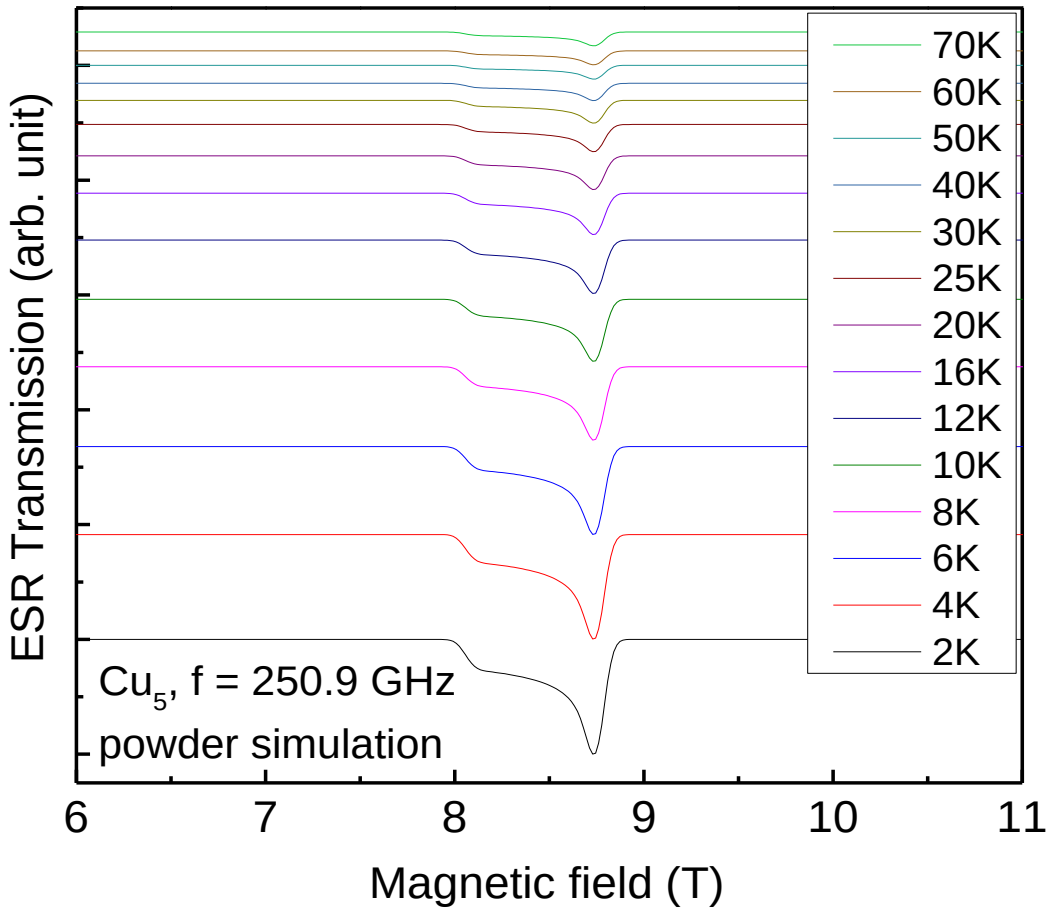

Figure 10.4: The temperature dependence of the powder simulation of Cu_5 at $\nu = 250.9$ GHz.

K in the range of $\nu = 60 - 430$ GHz. The frequency dependencies for Cu_5 with representative ESR spectra are shown in Fig. 10.3. The black dots are the magnetic field of a peak positions with which is high intensity in the broad spectra. Those points are fitted by a linear function shown with a red line which reveals a g-factor of 2.05 in Cu_5. The extrapolation of the resonance line (red line) to $H = 0$ shows no ZFS which implies no magnetic anisotropy.

10.3. Discussion

When a polycrystalline sample is grinned to very fine powder, the observed ESR spectrum can be a combination of all individual spectra for different orientations

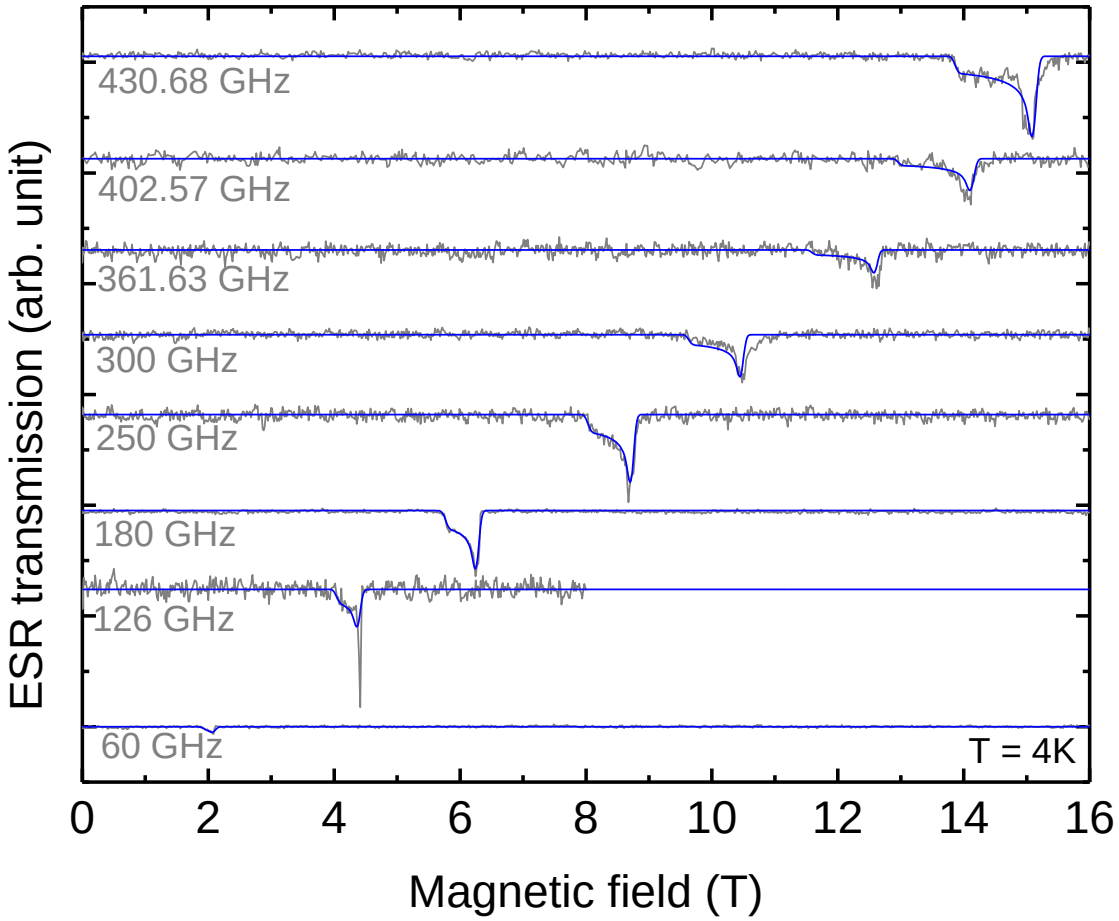

Figure 10.5: Frequency dependent ESR spectra (gray spectra) with simulation ESR spectra (blue lines) at $T = 4$ K.

[118]. Hence, an obtained ESR spectrum may broad, because it contains signals of all resonances corresponding to all possible orientations. These property reveals through various g-factors for the three directional components of the magnetic field. The resonance condition can be described as [119],

$$h\nu = g(\theta, \phi)\mu_B H = \mu_B H \sqrt{g_x^2\, sin^2\theta cos\phi^2 + g_y^2\, sin^2\theta sin^2\phi + g_z^2\, cos^2\theta}, \qquad (10.1)$$

were g_x, g_y and g_z are g-factors in the direction of the principal axes. θ is the polar angle and ϕ is the azimuthal angle. When a sample has an axial symmetry, there are two principal values: $g_{\|}$ and $g_{\perp}$. If the magnetic field is parallel

to the symmetry axis, there is a resonance which is related to $g_z = g_\parallel$. If the axis is perpendicular to the magnetic field, a resonance occurs, which is related to $g_x = g_y = g_\perp$. In the case of a rhombic symmetry, there are three possible orientations along all the principal axes, x, y, and z. ESR spectrum shows three different g-factors, g_x, g_y and g_z corresponding to the principal axes of a sample.

Each ESR spectrum shown in Fig. 10.3 is broad but there is a peak with a high intensity at higher magnetic fields. This represents a ESR powder spectrum. The g-factor is already known, but the g_x, g_y and g_z should be considered for analyzing the ESR spectra. In consideration of all directions of the sample, a simulation for a powder sample is performed. Fig. 10.4 and Fig. 10.5 show the simulation of the temperature dependence and of the frequency dependence, respectively. The simulation lines reproduce the experimental spectra well. Also, it reveals $g_x = 2.03 \pm 0.01$, $g_y = 2.04 \pm 0.01$ and $g_z = 2.23 \pm 0.01$ which indicate a g anisotropy.

10.4. Summary

The structure of $(HNEt_3)_2Cu(II)[12\text{-}MC_{Cu(II)N(Shi)}\text{-}4]$ contains of five Cu^{2+} ions. They are coupled antiferromagnetically and their saturation magnetization is $M_s \sim 1.1\mu_B$/f.u. [117]. The analysis of χT reveals a total spin $S = 1/2$ in the ground state [117].
Typical powder ESR spectra are obtained in both frequency dependence and temperature dependence data. When the temperature increases, the intensity of the ESR spectra decreases corresponding to the Boltzmann effect. The linear fit of the frequency dependent spectra reveals a g-factor of 2.05. Also, this resonance line shows no ZFS, which implies an isotropic system. The powder simulation is performed for Cu_5, because the observed ESR spectra contain all orientations of g-factors in the powder. This simulation shows a g-anisotropy comprising of $g_x = 2.03 \pm 0.01$, $g_y = 2.04 \pm 0.01$ and $g_z = 2.23 \pm 0.01$.

Part V.
Summary and Outlook

In this work, correlated electron systems and metal-organic spin systems have been investigated by using ESR. The main experimental technique applied is HF-ESR performed in the frequency range of 30 - 600 GHz and in magnetic fields up to 15 T. In addition, X-band ESR applying a resonator was applied, and static magnetic properties were determined up to 7 T by means of SQUID magnetometer.

The first studied materials are the honeycomb-lattice spin systems $Na_3Ni_2SbO_6$ and $Li_3Ni_2SbO_6$. Firstly, $Na_3Ni_2SbO_6$ shows the long range antiferromagnetic order below $T_N = 17$ K. Accordingly, the ESR data shows antiferromagnetic resonance (AFMR) at low temperature. Analysis of the ESR spectra by using the mean-field theory reveals an AFMR gap of 12.8 T ($\sim$ 358 GHz) and g-factors of 2.18 and 2.05 for the parallel and perpendicular modes, respectively. The temperature dependent ESR spectra indicate a rapid shift of the linewidth around T_N due to the development of internal fields. The simulation of AFMR mode yield the anisotropy field of 2.55 T and the exchange field of 32 T.

$Li_3Ni_2SbO_6$ has a similar structure a $Na_3Ni_2SbO_6$ except that Li^+ is substituted for Na^+. AFM order evolves at $T_N = 15$ K. In this case, the orthorhombic antiferromagnetic resonance is observed which exhibits two anisotropy fields. An analysis of the ESR data reveals an AFMR gap of 7 T and g-factors of 2.1 and 2.06 for the easy axis mode and the second easy axis mode. Also, it reveals the exchange constant λ, anisotropy constants K_1, and K_2 are 16.7 mole T^2/J, 2.6 and 1.5 J/mole, respectively. The temperature dependent ESR spectra show a change of linewidth around T_N due to internal antiferromagnetic fields.

The last frustrated transition metal oxide under study is the kagomé lattice $Ca_{10}Cr_7O_{28}$ which is constituted by the distorted bilayer of kagomé lattice. The g-factors along the c-axis are 2.01 at 4 K and 2.03 at 200 K, respectively. For the b-axis it shows the g-factors of 1.94 at 4 K and 1.93 at 30 K, respectively. The HF-ESR data shows no ZFS and the anisotropy of g-factors depending on crystallographic axes. The temperature dependence of X-band ESR data reveals that the linewidth decreases by decreasing temperature.

To investigate the influence of an attached gold atom on the magnetic proper-

ties of a Ni_2-complex, $[Ni_2L(dppba)]ClO_4$ ($2ClO_4$) and $[Ni_2L(dppba)AuPh]$ BPh_4 ($4BPh_4$) are studied. The gold atom is attached to the phosphorus atom of the head part of the latter one. For $2ClO_4$, the magnetization and susceptibility measurements yield a ferromagnetic coupling of - 23 K between the Ni^{2+} ions and a total spin $S = 2$. The same measurements on $4BPh_4$ reveal a similar ferromagnetic coupling of - 26 K and a total spin $S = 2$. ESR data on both samples shows similar magnetic anisotropies and the same g-factor. $2ClO_4$ and $4BPh_4$ have a negative uniaxial anisotropy of - 0.63 K (= -13.3 GHz) and - 0.56 K (= -11.6 GHz), respectively. This demonstrates a bistable magnetic ground state. Therefore, a gold atom does not give a significant change to the magnetic properties of the Ni_2 complex.

The second material is $[Ni(III)Ni(II)(L^{DA})](BPh_4)_2$ which contains mixed valence Ni^{2+} and Ni^{3+} ions. The magnetization measurements show a ferromagnetic coupling of - 48.5 K between the Ni ions and a total spin $S = 3/2$ which is a summation of $S = 1$ for Ni^{2+} and $S = 1/2$ for Ni^{3+}. Hence, in this case, Ni^{3+} ($3d^7$) is in the low spin state. The ESR data reveal a magnetic anisotropy of -24.5 GHz and a g-factor of 2.15 which corresponds to the total spin $S = 3/2$ in the ground state of the molecule. However, the analysis of the susceptibility and the simulation of the ESR spectrum show an impurity contribution of 25.9 % from a spin system with $S = 1$.

The third material is $[Gd(III)_2L(OAc)_4]PF_6$. The coupling between two Gd^{3+} is 0.19 K which is a small value compared to the magnetic field of 0.24 T $\cong$ 0.33 K (with $g = 2.0$) by the dipolar interaction. Even though the orbital angular moment of the Gd^{3+} ion can be negligible, the ESR data shows a ZFS of 5.9 GHz. This ZFS can be originated from the dipolar interaction. The calculation of the magnetic anisotropy induced by the dipolar interaction results the parameters, $\xi = 30°$, $\eta = 0°$ and $g = 2.01$. The angles of ξ and η means that $\vec{r}$, which mean the direction vector for two Gd^{3+} ions, is tilted around 30° from the z-axis.

The last material studied in this work is $(HNEt_3)_2Cu(II)[12\text{-}MC_{Cu(II)N(Shi)}\text{-}4]$ (Cu_5). Five Cu^{2+} ions are located on a common plane and are coupled antiferromagnetically. The ESR measurements on Cu_5 show typical powder spectra, no ZFS and a g-factor of 2.05. A powder simulation of Cu_5 reveals a g-anisotropy of $g_x = 2.03 \pm 0.01$, $g_y = 2.04 \pm 0.01$ and $g_z = 2.23 \pm 0.01$.

In summary, the results show how HF-ESR can contribute valuable information on, e.g., magnetic anisotropy, spin order and spin dynamics.

Bibliography

[1] D.C. Mattis, The theory of Magnetism I. *Springer Series in Solid-State Sciences* 1981.

[2] B. D. Cullity, C. D. Graham, Introduction to Magnetic Materials. *Wiley* 2009.

[3] W. Wernsdorfer, Molecular nanomagnets: towards molecular spintronics. *Int. J. Nanotechnology* **7**, 497, 2010.

[4] L. Thomas, F. Lionti, R. Ballou, D. Gatteschi, R. Sessoli, and B. Barbara, Macroscopic Quantum Tunnelling of Magnetization in a Single Crystal of Nanomagnets. *Nature (London)* **383**, 145-147, 1996.

[5] M.-H. Julien, Z. H. Jang, A. Lascialfari, F. Borsa, M. Horvatic, A. Caneschi, D. Gatteschi, Proton NMR for Measuring Quantum Level Crossing in the Magnetic Molecular Ring Fe_{10}. *Phys. Rev. Lett.* **83**, 227, 1999.

[6] C. Benelli, D. Gatteschi, Introduction to Molecular Magnetism: From Transition Metals to Lanthanides. *Wiley-VCH* 2015.

[7] G. Rogez, B. Donnio, E. Terazzi, J. Gallani, J. Kappler, J. Bucher, and M. Drillon, The Quest for Nanoscale Magnets: The example of [Mn12] Single Molecule Magnets. *Adv. Mater.* **21**, 4323, 2009.

[8] J. Tejada, E. M. Chudnovsky, E. del Barco, J. M. Hernandez, T. P. Spiller, Magnetic qubits as hardware for quantum computers. *Nanotechnology* **12**, 181-186, 2001.

[9] T. Neuberger, B. Schoöpf, H. Hofmann, M. Hofmann, B. von Rechenberg, Superparamagnetic nanoparticles for biomedical applications: Possibilities and limitations of a new drug delivery system. *Journal of Mag. and mag. materials* **293**, 483-496, 2005.

[10] M. Evangelisti, O. Roubeau, E. Palacios, A. Camn, T. N. Hooper, E. K. Brechin, J. J. Alonso, Cryogenic Magnetocaloric Effect in a Ferromagnetic Molecular Dimer. *Angew. Chem. Int. Ed.* **50**, 6606-6609, 2011.

[11] D. Gatteschi, R. Sessoli, Quantum tunneling of magnetizatino and related phenomena in molecular materials. *Angew. Chem. Int. Ed.* **42**, 268-297, 2003.

[12] S. Blundell, Magnetism in Condensed Matter. *Oxford University Press* 2001.

[13] L. Balents, Spin liquids in frustrated magnets. *Nature*, **464**, 199-208, 2010.

[14] Y. Tokura, Correlated-Electron Physics in Transition-Metal Oxides. *Amerian Institute of Physics, Physics today*, 50-55, 2003.

[15] G. R. Eaton, S. S. Eaton, K. M. Salikhov, Foundations of Modern EPR. *World Scientific* 1998.

[16] A. Lund, M. Shiotani, S. Shimada, Principles and Applications of ESR Spectroscopy. *Springer Netherlands* 2011.

[17] J. A. Weil, J. R. Bolton, Electron Paramagnetic Resonance: Elementary theory and practical applications. *John Wiley and Sons* 2007.

[18] C. Kittel, Introduction to Solid State Physics. *John Wiley and Sons, Inc* 2005.

[19] A. Abragam and B. Bleaney, Electron Paramagnetic Resonance of Transition Ions. *Oxford University Press, London* 1970.

[20] C. P. Poole, Jr., Electron Spin Resonance: A Comprehensive Treatise on Experimental Techniques. *Dover Publications, Inc., 2nd edition* 1996.

[21] G. T. Rado, H. Suhl Magntetism I. *Academic press* 1963.

[22] P. W. Anderson, P. R. Weiss, Exchange narrowing in paramagnetic resonance. *Reviews of morden physics* **25**, 1, 1953.

[23] R. M. White, Quantum Theory of Magnetism: Magnetic Properties of Materials. *Springer* 2007.

[24] A. M. Portis, Electronic Structure of F Centers: Saturation of the Electron Spin Resonance. *Phys. rev.* **91**, 1071-1078, 1953.

[25] L. H. Thomas, Motion of the spinning electron. *Nature* **117**, 514, 1926.

[26] H. N. Russell, F. A. Saunders, New Regularities in the Spectra of the Alkaline Earths. *Astrophysical Journal* **61**, 38-69, 1925.

[27] R. G. Burns, Mineralogical appplications of crystal field theory. *Cambridge University Press* 1993.

[28] A. S. Chakravarty, S. Basu, Effects of lower-symmetric crystal fields in the intermediate-coupling scheme for the transition-metal complexes. *Phys. Rev. B* **28**, 6861-6867, 1983.

[29] R. L. Liboff, Introductory Quantum Mechanics. *Addison-Wesley Publishing Company, 2nd edition* 1992.

[30] C. P. Slichter, Principles of Magnetic Resonance. *Springer-Verlag Berlin Heidelberg GmbH* 1978.

[31] O. Kahn, Molecular Magnetism. *Wiley-VCH* 1993.

[32] B. Barbara, Tunnelling and Coherence of Mesoscopic Spins. *Physik Journal* **7**, 81-85, 2008.

[33] H. Nojiri, H. Ohta, N. Miura, M. Motokawa, Study of spin-Peierls $CuGeO_3$ by high-field ESR. *Physica B* **246**, 16, 1998.

[34] S. Foner, High-field antiferromagnetic resonance in Cr_2O_3. *Phys. Rev.* **130**, 183, 1963.

[35] V. N. Glazkov, A. I. Smirnov, A. Revcolevschi, G. Dhalenne, Magnetic resonance study of the spin-reorientation transition in the quasi-one-dimensional antiferromagnet $BaCu_2Si_2O_7$. *Phys. Rev. B* **72**, 104401, 2005.

[36] L. Holmes, M. Eibschutz, and H.J. Guggenheim, Spin-flop transition in $BaMnF_4$. *Solid State Communications* **7**, 973-976, 1969.

[37] C. Kittel, Theory of Antiferromagnetic Resonance. *Phys. Rev.* **82**, 565, 1951.

[38] F. Keffer, Anisotropy in the Antiferromagnetic MnF_2. *Phys. Rev.* **87**, 608, 1952.

[39] Fred M. Johnson, Arthur H. Nethercot Jr., Antiferromagnetic resonance in MnF_2. *Phys. Rev.* **114**, 705, 1959.

[40] A. M. Portis, D. Teaney, Microwave faraday rotation in antiferromagnetic MnF_2. *Phys. Rev.* **116**, 838, 1959.

[41] M. Yehia, E. Vavilova, A. Möller, T. Taetz, U. Löw, R. Klingeler, V.Kataev, B. Büchner, Finite size effects and magnetic order in the spin 1/2 honeycomb lattice compound $InCu_{2/3}V_{1/3}O_3$. *Phys.Rev.B* **81**, 2010.

[42] F. Keffer, C. Kittel, Theory of antiferomagnetic resonance. *Phys. Rev.* **2**, 329-337, 1952.

[43] http://ewww.mpi muelheim.mpg.de/bac/logins/bill/julX en.php

[44] R. P. Feynman, Forces in Molecules. *Phys. rev.* **56**, 340-343, 1939.

[45] S. Stoll and A. Schweiger, EasySpin, a comprehensive software package for spectral simulation and analysis in EPR. *J. Magn. Reson.* **178(1)**, 42-55, 2006.

[46] G. Fusco, A. Tagliaferro, W.I. Milne, J. Robertson, Paramagnetic centres in tetrahedral amorphous carbon. *Diamond and Related Materials* **6**, 783-786, 1997.

[47] M. Bersohn, J. C. Baird, An introduction to electron paramagnetic resonance. *W. A. Benjamin, INC. New York* 1966.

[48] C. Dahl, P. Goy, and J. P. Kotthaus, Millimeter and Submillimeter Wave Spectroscopy of Solids, edited by G. Grüner. *Springer-Verlag, Berlin, Heidelberg, Topics in Applied Physics* **74**, 1998.

[49] Yun-Shik Lee, Principles of Terahertz Science and Technology. *Springer* 2009.

[50] C. Golze, Tunable High-Field / High-Frequency ESR and High-Field Magnetization on Single-Molecule Clusters. *PhD thesis* Technischen Universität Dresden, 2007.

[51] A. W. Scott, Understanding microwaves. *John Wiley and Sons Inc.* 1993.

[52] D. J. Griffiths, Introduction to electrodynamics. *PRENTICE HALL, Englewood Cliffs, New Jersey* 1989.

[53] J.D. Jackson, Classical Electrodynamics. *John Wiley and Sons Inc., New York* 1998.

[54] F. A. Benson, T. M. Benson, Fields, Waves and Transmission Lines. *Springer science and business media* 1991.

[55] H. T. Diep, Frustrated Spin Systems. *World Scientific* 2004.

[56] G. H. Wannier, Antiferromagnetism. The Triangular Ising Net. *Phys.Rev.B* **79**, 357, 1950.

[57] J. Villain, Spin glass with non-random interactions. *J. Phys. C: Solid State Phys.* **10**, 1717, 1977.

[58] G. Toulouse, Spin glass with non-random interactions. *Commun. Phys.* **2**, 115, 1977.

[59] P. H. Y. Li, R. F. Bishop, C. E. Campbell, A frustrated spin-1 J_1-J_2 Heisenberg antiferromagnet: An anisotropic planar pyrochlore model. *J. Phys.: Conf. Ser.* **529**, 012008, 2014.

[60] M. Kotobuki, Y. Suzuki, H. Munakata, K. Kanamuraa, Y. Sato, K. Yamamoto, T. Yoshida, Compatibility of $LiCoO_2$ and $LiMn_2O_4$ cathode materials for $Li_{0.55}La_{0.35}TiO_3$ electrolyte to fabricate all-solid-state lithium battery. *Journal of power sources* **195**, 5784-5788, 2010.

[61] Jeffrey Ma, Shou-Hang Bo, Lijun Wu, Yimei Zhu, Clare P. Greyac, Peter G. Khalifah, Ordered and disordered polymorphs of $Na(Ni_{2/3}Sb_{1/3})O_2$: honeycomb-ordered cathodes for Na-ion batteries. *Chemistry of Materials* , , 2015.

[62] J.B. Fouet, P. Sindzingre, C. Lhuillier, An investigation of the quantum J_1-J_2-J_3 model on the honeycomb lattice. *Eur. Phys. J. B* **20**, 241 - 254, 2001.

[63] Yoko Miura, Riu Hirai, Toshiaki Fujita, Yoshiaki Kobayashi, Masatoshi Sato, Spin-gap behavior of distorted honeycomb lattice system $Na_3Cu_2SbO_6$. *Journal of Magnetism and Magnetic Materials* **310**, e389 - e391, 2007.

[64] J. M. S. Skakle, M. A. Castellanos R., S. Trujillo Tovar, A. R. West, Synthesis of $Li_3Cu_2SbO_6$, a New Partially Ordered Rock Salt Structure. *Journal of Solid State Chemistry* **131**, 115- 120, 1997.

[65] E.A. Zvereva, V.B. Nalbandyan, J.-Y. Lin, E.L. Vavilova, M.F.Iakovleva, M. Abdel-Hafiez, A.V. Silhanek, H-L. Feng, K. Yamaura, A. Stroppa, S. Picozzi, H. O. Jeschke, R. Valenti, and A.N. Vasiliev, Magnetic phase diagram of monoclinic honeycomb lattice antimonates $A_3Ni_2SbO_6$ (A=Li, Na) (In preparation).

[66] H. O. Jeschke and R. Valenti, Electronic structure of $Na_3Ni_2SbO_6$ and $Li_3Ni_2SbO_6$. (In preparation).

[67] M. Achiki, K. Yosida, Antiferromagnetism of Zn-Ferrite. *Progress of Theoretical Physics* **17**, 223, 1957.

[68] E. Chappel, M.D. Núñez-Regueiro, F. Dupont, G. Chouteau, C. Darie, A. Sulpice, Antiferromagnetic resonance and high magnetic field properties of $NaNiO_2$. *Eur. Phys. J. B* **17**, 609-614, 2000.

[69] Susumu Okubo, Hideo Wada, Hitoshi Ohta, Takahiro Tomita, Masashi Fujisawa, Takahiro Sakurai, Eiji Ohmichi, Hikomitsu Kikuchi, Anomalous Spin Dynamics Observed by High-Frequency ESR in $InCu_{2/3}V_{1/3}O_3$. *J.Phys.Soc.Jpn* **80**, 023705, 2011.

[70] E. P. Trounson, D.F. Bleil, R.K. Wangsness, L. R. Maxwell, Magnetic Resonance in Antiferromagnetic Materials near the Curie Temperature. *Phys. Rev.* **79**, 542, 1950.

[71] Masashi Hase, Masayuki Hagiwara, and Koichi Katsumata, Observation of an antiferromagnetic resonance in the spin-Peierls compound $CuGeO_3$ doped with Zn. *Phys. Rev. B* **54**, R3722, 1996.

[72] J. C. Burgiel, M. W. P. Strandberg, Antiferromagnetic resonance linewidth in MnF_2 near the transition temperature. *J. App. Phys.* **35**, 852, 1964.

[73] Hitesh J. Changlani, Andreas M. Läuchli, Trimerized ground state of the spin-1 Heisenberg antiferromagnet on the kagome lattice. *Phys. Rev. B* **91**, 100407(R), 2015.

[74] P. Nikolic, T. Senthil, Physics of low-energy singlet states of the Kagome lattice quantum Heisenberg antiferromagnet. *Phys. Rev. B* **68**, 214415, 2003.

[75] J. T. Chalker, P. C. W. Holdsworth, E. F. Shender, Hidden order in a frustrated system: Properties of the Heisenberg Kagome antiferromagnet. *Phys. Rev. Lett.* **68**, 855, 1992.

[76] Itiro Syôzi, Statistics of Kagome Lattice. *Progress of Theoretical Physics* **6**, 306, 1951.

[77] Matthew P. Shores, Emily A. Nytko, Bart M. Bartlett, and Daniel G. Nocera, A Structurally Perfect $S = 1/2$ Kagomé Antiferromagnet. *J. Am. Chem. Soc.* **127**, 13462-13463, 2005.

[78] J. L. Atwood, Kagomé lattice: A molecular toolkit for magnetism. *Nature Materials* **1**, 91-92, 2002.

[79] C. Balz, B. Lake, M. Reehuis, O. Prokhnenko, A.T.M.N. Islam, S. Toth, Y. Singh, Report on the diffraction study of a new Calcium Chromium Oxide $Ca_10(Cr^VO_4)_6(Cr^{VI}O_4)$ (In preparation).

[80] A. Chubukov, Order from disorder in a kagome antiferromagnet. *Phys. Rev. Lett.* **69**, 832, 1992.

[81] Wei-min Zhang, Hitoshi Ohta, Susumu Okubo, Masashi Fujisawa, Takahiro Sakurai, Yoshihiko Okamoto, Hiroyuki Yoshida, Zenji Hiroi, High-Field ESR Measurements of S=1/2 Kagome Lattice Antiferromagnet $BaCu_3V_2O_8(OH)_2$. *J. Phys. Soc. Jpn.* **79**, 023708, 2010.

[82] H. Ohta, W. Zhang, S. Okubo, M. Tomoo, M. Fujisawa, H. Yoshida, Y. Okamoto, Z. Hiroi, S=1/2 Kagome Lattice Antiferromagnet $Cu_3V_2O_7(OH)_2 \cdot 2H_2O$ Studied by High Field ESR. *J. Phys.: Conf. Ser.* **145**, 012010, 2009.

[83] M. Sumikawa, H. Ohta, M. Motokawa, H. Kikuchi, H. Nagasawa, EPR of the Kagome antiferromagnet $SrCr_8Ga_4O_{19}$. *Physica B* **201**, 123-126, 1994.

[84] S. Okubo, M. Tomoo, H. Ohta, and H. Kikuchi, High field ESR measurements of S=1/2 kagome Heisenberg antiferromagnet $ZnCu_3(OH)_6C_{l2}$. *J. Phys.: Conf. Ser.* **145**, 012011, 2009.

[85] G. Christou, D. Gatteschi, D. N. Hendrickson, R. Sessoli, Single-molecule magnets. *MRS Bulletin* **36**, 66-71, 2000.

[86] A. Caneschi, D. Gatteschi, N. Lalioti, C. Sangregorio, R. Sessoli, G. Venturi, A. Vindigni, A. Rettori, M. G. Pini, M. A. Novak, Cobalt(II)-nitronyl nitroxide chains as molecular magnetic nanowires. *Angew. Chem. Int. Ed.* **40**, 1760-1762, 2001.

[87] Y. D. Zhang, J. I. Budnick, W. A. Hines, C. L. Chien J. Q. Xiao, Effect of magnetic field on the superparamagnetic relaxation in granular Co-Ag samples. *Apple. Phys. Lett.* **72**, 2053-2055, 1998.

[88] D. Gatteschi, R. Sessolia, A. Cornia, Single-molecule magnets based on iron(III) oxo clusters. *Chem. Commun.* **9**, 725-732, 2000.

[89] K. M. Mertesa, Y. Suzukia, M. P. Sarachika, Y. Myasoedovb, H. Shtrikmanb, E. Zeldovb, E. M. Rumbergerc, D. N. Hendricksonc, G. Christoud, Mn_12-acetate: a prototypical single molecule magnet. *Solid state communication* **127**, 131-139, 2002.

[90] J. J. Henderson, C. Koo, P. L. Feng, E. del Barco, S. Hill, I. S. Tupitsyn, P. C. E. Stamp, D. N. Hendrickson, Manifestation of Spin Selection Rules on the Quantum Tunneling of Magnetization in a Single-Molecule Magnet. *Phys. Rev. Lett.* **103**, 017202, 2009.

[91] D. Gatteschi, R. Sessoli, J. Villain, Molecular nanomagnets. *Oxford university press* 2006.

[92] G. Aromi, S. M. J. Aubin, M. A. Bolcar, G. Christou, H. J. Eppley, K. Forlting, D. N. Hendrickson, J. C. Huffman, R. C. Squire, H. L. Tsai, S.

Wang, M. W. Wemple, Manganese carboxylate clusters: from structural aesthetics to single- molecule magnets. *Polyhedron* **17**, 3005, 1998.

[93] T. Lis, Preparation, structure and magnetic properteis of a dodecanuclear mixed valence manganese carboxylate. *Acta Cryst.* **B36**, 2042-2046, 1980.

[94] R. Sessoli, D. Gatteschi, A. Caneschi, M. A. Novak, Magnetic bistability in a metal-ion cluster. *Nature* **365**, 141, 1993.

[95] K.M. Mertesa, Y. Suzukia, M.P. Sarachika, Y. Myasoedovb, H. Shtrikmanb, E. Zeldovb, E.M. Rumbergerc, D.N. Hendricksonc, G. Christoud, Mn_{12}-acetate: a prototypical single molecule magnet. *Solid State Communications* **127**, 131-139, 2003.

[96] E. del Barco, A. D. Kent, S. Hill, J. M. North, N. S. Dalal, E. M. Rumberger, D. N. Hendrickson, N. Chakov, and G. Christou, Magnetic Quantum Tunneling in the Single-Molecule Magnet Mn_{12}-Acetate. *Journal of Low Temperature Physics* **140**, 119, 2005.

[97] J. R. Friedman, M. P. Sarachik, J. Tejada, , and R. Ziolo, Macroscopic Measurement of Resonant Magnetization Tunneling in High-Spin Molecules. *Phys. Rev. Lett.* **76**, 3830-3833, 1996.

[98] B. Bogani, W. Wernsdorfer, Molecular spintronics using single-molecule magnets. *Nat. Mat.* **7**, 179, 2008.

[99] C. J. Milios, S. Piligkos, E. K. Brechin, Ground state spin-switching via targeted structural distortion: twisted single-molecule magnets from derivatised salicylaldoximes. *Solid State Communications* **14**, 1809-1817, 2008.

[100] M. N. Leuenberger, D. Loss, Quantum computing in molecular magnets. *Nature* **410**, 789-793, 2001.

[101] A. Cornia, M. Mannini, P. Sainctavitc, R. Sessoli, Chemical strategies and characterization tools for the organization of single molecule magnets on surfaces. *Chem. Soc. Rev.* **40**, 3076-3091, 2011.

[102] F. Troiania, M. Affronte, Molecular spins for quantum information technologies. *Chem. Soc. Rev.* **40**, 3119-3129, 2011.

[103] M. Mannini, F. Pineider, P. Sainctavit, C. Danieli, E.Otero, C. Sciancalepore, A. M. Talarico, M. Arrio, A. Cornia, D. Gatteschi, R. Sessoli, Magnetic memory of a single-molecule quantum magnet wired to a gold surface. *Nat. Mater.* **8**, 194-197, 2009.

[104] M. Golecki, J. Lach, A. Jeremies, F. Lungwitz, M. Fronk, G. Salvan, D. R. T. Zahn, J. Park, Y. Krupskaya, V. Kataev, R. Klingerler, B. Büchner, B. Mahns, M. Knupfer, P. F. Siles, D. Grimm, O. G. Schmidt, A. Reis, W. R. Thiel, D. Breite, B. Abel, B. Kersting, Chemisorption of

Exchange-Coupled $[Ni_2L(dppba)]^+$ Complexes on Gold by Using Ambidentate 4-(Diphenylphosphino)benzoate Co-Ligands. *Chem. Eur. J.* **19**, 7787-7801, 2013.

[105] B. M. Trost, M. R. Machacek, A. Aponick, Predicting the Stereochemistry of Diphenylphosphino Benzoic Acid (DPPBA)-Based Palladium-Catalyzed Asymmetric Allylic Alkylation Reactions: A Working Model. *Acc. Chem. Res.* **39**, 747-760, 2006.

[106] C. K. Jorgensen, Oxidation numbers and oxidation states. *Berlin, Germany: Springer* 1969.

[107] P. Day, N. S. Hush, R. J. H. Clark, Mixed valence: origins and developments. *Phil. Trans. R. Soc. A* **366**, 5, 2008.

[108] D. R. Gamelin, E. L. Bominaar, M. L. Kirk, K. Wieghardt, E. I. Solomon, Excited-state contributions to ground-state properties of mixed-valence dimers: spectral and electronic-structural studies of $[Fe_2(OH)_3(tmtacn)_2]^{2+}$ related to the $[Fe_2S_2]^+$ active sites of plant-type ferredoxins. *J. Am. Chem. Soc.* **118**, 8085, 1996.

[109] B. Kersting, M. J. Kolm, C. Janiak, Thiolate-Bridged Diiron(III) Complex with Spin-Crossover Behaviour. *Z. anorg. allg. Chem.* **627**, 775-780, 1998.

[110] B. Kersting, D. Siebert, First Examples of Dinickel Complexes Containing the $N_3Ni(\mu_2\text{-}SR)_3NiN_3$ Core. Synthesis and Crystal Structures of $[L_2Ni_2][BPh_4]_2$ and $[L_3Ni_2][BPh_4]_2$ (L = 2,6-Di(aminomethyl)-4-*tert*-butylthiophenolate). *Inorg. Chem.* **37**, 3820-3828, 1998.

[111] B. C. Cavenett, The allowed and forbidden transitions in the paramagnetic resonance of the manganese ion in cubic zinc selenide. *Proc. Phys. Soc* **84**, 1-9, 1964.

[112] Peter Comba, Michael Grosshauser, Dennis Müller, Rüdiger Klingeler, Mark Riley, and Hubert Wadepohl, Magnetic properties of and Interactions within a series of homodinuclear Lanthanide complexes (Unpublished).

[113] A. Ozarowski, The Zero-Field-Splitting Parameter D in Binuclear Copper(II) Carboxylates Is Negative. *Inorgain Chemistry* **47**, 21, 2008.

[114] A. Ozarowski, D. Reinen, Anisotropic Exchange Interactions in the Copper(II) and Vanadium(IV) Dimers $[(L')Cu(\mu\text{-}OH)_2Cu(L')](ClO_4)_2$ and $[(L)VO(\mu\text{-}OH)_2VO(\ L)]Br_2$ with 1,4,7-Triazacyclononane(L) and Its N,N',N"-Trimethyl Derivative (L'): A Single-Crystal EPR Study. *Inorgain Chemistry* **25**, 1704, 1986.

[115] A. Benchini, D. Gatteschi, EPR of exchange coupled systems. *Dover* 2012.

[116] T.D.Smith, The determination of structural properties of dimeric transition

metal ion complexes from EPR spectra. *Coordination Chemistry Reviews* **13**, 173, 1974.

[117] P. Happa, E. Rentschler, Enforcement of a high-spin ground state for the first 3*d* heterometallic 12-metallacrown-4 complex. *Dalton Trans.* **43**, 15308, 2014.

[118] M. A. Hemminga, L. J. Beliner, ESR Spectroscopy in Membrane Biophysics. *Springer* 2007.

[119] D. M. Murphy, S. David Jackson, J. S. J. Hargreaves, EPR (Electron Paramagnetic Resonance) Spectroscopy of Polycrystalline Oxide Systems. *WILEY-VCH* 2009.

Publication List

1. Chemisorption of Exchange-Coupled $[Ni_2L(dppba)]^+$ Complexes on Gold by Using Ambidentate 4-(Diphenylphosphino)benzoate Co-Ligands,
   M. Golecki, J. Lach, A. Jeremies, F. Lungwitz, M. Fronk, G. Salvan, D. R. T. Zahn, **J. Park**, Y. Krupskaya, V. Kataev, R. Klingerler, B. Büchner, B. Mahns, M. Knupfer, P. F. Siles, D. Grimm, O. G. Schmidt, A. Reis, W. R. Thiel, D. Breite, B. Abel, and B. Kersting,
   Chem. Eur. J. **19**, 7787-7801, 2013.

2. Magnetic interactions in a series of homodinuclear lanthanide complexes,
   Peter Comba, Michael Großerhauser, Rüdiger Klingeler, Changhyun Koo, Yanhua Lan, Dennis Müller, **Jaena Park**, Annie Powell, Mark J. Riley, and Hubert Wadepohl,
   Inorganic Chemistry, (submitted).

Acknowledgment

First of all, I would like to thank Prof. Rüdiger Klingeler to give me the wonderful chance to study at University Heidelberg. I have learned how to think and approach to Physics from his performance. He has always provided opportunities to visit him anytime for discussions and has given clear and lucid explanations. Also, I appreciate for his great effort to teach me in the physics field. Besides, I am thankful for his kind and friendly behavior.

I would like to thank my committee members, Prof. Bernd Pilawa, Prof. Ulrich Schwarz, and Prof. Norbert Frank, for overseeing my dessertation.

Also, I would like to thank Dr. Changhyun Koo for his great support. He is always available for helpful suggestions and discussions about experiments and all matters for work.

I want to thank Dr. Vladislav Kataev for giving me the chance to start my first research at the IFW. All the time it was very helpful to discuss with him whenever there was any questions.

I also want to acknowledge Dr. Yulia Krupskaya for her support and valuable comments in the laboratory and the office.

I thank the Sci-Ed it Publications to correction of syntax and grammar of the page from 3 to 29.

I would like to express my gratitude to Alexander Ottmann, Christoph Neef, Ahmad Omar, Ashwin Mohan, and Steven Rodan who are my colleagues as well as my friends. Thanks to you, I felt here as my hometown. I have a full of grateful memories with you.

Further, I am thankful to the whole group, Dr. Kunpen Wang, Dr. Jianxiu Zhang, Msia Tavhelidse, Johannes Werner, Cebrail Pür, Elisa Thauer, and other Master/Bachelor students for happy work atmosphere, for the interesting discussions during our cake and coffee time. Thank you very much for the last years in Heidelberg.

Finally, I would like to thank to my family and my friends for their support and encouragement. Especially, I give a big thanks and love to our mom.

Erklärungen gemäß § 8 (3) b) der Promotionsordnung

Ich erkläre hiermit, dass ich die vorgelegte Dissertation selbst verfasst und mich dabei keiner anderen als der von mir ausdrücklich bezeichneten Quellen und Hilfen bedient habe.

Heidelberg, 01. 09. 2015

Jaena Park